

PRESENT STATUS OF THE R&D ON MCFC IN CRIEPI/JAPAN

*Yoshiyuki Izaki, Yoshihiro Mugikura, Eiichi Koda
Takao Watanabe, Toshio Abe
Central Research Institute of Electric Power Industry
(CRIEPI)
2-6-1 Nagasaka, Yokosuka-shi, Kanagawa-ken,
240-01 Japan

* : presently at Illinois Institute of Technology
under collaboration research agreement with IIT, Chicago

Keywords: MCFC, CRIEPI, Japan

Introduction

Molten Carbonate Fuel Cells (MCFC) power plants are expected to have high generation efficiency and to be favorable for environmental protection. In Japan, recently, many electric utilities are interested in this technology.

R&D on MCFC technology in Japan has been started under the Moonlight Project of the Agency of Industrial Science and Technology, Ministry of International Trade and Industry. Currently, the R&D is concerned not only with MCFC stack technology but also with balance of plant (BOP) technology for a 1MW pilot plant. Moreover, other national or private research programs concerned with the MCFC are in progress.

CRIEPI has participated in the Moonlight Project as a representative of all Japanese electric utilities, and has been in charge of the total system study and stack operating study from the beginning. In addition, CRIEPI has been conducting collaborative projects with several companies, to support the Moonlight Project and to accelerate the introduction of MCFC technology into Japanese electric utilities. In these projects, a number of cells and stacks have been constructed and operated, and their performance has been constantly improved. Some issues remain to be solved, especially, life and energy density improvement to reduce cost. It is necessary to accumulate basic operational data systematically and to understand long-term performance. Recently, research has focused on these data.

In this paper, the status of R&D on MCFC in Japan is introduced, and selected results achieved in CRIEPI projects are described. Moreover, CRIEPI's future plans for R&D are also introduced.

Status of R&D on MCFC technology in Japan

Moonlight project⁽¹⁾

R&D in Japan is mainly conducted under the Moonlight project. The target of this project is the development of a 1MW external reforming MCFC pilot plant. Fig.1 and Fig.2 show the organization for MCFC development under the Moonlight Project and the

R&D schedule, respectively. As for the fuel cell stacking technology, two types of 100kW external reforming stacks and a 30 kW direct internal reforming stack are being developed. All of stacks are to be operated by September 1993 for intermediate evaluation.

Furthermore, as for BOP technology, two types of fuel reformers, a high temperature gas recycle blower, a turbine compressor, a heat recovery steam generator and total plant control methods are being developed by the MCFC Research Association. All of their equipment is to be demonstrated by September 1993, as are the MCFC stacks.⁽²⁾

Moreover, stack operation technology to optimize its operation conditions is being developed and a total system study to clarify the image of future MCFC power plants and support technology, i.e. material development, gas clean-up technology for coal gasified gas and so on, are being undertaken with a view of the future.

Joint research program of Kansai Electric Power Company and Mitsubishi Electric Co.

Kansai Electric Power Company is the second-largest electric power company in Japan. It has been conducting development on Indirect Internal Reforming (IIR) MCFC stacks under a joint research project with Mitsubishi Electric Company since 1988. In this project a 100kW stack has been operated for 2,308 hours during 1992.⁽³⁾ Recently, the next phase in this joint research program has been addressed. This concerns the development of modified IIR stacks technology and the simple system technology.

Review of the R&D in CRIEPI

CRIEPI has been conducting R&D on MCFC technology since 1980 as one of the future key technologies for electric power utilities and has also been participating in the Moonlight Project since 1981.⁽⁴⁾ Thus far, a number of cells and stacks have been operated under a collaborative research agreement with various Japanese developers such as Hitachi, Ltd., Ishikawajima-Harima Heavy Industries Co., Ltd. (IHI), Mitsubishi Electric Corp., Fuji Electric Co., Ltd. and Toshiba Corp., to support the Moonlight project and to accelerate the introduction into Japanese electric utilities. Table 1 shows the history of the R&D objectives in CRIEPI.

Stack operation technology

It is necessary to realize high performance and reliability of the stack itself in actual operation. To obtain high performance, pressurized operation and high utilization are desirable. To ensure high reliability in large-scale stack operation, uniform gas flow and uniform temperature distribution are required. Therefore, it is important to develop the operation technology as well as the stack design technology.

CRIEPI has installed a 10kW class test facility with several gas recycling loops in 1988, to test the operation technology of large-scale stacks.⁽⁵⁾ Using the facility, a 6kW and a 10kW class stacks have already been operated under collaborative research agreements with IHI. In the operation of the 6kW class stack, it was confirmed that their gas recycling techniques are suitable for MCFC stack operation.⁽⁶⁾ The 10kW class stack has been operated for about 4000 hours under pressurized and high fuel utilization conditions in 1991, by means of anode and cathode gas recycling techniques.⁽⁷⁾ (Fig.3)

CRIEPI is also in charge of the stack operation study in the Moonlight project. Based on the above operation results, a 100kW test facility was designed and constructed in 1993, and one of the two 100kW stacks developed in the project is now being operated in this facility.

Cell and stack evaluation technology

To evaluate and improve the MCFC technology, it is important to accumulate and evaluate operation data under conditions close to actual use. CRIEPI has conducted several operation tests with bench-scale cells and stacks, and a large number of data have been accumulated and analyzed. From these data it was concluded that pressurized operation is suitable to achieve higher performance, because it reduces cathode reaction resistance.^(8,9) (Fig. 4)

Pressurized operation, however, accelerates nickel cathode dissolution into the electrolyte matrix. Deposition of the dissolved nickel in the matrix may lead to failure of the cell, caused by internal short circuit. To understand this phenomenon, experiments on nickel dissolution under more severe conditions were carried out under a collaborative research agreement with Mitsubishi Electric Co.. The effects of the partial pressure of carbon dioxide in cathode gas and of the thickness of electrolyte tile on nickel dissolution and shorting have been clarified with bench-scale cells.⁽¹⁰⁾ (Fig. 5)

System analysis technology

It is necessary to clarify the MCFC plant image and its performance preliminary to introducing it into electric utilities. Several kinds of MCFC power plants, i.e. LNG fueled, coal-gas fueled and co-generation plants, have been designed conceptually thus far, under in-house research and as part of the Moonlight Project.⁽¹¹⁾

From these study it has been concluded that, in order to satisfy the requirements of electric power utilities, external reforming MCFC plants must be pressurized and the MCFC stacks must high energy density.

R&D Strategy of CRIEPI

From the results presented here, it is clearly important to improve the life time and energy density of MCFC stacks. To solve these issues, continued long-term and high energy density operation data will be accumulated systematically under collaborative research agreements with Hitachi, IHI and Mitsubishi Co., respectively. In addition, to obtain long-term performance experience, several experiments with bench-scale cells will be carried out by CRIEPI working with electric utilities.

To optimize cathode operation, which is a key to longer MCFC life and high energy density, more basic studies, clarifying the reaction mechanism under high pressure operation and studying the interfacial phenomena between electrode materials and electrolyte, are needed. Research on these topics has been started in collaboration with Tohoku University, Japan and Illinois Institute of Technology, Chicago, U.S., respectively.⁽¹²⁾

References

- (1) T. Kodama, Y. Miyazaki, A. Fukutome, K. Honjo, " Research and Development on Molten Carbonate Fuel Cell Power Generation Technology under the Moonlight Project," Proceeding Third International Symposium on Carbonate Fuel Cell Technology, PV 93-3, The Electrochemical Society, Inc., Pennington NJ, pp. 106-113 (1992).
- (2) T. Mori and N. Horiuchi, " Demonstration of MCFC Stacks and Plant System at Akagi Stack and System Square," Proceeding of the third international symposium on Carbonate Fuel Cell technology, Proceeding Third International Symposium on Carbonate Fuel Cell Technology, PV 93-3, The Electrochemical Society, Inc., Pennington NJ, pp. 11-24 (1992).
- (3) J. Ohtsuki, T. Seki, S. Takeuchi, A. Kusunoki, A. Sasaki, H. Urushibata, T. Murahashi, " Development of Indirect Internal Reforming Molten Carbonate Fuel Cell," Proceeding Third International Symposium on Carbonate Fuel Cell Technology, PV 93-3, The Electrochemical Society, Inc., Pennington NJ, pp. 48-62 (1992).
- (4) T. Abe, Y. Izaki, T. Watanabe, Y. Mugikura, K. Shimazu, " Trends and Prospects in the Development of Molten Carbonate Fuel Cell in Japan," Proceeding Second International Symposium on Carbonate Fuel Cell Technology, PV 90-16, The Electrochemical Society, Inc., Pennington NJ, pp. 16-34 (1990).
- (5) Y. Izaki, T. Watanabe, Y. Mugikura et al, " Experimental Results of a 10kW class Molten Carbonate Fuel Cell," Proceeding 24th. IECEC , pp. 1523-1528 (1989).
- (6) Y. Mugikura, T. Watanabe, Y. Izaki, T. Matsuyama, T. Shimizu, S. Sato et al, "6kW class MCFC with Gas Recycling," Abstracts 1990 Fuel Cell Seminar, pp. 103-106.
- (7) Y. Izaki, T. Watanabe, Y. Mugikura, T. Matsuyama, T. Shimizu, S. Sato et al, "Large Scale MCFC Performance and Operation Technology," Proceedings of the International Fuel Cell Conference, Makuhari, pp. 243-246 (1992).
- (8) Y. Izaki, Y. Mugikura, E. Koda, T. Matsuyama, T. Shimizu, S. Sato et al, " Proceeding Third International Symposium on Carbonate Fuel Cell Technology, PV 93-3, The Electrochemical Society, Inc., Pennington NJ, pp. 119-130 (1992).
- (9) Y. Mugikura, Y. Izaki, T. Watanabe, H. Urushibata, S. Yoshioka, H. Maeda et al, " Evaluation of MCFC Performance at Elevated Pressure," Proceedings of the International Fuel Cell Conference, Makuhari, pp. 215-218 (1992).
- (10) Y. Mugikura, Y. Izaki, T. Watanabe, E. Koda, H. Kinoshita, T. Abe, " Development Status of MCFC at CRIEPI," Abstracts 1992 Fuel Cell Seminar, pp. 109-112.
- (11) E. Koda, Y. Izaki, T. Abe, N. Nagasaki, T. Shimizu, " The Conceptual Design of MCFC Power Plants", Proceeding of the third international symposium on Carbonate Fuel Cell technology, pp. 75-88 (1992).
- (12) T. Watanabe and J. R. Selman, " Metal Wetting Behavior by Molten Carbonate," Abstracts 1990 Fuel Cell Seminar, pp. 559-562.

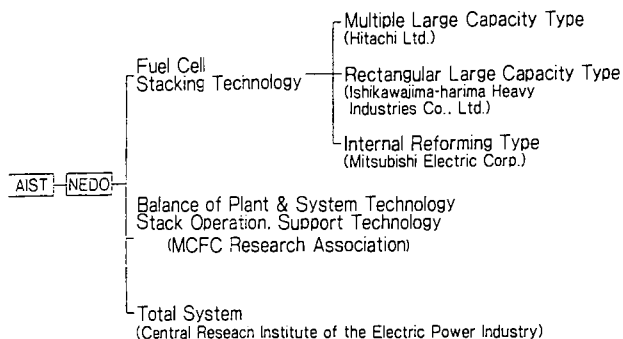


Fig. 1 Organization of MCFC Development in the Moonlight Project

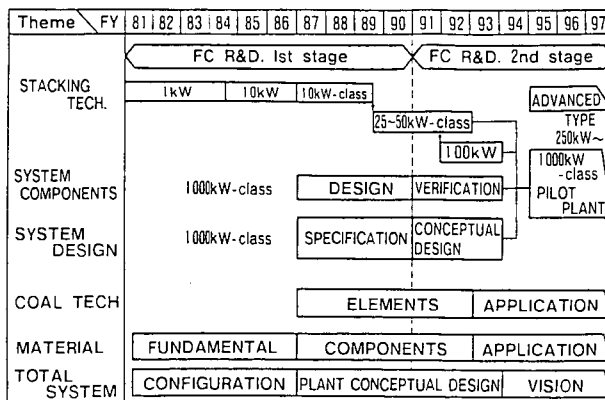


Fig. 2 R&D Program on MCFC Power Generation in the Moonlight Project

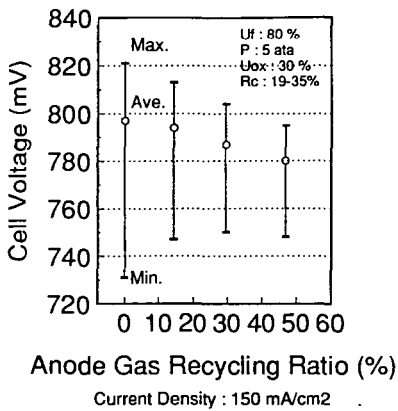


Fig. 3 Effect of anode gas recycling on a MCFC stack

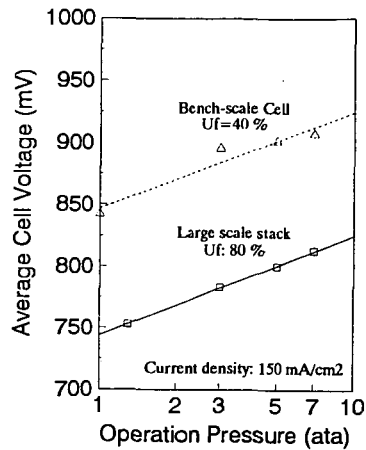


Fig. 4 Effect of operating pressure on cell performance

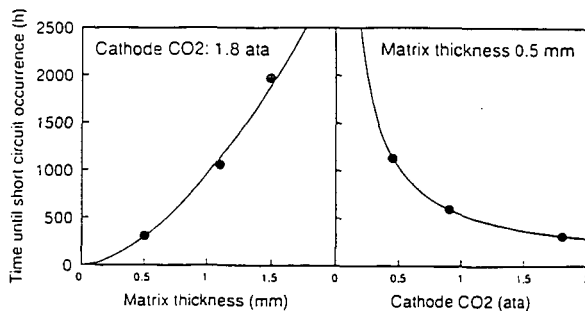


Fig. 5 Effects of matrix's thickness and CO₂ partial pressure on the start time of internal short

Table 1. Trend of R&D Items in CRIEPI

Year	R&D Items
1980 to 1984 :	Evaluation of single small cell performance
1984 to 1989 :	R&D on cell and stack evaluation technology <ul style="list-style-type: none"> •Evaluation of single cells and stacks up to 1kW class •Development of operation technology on large-scale stacks
1989 to 1992 :	R&D on cell and stack evaluation technology <ul style="list-style-type: none"> •Improvement of stack performance up to 10kW class •Evaluation on pressurized condition
	R&D on MCFC plant technology <ul style="list-style-type: none"> •Establishment of gas recycling technology •Conceptual design of MCFC power plant

Table 2. R&D Schedule of CRIEPI

<ul style="list-style-type: none"> •Development of higher energy density stacks Two 10kW class stacks will be operated by 1995 under higher current density (over 200mA/cm²). •Evaluation of the relationship between operation conditions and cell life. Several bench-scale cells will be evaluated by together with electric utilities. •Optimization of cathode electrode for higher energy density and long-life cells. Basic data for the optimization will be accumulated by together with Tohoku University and IIT.

PERFORMANCE ANALYSIS OF IMHEX FULL-AREA STACKS

W. C. Hu and G. L. Reznikov

M-C Power Corporation

8040 S. Madison Street, Burr Ridge, IL 60521-5808

Keywords: Performance, MCFC, Full-Area Stack

ABSTRACT

M-C Power Corporation is actively engaged in the commercialization of molten carbonate Fuel Cell Technology based on the IMHEX[®] stack configuration conceived by the Institute of Gas Technology (IGT). The active cell area has been successfully scaled up from 1 ft² of subscale stack to 1 m² of full-area commercial stack. Two 20 kW full-area stack tests have been completed. Both stacks operated successfully for about 2000 hours. Both stacks demonstrated the capability of producing maximum power exceeding the design capacity of 20 kW. Pressure drop characteristics were also within the range for designing larger commercial stacks. Both stacks demonstrated many of the operational modes expected for commercial applications. This paper presents the performance analysis of the data generated from these two full-area stack tests.

INTRODUCTION Since its inception in 1987, M-C Power has successfully demonstrated that the internally manifolded heat exchanger concept (IMHEX[®]) developed by IGT is a commercially viable molten carbonate fuel cell technology for power generation. In April-June of 1991, M-C Power successfully built and operated a 70-cell stack with active area of 1 ft² for 1580 hours of power generation. Since then, M-C Power has successfully built and operated two full-area-commercial-size fuel cell stacks with active area of 1 m². The first full-area stack with 19 cells was tested in April-July of 1992 for a duration of 2200 hours. The second full-area stack with 20 cells was tested in November 1992-January 1993 for a duration of 1900 hours. The following sections discuss the results obtained from these two full-area stack tests.

FIRST FULL-AREASTACK Two types of gases were used in testing the first full-area stack. One type is referred to as "reference" gases which has been used at IGT for years as standard gases for evaluating the cell performance. At the anode, the "reference" gas is a 3:1 H₂:CO₂ gas mixture by volume, humidified to about 20% of water. After this gas mixture reacts through the water shift reaction in the anodic chamber, it is similar to the product of a naphtha reformer. At the cathode, the "reference" gas is a 70:30 Air:CO₂ gas mixture by volume.

The other type of gases, used for a short duration during the test, is referred to as "system" gases. At the anode, it is a 4:1 H₂:CO₂ gas mixture by volume, humidified to about 25% water. After this gas mixture shifts in the anodic chamber, it is similar to a product of natural gas reformer. At the cathode, the "system" gas is a mixture containing about 7-10% O₂, 8-10% CO₂, and balanced by N₂. This "system" gas simulates the concentrations of O₂ and CO₂ that would be expected in the cathodic chamber during operation of a total molten carbonate fuel cell system with cathode gas recycled for controlling the stack temperature.

This stack demonstrated uniform cell voltages while maintaining an average stack temperature of 650 °C as shown in Figure 1. A uniform profile was obtained at OCV condition and at high current density of 150 mA/cm², indicating that good gas flow distribution was achieved. Shown in Figure 2 is the history of power generation during the test. The stack was capable of producing steady-state power for both the "reference" and "system" gases at about 18 and 13 kW, respectively. For a brief period, the stack was operated at power output exceeding the 20 kW design capacity. The fuel utilization during this test was between 60 to 75%.

For commercial power generation, sometimes it may be necessary to stop the hot stack from producing power and cool it down to room temperature for maintenance operations and then re-start the stack for power generation. This procedure is commonly referred to as thermal cycling. During this test, after about 1300 test hours, the stack was cooled from 650 °C operating temperature and then successfully re-started to generate power at operating temperature. The duration of this thermal cycle (TC #1) was about 470 hours with about 180 hours at room temperature. After about another 150 hours of operation, the stack went through another thermal cycle (TC #2). This time the stack was only cooled down to 300 °C to allow a faster re-start. The duration for this thermal cycle was about 100 hours.

To see if thermal cycling would affect stack performance, a polarization run was made shortly after TC #1, at about 1850 hours. This polarization run was compared to the polarization run made around 500 test hours. As shown in Figure 3, there was no significant degradation in stack performance after TC #1. The history of stack performance of this first-full area stack is also summarized in Figure 4. As indicated by OCV, load, polarization loss, and internal resistance loss data, this stack appeared to have operated without significant loss of performance for the entire 2200 hours of testing.

SECOND FULL-AREA STACK TEST For this second full-area stack, the test was also conducted with "reference" and "system" gases. The definitions for these gases as used in the second full-area stack test are the same as those used in the first full-area stack test, except that in the second stack test, the composition of the anode "reference" gas was now defined to have the same composition as the anode "system" gas, a 4:1 H₂:CO₂ mixture, humidified to about 25% of H₂O.

The history of power generation for this stack test is shown in Figure 5. The stack produced maximum power of 23 kW on "reference" gases and 21 kW on "system" gases. During this test, another commercial mode of operation was simulated. This mode is referred to as "hot standby". During the "hot standby" period, the feed gases were switched from "system" gases to "inactive" gases to protect the stack while the stack was maintained at operating temperature in open circuit condition for about 140 hours. The stack quickly produced power as soon as the "system" gases were re-introduced.

The performance characteristics for the second full-area stack can be seen from a polarization run as shown in Figure 6. At high current density of 160 mA/cm², the average cell voltage was at 687 mV. This is equivalent to producing 23 kW power which exceeds the 20 kW design capacity for this stack.

FIRST AND SECOND FULL-AREASTACKS COMPARISONS Shown in Figure 7 is the comparison of polarization run data obtained from the first and the second full-area stack tests. Both polarization runs were obtained at the average stack temperature of 650 °C and using "reference" gases. As indicated earlier, the anode "reference" gas mixture used in the first stack was a 3:1 H₂:CO₂ mixture and in the second stack was a 4:1 H₂:CO₂ gas mixture. Calculations show that due to the difference in composition, the OCV for the second stack should be higher than the OCV of the first stack by about only 12 mV. As shown in Figure 7, the polarization curve for the second stack is higher the polarization curve of the first stack by about 7 to 10 mv. The corresponding power curves also show no significant difference between these two stacks. Thus, we can conclude that the performance characteristics of the full-area stack has been successfully duplicated using the manufacturing technology developed at M-C Power Corporation.

M-C Power is now designing and manufacturing active components needed for a commercial 250 kW stack to be demonstrated at a UNOCAL facility. One of the many factors need to be considered in design is the pressure drop characteristics for cathodic chamber. An empirical pressure drop correlation shown in Figure 8 was developed based on the pressure drop and flow data obtained from these two full-area stack tests. The data show that the pressure drop correlation gives good prediction. In other words, the pressure drop characteristics for both stacks are the same. Additionally, pressure drop predictions based on cold-flow model also agree well with the empirical pressure drop correlation. This empirical correlation also shows that at the anticipated cathode flow rates for the 250 kW stack operation, the expected pressure drops are well within the design constraint for the wet seal.

CONCLUSIONS The test results from these two full-area stacks have shown that using the manufacturing technology developed at M-C Power Corporation, the IMHEx configuration developed by IGT can be successfully implemented for commercial size stacks. During the test duration, both stacks were operated successfully and simulated "thermal cycling" and "hot standby" modes expected in commercial power generation. Within the experimental accuracy, the stack performance and cathode pressure drop characteristics have been successfully duplicated.

ACKNOWLEDGEMENTS The M-C Power Program is being funded by the Gas Research Institute, the Department of Energy, The Electric power Research Institute, and San Diego Gas & Electric Company. Significant cost sharing is being provided by M-C Power, IGT, Bechtel Corporation, Stewart & Stevenson Services, Southern California Edison, Southern California Gas Company, the South Coast Air Quality Management District, and UNOCAL.

acs.ppr

FIGURE 1. First Full-Area Stack Cell Voltages
(75% Fuel Utilization @ 150 mA/cm²)

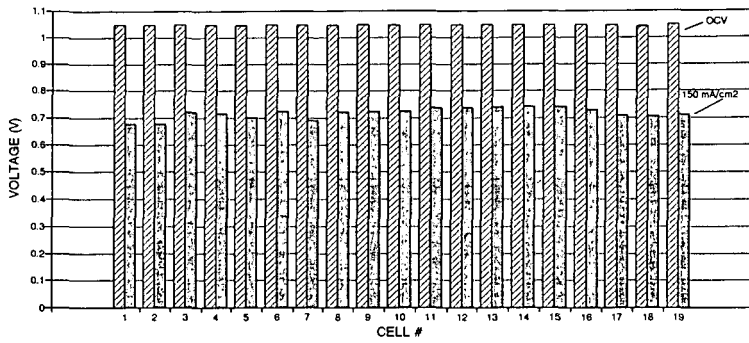


FIGURE 2. First Full-Area Stack Test
Stack Power vs. Time

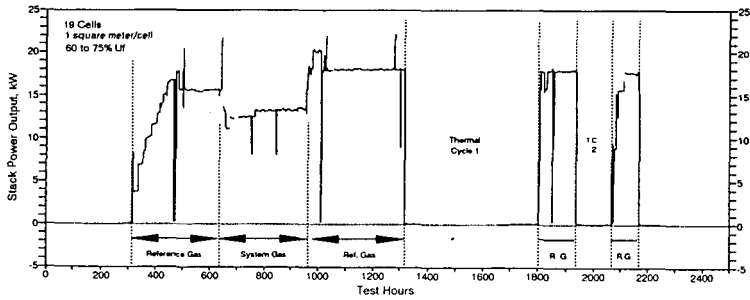


FIGURE 3. First Full-Area Stack Polarization
before and after Thermal Cycle

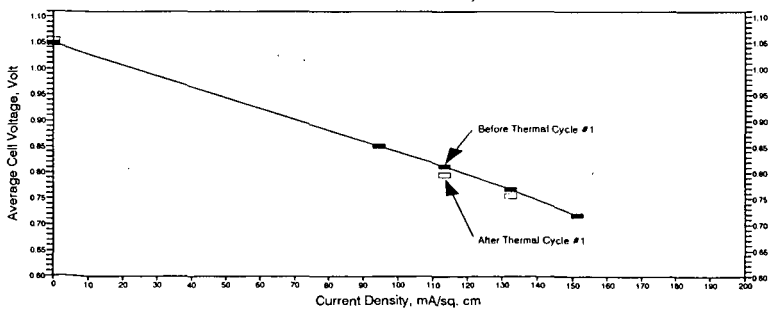


FIGURE 4. First Full-Area Stack Performance History

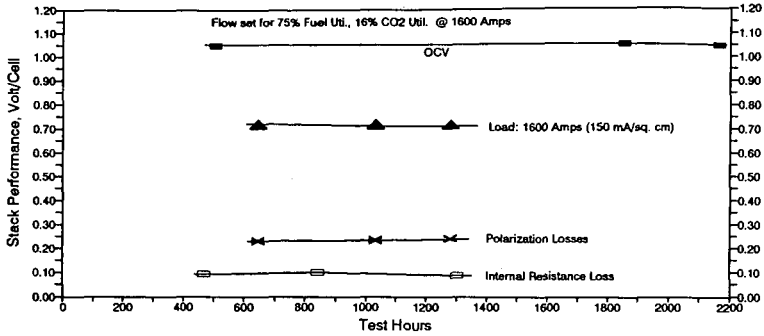


FIGURE 5. Second Full-Area Stack Test Stack Power vs. Time

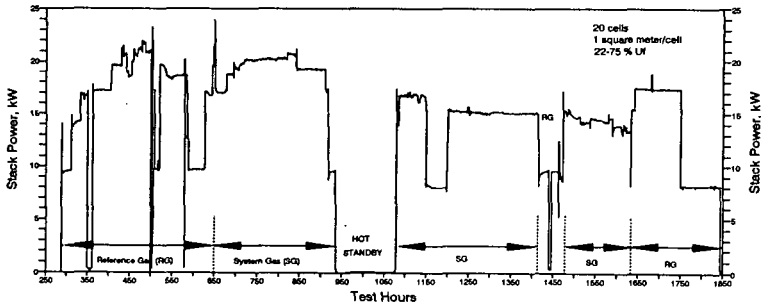


FIGURE 6. Second Full-Area Stack Polarization

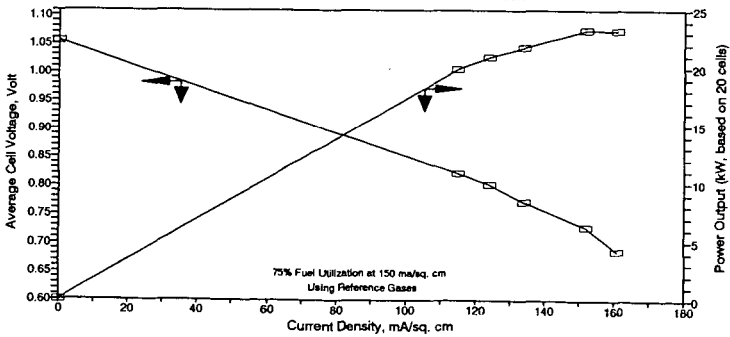


FIGURE 7. Comparison of Polarization Curves
First vs. Second Full-Area Stacks

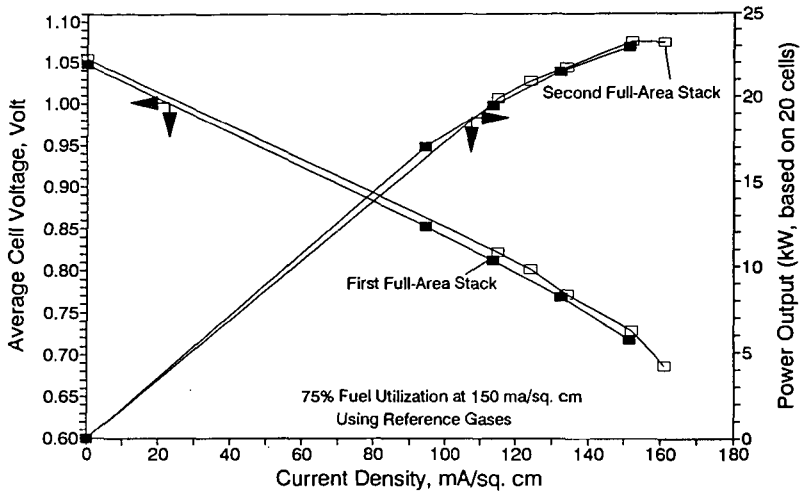
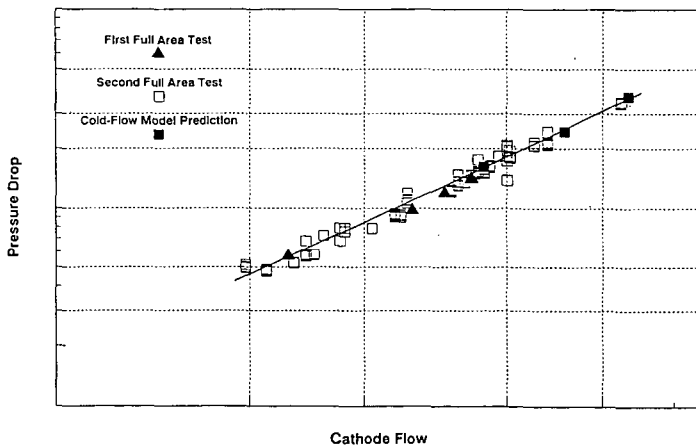


FIGURE 8

CATHODE PRESSURE DROP
Full-Area Tests



ADVANCED MOLTEN CARBONATE FUEL CELL COMPONENTS

D.S. Erickson
M-C Power Corporation
8040 South Madison Street
Burr Ridge, IL 60521

R. Remick and E. Ong
Institute of Gas Technology
3432 South State Street
Chicago, IL 60616

ABSTRACT

First-generation molten carbonate fuel cell electrodes and matrices have successfully been manufactured in the sizes and quantities required for commercial production. To meet the endurance and cost goals required for commercializing MCFC technology, a change in the active area materials may be required. Several advanced components, including stabilized cathodes and strengthened anodes, have been tested in bench scale cells with improved strength, endurance, and/or performance. This paper will discuss the status of advanced MCFC component development and the work remaining before they are selected for development for full-area manufacturing.

INTRODUCTION M-C Power Corporation (MCP) was formed in 1987 to commercialize Molten Carbonate Fuel Cell (MCFC) stacks based on the cell technology and internally manifolded stack concept developed by the Institute of Gas Technology (IGT). Since then, MCP has successfully built and operated two full-area subscale (20 kW) stacks with a third starting in May 1993.

MCP is currently manufacturing the active area components for the first internally manifolded commercial MCFC stack (250 kW) using first-generation active area components. Concurrent with the efforts to scale up the manufacturing processes has been an ongoing effort at MCP and IGT to test advanced component technologies to enable MCP to meet its future cost and performance goals. The following sections discuss some of the component technologies which are being developed by MCP and IGT for future commercialization at MCP.

SELECTION CRITERION FOR COMMERCIALIZATION IGT has been testing several advanced component technologies designed to lower the cost of the fuel cell stacks and increase their endurance and performance. After successfully fabricating 100-cm² size samples, components are evaluated in bench scale cells to monitor their performance under varying operational parameters. Out-of-cell testing is also utilized to demonstrate the improvements in performance and endurance. From these tests, target microstructures are determined for optimal cell performance and endurance.

The technologies that are currently being developed for full-area testing are showing progress toward meeting the performance goals (Figure 1) and the additional criterion involving the cost and ease of fabrication. The advanced components currently being developed for full-area manufacturing at MCP are the stabilized cathode and the low Cr anode.

STABILIZED CATHODE The stabilized cathode was developed to inhibit the NiO dissolution which could result in cell shorting at the target operational times and pressures. Lowering of the NiO dissolution of stabilized cathodes was demonstrated at the 100-cm² cell size with acceptable performance (Figure 2). The dissolution behavior and cell performance of the stabilized cathode at elevated pressures will be further defined in the pressurized 100-cm² test stands at MCP and IGT. This testing will further pinpoint the target microstructure, composition, and porosimetry for optimal performance.

Process development at MCP and IGT focuses on three areas: raw materials development, tape casting specification, and heat treating parameter specification. The raw materials for manufacturing the components for 100-cm² testing had been batch manufactured at IGT. The batch process has been modified for continuous manufacturing for production of commercial quantities of the stabilized cathode materials. Tape casting has been successful using techniques developed for the first generation of components. Scale up of the heat treating procedures has been successful at the 0.1 m² level with final scale up to 1 m² occurring when modifications to MCP's existing equipment is complete.

LOW Cr ANODE The low Cr anode was developed to enable us to retain the creep strength and cell performance of the baseline anodes, with half the Cr content of the first generation Ni-Cr anodes. Raw materials manufacturing development and development of the tape casting and heat treating procedures resulted in anodes with a uniform distribution of Cr. Creep behavior and cell performance were characterized and compared to baseline at the 100-cm² level. Components of 0.1 m² area have been tape cast and sintered using the production equipment at MCP.

The target microstructures were obtained, verifying the capability of the process to meet the specification developed from bench top testing. Raw materials have been produced in lot sizes sufficient for 20 kW stack production, and scale up of the manufacturing procedures for production of full-area low Cr anodes is ongoing at MCP.

CONCLUSION MCP has selected advanced components to represent the second generation of active area components. Commercialization of the raw materials and component fabrication procedures should be completed by the beginning of next year. A full-area, subscale (20 kW) stack is planned to verify performance improvements and identify further work toward commercial stack production using these components.

ACKNOWLEDGEMENTS The MCP Program is being funded by the Gas Research Institute, the Department of Energy, The Electric Power Research Institute, and San Diego Gas & Electric Company. Significant cost sharing is being provided by MCP, IGT, Bechtel Corporation, Southern California Edison, Southern California Gas Company, the South Coast Air Quality Management District, Stewart & Stevenson Services, and UNOCAL.

REFERENCES Work performed under MCP Subcontract MCP-9-IGT, DOE Contract No. DE-AC-21-90MC-27394.

Work performed under MCP Subcontract MCP-9-IGT, DOE Contract No. DE-AC21-90MC-27394.

Figure 1.
Bench Scale Cell Performance of
Low Cr Anode and Stabilized Cathode
(Cell BS-TC-92-3)

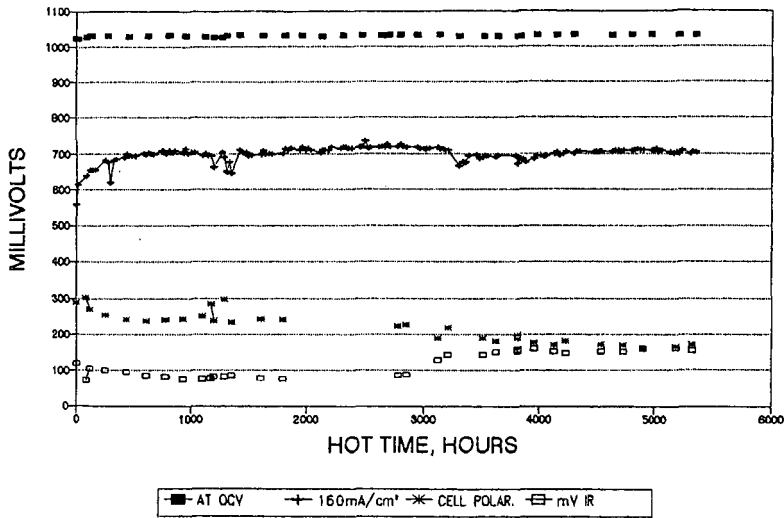
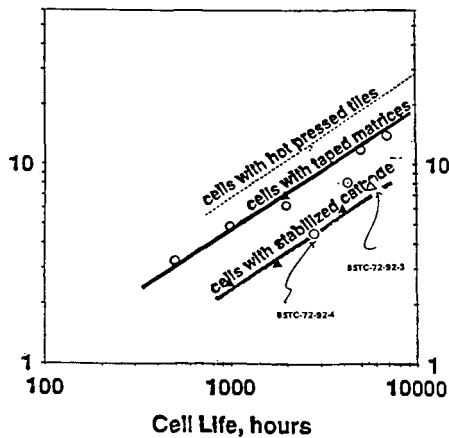


Figure 2.
Lowering of Ni Deposition in Matrix
for Cells Using the Stabilized Cathode



CATHODE MATERIALS FOR THE MOLTEN CARBONATE FUEL CELL

G. H. Kucera, A. P. Brown, M. F. Roche, E. J. Indacochea, M. Krumpelt, and K. M. Myles
Chemical Technology Division, Argonne National Laboratory, Argonne, IL 60439

Keywords: Lithium Ferrate Cathode, Lithium Cobaltate Cathode, Nickel Oxide Cathode

INTRODUCTION

The effort on near-term development and commercialization of the molten carbonate fuel cell (MCFC) is focused on its operation at ambient pressure. However, the long-term objective is operation at pressures of 5 to 10 times ambient. There are a number of benefits to operating the MCFC under pressure. Some, such as smaller piping and blower size, affect the system cost, and others, such as increased efficiency and higher power density, result from the cell operation itself. A major problem associated with pressurization is the accelerated rate of dissolution of the MCFC's nickel-oxide (NiO) cathode and the subsequent deposition of nickel near the MCFC's nickel anode (1). The dissolution of NiO in the MCFC electrolyte proceeds according to the following reaction, which is driven to the left with increasing CO₂ pressure: $\text{NiO} + \text{CO}_2 \rightarrow \text{Ni}^{2+} + \text{CO}_3^{2-}$. The Ni²⁺ in the electrolyte is reduced to nickel metal when it encounters the reducing conditions of the anode environment. The loss of nickel oxide from the cathode becomes critical if a short circuit results or if compaction of the cathode occurs. A solution to this problem is the development of alternative cathode materials.

The selection of an alternative to the NiO cathode is based on a number of criteria. These include 1) chemical stability in the cathode environment, 2) low solubility in the electrolyte, 3) high electronic conductivity, 4) an absence of precipitation mechanisms in the anode environment (as either the metal or an oxide), and 5) overpotential for oxygen reduction (from in-cell tests). Studies at Argonne National Laboratory have focused on the development of various ceramic oxides identified as having chemical stability in the cathode environment. Three of the more promising candidates are LiFeO₂, Li₂MnO₃, and LiCoO₂. This paper presents the results of studies of these materials with respect to the criteria listed above.

STABILITY

A properly designed stability test for an MCFC cathode reproduces the conditions of the cathode environment. These conditions include temperature, cathode gas, and electrolyte composition. Thus, the tests were conducted on candidate materials held at a temperature of 650°C in a 100 kPa (1 atm) cathode gas consisting of 14% O₂-28% CO₂-balance N₂. The candidate materials were wetted with the electrolyte, 70 mol% Li₂CO₃-30 mol% K₂CO₃, and, to ensure adequate gas access, the amount of electrolyte was controlled so that the materials were not flooded.

Various oxides of iron, manganese, and cobalt were tested under the above conditions. Because the phase rule indicates that each cation has only one stable compound, the test results were expected to be independent of the precursor oxide. Thus, Fe₂O₃, FeO, and Fe₃O₄ all produced LiFeO₂; MnO and Mn₂O₃ produced Li₂MnO₃; and CoO and Co₃O₄ produced LiCoO₂. These tests show that, under cathode conditions, the stable products are LiFeO₂, Li₂MnO₃, and LiCoO₂.

SOLUBILITY

The solubilities of LiFeO₂, Li₂MnO₃, and NiO in Li₂CO₃-K₂CO₃ melts sparged with cathode gas were determined by Kaun *et al.* (2, 3). Their studies (see Fig. 1) showed that, at 650°C, iron and manganese had lower solubilities than nickel. Therefore, both the LiFeO₂ and Li₂MnO₃ cathode materials showed promise because they

met two of the necessary criteria (chemical stability and low solubility).

The solubility of LiCoO_2 was measured under similar gas and electrolyte conditions at 650°C . Chemical analyses of electrolyte samples, taken periodically for times up to 300 h, showed about 0.5 wppm cobalt, a value also measured for a blank electrolyte sample containing no LiCoO_2 . Low cobalt solubility was also reported by Plomp *et al.* (4), who state that LiCoO_2 has a dissolution rate which is almost an order of magnitude lower than that of NiO at ambient pressure. The data from these solubility studies suggests that LiCoO_2 warrants further study as a cathode.

MIGRATION

As indicated above, one of the selection criteria is that a potential cathode material should not form either a metal precipitate or an oxide precipitate at the anode (reducing) side of an operating cell. The candidate materials LiFeO_2 , Li_2MnO_3 , and LiCoO_2 were assessed for their tendency to migrate toward the anode during cell operation (see "Cell Testing" section for a description of cell construction). Cells with LiFeO_2 and Li_2MnO_3 cathodes were operated only under open-circuit conditions, because the cathodes were not optimized for conductivity or electrode structure. The cells were operated for 2000 h and were quenched when the test was terminated so that any soluble cathode cations would remain in the electrolyte. The quenched electrolyte was analyzed by scanning electron microscopy/energy dispersive x-ray spectrometry (SEM/EDX) and by wet-chemical methods. Table 1 summarizes the results of the wet-chemical assays of electrolytes from the cells containing LiFeO_2 and Li_2MnO_3 cathodes and from a cell having a NiO cathode that was operated in a similar manner. The data showed that the concentrations of Fe and Mn from the cells with LiFeO_2 and Li_2MnO_3 cathodes were within the background scatter of the other cells. No evidence was found of either Fe- or Mn-containing deposits in the SEM/EDX measurements. These results, when taken with the above stability tests, showed that both LiFeO_2 and Li_2MnO_3 met three of the five criteria for an alternative cathode (chemical stability, low solubility, and a lack of migration).

Two LiCoO_2 cathodes were also tested in cells. These cells were operated under load; one for about 600 h, and the other for about 800 h. The components from the 600-h cell were examined by optical microscopy and SEM/EDX. The examinations revealed a small number of metallic deposits in the electrolyte tile near the anode and large crystalline deposits in the openings of the perforated sheet that serves as the cathode current collector. The SEM/EDX results showed that both deposits contained cobalt. The location of the deposits may be a reflection of the operating conditions, which varied from open circuit to a current density of 160 mA/cm^2 . The components from the 800-h cell are still under examination. However, preliminary SEM/EDX results showed a significant concentration of cobalt at the cathode/electrolyte-tile interface that extended about 200 μm into the 1.3-mm-thick tile. The cobalt concentration decreased through the next 300 μm until a background value was reached. Because the cobalt concentration has not, as yet, been quantitatively determined, it is not certain if its transport represents a life-limiting situation. Researchers at the Netherlands Energy Research Foundation (5) reported finding cobalt in the nickel anode. If the cobalt deposition rate is low, and if all cobalt deposits are located in the anode, then LiCoO_2 would still be a promising cathode.

CONDUCTIVITY

The conductivity of a material is important in determining its usefulness as an MCFC cathode, since the material must be capable of delivering electrons to reaction sites where CO_3^{2-} is formed from O_2 and CO_2 . The precise requirement for the conductivity of an alternative cathode material is unknown; however, an initial target was set at $0.1 \text{ ohm}^{-1}\text{cm}^{-1}$ at 650°C . This is about a factor of 10 lower than that of the NiO cathode. Our calculations (6) using an existing model (7) indicated that a thinner electrode of less conductive materials would give a performance equivalent to the NiO cathode.

Conductivity measurements as a function of temperature were employed to determine the electrical

properties of the candidate cathode materials. The measurements were made on sintered disks (about 2.5-cm dia x 0.2-cm thick) of LiFeO_2 , Li_2MnO_3 , and LiCoO_2 using the van der Pauw method (8). The conductivity of LiFeO_2 , Li_2MnO_3 , and LiCoO_2 in cathode gas (14% O_2 -28% CO_2 -balance N_2) is shown in Fig. 2 as a function of temperature. The data showed that the conductivity at 650°C (the typical MCFC operating temperature) was about $0.003 \text{ ohm}^{-1}\text{cm}^{-1}$, $0.0014 \text{ ohm}^{-1}\text{cm}^{-1}$, and $1 \text{ ohm}^{-1}\text{cm}^{-1}$ for LiFeO_2 , Li_2MnO_3 , and LiCoO_2 , respectively. The values for LiFeO_2 and Li_2MnO_3 were too low for cathode use. However, their response to temperature is typical of a semiconductor. The electrical conductivity of a semiconductor depends on its charge-carrier concentration and carrier mobility and can be increased by dopants that increase the number and/or mobility of charge carriers.

Doping of LiFeO_2 . Because the conductivity of LiFeO_2 was about a factor of 30 lower than the target value of $0.1 \text{ ohm}^{-1}\text{cm}^{-1}$, dopants were incorporated to improve its conductivity. The dopants Mn, Co, and Cu were successfully incorporated into the LiFeO_2 lattice. Manganese-doped LiFeO_2 was studied more extensively than the others. Manganese was added to the LiFeO_2 lattice until the incorporation limit was reached. This occurred when the mole ratio of manganese to iron was about 1:7. The result of these additions was that the conductivity at 650°C was increased from $0.003 \text{ ohm}^{-1}\text{cm}^{-1}$ to about $0.04 \text{ ohm}^{-1}\text{cm}^{-1}$. The correlation between dopant concentration and conductivity (Fig. 3) and between dopant concentration and lattice parameter (Fig. 4) indicated that the dopant was fully incorporated and homogeneously distributed in the parent material.

Cobalt-doped LiFeO_2 was studied at dopant concentrations ranging from 5 to 14 mol%. The conductivity at 650°C as a function of dopant concentration is shown in Fig. 5. The data show good correlation between dopant concentration and conductivity with the maximum conductivity being $0.1 \text{ ohm}^{-1}\text{cm}^{-1}$ when the mole ratio of cobalt to iron is about 1:8.

Copper-doped LiFeO_2 was studied at two concentrations, 10 and 20 mol% Cu. At a dopant concentration of 10 mol% Cu, the conductivity at 650°C was about $0.08 \text{ ohm}^{-1}\text{cm}^{-1}$. At 20 mol% Cu, the conductivity was similar to that of the material with 10 mol% Cu, but a second phase consisting of CuO was present. This shows that the incorporation limit was exceeded at the higher concentration of CuO .

The conclusions to be reached from the above studies are that the charge-carrier concentration is proportional to the dopant concentration, the conductivity of LiFeO_2 can be enhanced with the use of dopants, and the target value of $0.1 \text{ ohm}^{-1}\text{cm}^{-1}$ can be achieved with doped LiFeO_2 . Of the three dopants initially studied, only cobalt and copper were evaluated further.

Doping of Li_2MnO_3 . As noted above, the conductivity of undoped Li_2MnO_3 (about $0.0014 \text{ ohm}^{-1}\text{cm}^{-1}$) is too low for cathode use. As with LiFeO_2 , doping was employed to increase the conductivity. Six dopants (Mg, Ca, Zn, Al, Nb, and W) were initially selected, but only Mg, Zn, and Nb showed promise. The conductivities at 650°C of Li_2MnO_3 with several concentrations of these three dopants are given in Table 2. The highest concentration shown in Table 2 for each dopant is its limit of incorporation. The conductivity, even though it was increased by a factor of nearly sixty by niobium ($0.0014 \text{ ohm}^{-1}\text{cm}^{-1}$ when undoped vs $0.08 \text{ ohm}^{-1}\text{cm}^{-1}$ for Nb doped), was still below the target value. However, these doping studies demonstrated that the charge-carrier concentration could be increased through incorporation of a dopant in the crystal lattice of the parent material. Despite their low conductivities, both the Nb- and Mg-doped Li_2MnO_3 were evaluated further to determine their conduction mechanisms.

Seebeck Coefficients. The Seebeck coefficient ($\mu\text{V/K}$) is the potential difference generated by applying a temperature gradient to a conductive material. The sign of the Seebeck coefficient is the same as the sign of the dominant charge carrier. Thus, when the coefficient is negative, electrons are the dominant charge carriers, and, when it is positive, holes are the dominant charge carriers. A measurement of the Seebeck coefficient, therefore, provides information concerning the conduction mechanism of the material. A p-type conductor, where hole conduction dominates, is desired for a cathode material.

Seebeck-coefficient measurements were made on LiFeO_2 doped with Co^{2+} and Cu^{2+} , on Li_2MnO_3 doped with Nb^{5+} and Mg^{2+} , and on undoped LiCoO_2 . The measurements were made over a range of temperatures and employed a cover gas of 14% O_2 -28% CO_2 -balance N_2 . Figure 6 shows the results of these measurements for the temperature range of 600 to 800°C. The Seebeck coefficients for the Nb- and Mg-doped Li_2MnO_3 were negative, indicating that both are n-type semiconductors, where electrons are the dominant charge carriers. These data suggested that Nb^{5+} substituted on Mn^{4+} sites and that Mg^{2+} substituted on Li^+ sites. In both cases, the conduction mechanism was electron hopping between the parent cation Mn^{4+} and Mn^{3+} . The Seebeck results combined with the conductivity results suggested that Nb- and Mg-doped Li_2MnO_3 were not good candidates for the MCFC cathode, because p-type conduction is desired.

The Seebeck coefficient for the Co-doped LiFeO_2 was positive and nearly constant throughout the temperature range studied. The positive coefficient indicated that the material was a p-type conductor; the small slope indicated little or no concentration of electrons as charge carriers. The Cu-doped LiFeO_2 changed from a p-type to an n-type conductor at about 675°C, a temperature within the typical operating temperature range of an MCFC. Therefore, of the doped materials assessed, only the Co-doped LiFeO_2 material appeared to be a good candidate for testing as a cathode.

The Seebeck data for undoped LiCoO_2 showed that this material was also a p-type conductor (its coefficients were positive). The good conductivity and the positive Seebeck coefficient of undoped LiCoO_2 suggested that the material was nonstoichiometric with respect to lithium and/or oxygen. Excess lithium (substituted on a cobalt site) or interstitial oxygen would give the observed characteristics. This material continues to be a good candidate for an alternative cathode.

CELL TESTING

Both full and half cells were used to test the cathodes. The 25-cm² full cells contained the candidate cathode, a nickel-chrome anode, and an electrolyte tile containing 50 vol% electrolyte (70 mol% Li_2CO_3 -30 mol% K_2CO_3) and 50 vol% LiAlO_2 . The cathode-gas composition was generally varied to determine the effects of O_2 and CO_2 pressures on cathode performance. The anode gas was 80 mol% H_2 -20 mol% CO_2 . The 2.5-cm² half cells contained the candidate cathode, again with a range of cathode gases, a gold reference electrode bathed in the same cathode gas, and a Type 316 stainless-steel counter electrode employing carbon dioxide gas as the reductant ($\text{CO}_2 + 2\text{e}^- \rightarrow \text{CO} + \text{O}^{2-}$). The cells were typically operated at 650°C.

Half-Cell Tests of Co-doped LiFeO_2 . The effect of cathode-gas composition on the performance of a Co-doped LiFeO_2 cathode was measured over a range of oxygen partial pressures (5 to 70 kPa) at a fixed carbon dioxide partial pressure (30 kPa). The results are shown in Fig. 7. The data at 160 mA/cm² show a dramatic increase in performance (decrease in overpotential) with increasing O_2 partial pressure (i.e., about 300 mV on increasing the O_2 partial pressure from 5 to 70 kPa). The best performance was still about 75 mV poorer than that of NiO; however, under operation at ten times ambient pressure, the O_2 partial pressure is expected to be higher than 70 kPa. The performance of the cathode was also examined over a range of carbon dioxide partial pressures (5 to 60 kPa) at a fixed oxygen partial pressure (15 kPa). The results are shown in Fig. 8. The data at 160 mA/cm² showed an unexpected trend; the best performance occurred at the lowest partial pressure of CO_2 .

Both the O_2 and CO_2 partial pressures affected the performance of the Co-doped LiFeO_2 cathode, and the greatest changes were seen at current densities greater than 100 mA/cm². Based on these results, an alternative cathode-gas mixture was formulated to take advantage of the gas-composition effects and attain the best cathode performance. The mixture consisted of 20% O_2 , 5% CO_2 , balance N_2 . This cathode gas yielded good cathode performance; the test results are shown in Fig. 9. The performance of a NiO cathode operated in a half cell is shown for comparison. The data show that the alternative cathode gas results in a performance similar to that of a cathode gas having an O_2 partial pressure of 70 kPa.

Full-cell Tests of Co-doped LiFeO₂. Cobalt-doped LiFeO₂ cathodes were operated in full cells to determine if the altered cathode gas, which gave improved performance in the half-cell test, would have similar benefits in full cells. The polarization curves for a cell operated at ambient pressure with a Co-doped LiFeO₂ cathode and tested with the standard cathode gas (14% O₂-28% CO₂-balance N₂) and with an altered cathode gas (80% O₂-20% CO₂) are shown in Fig. 10. The data show that at a current density of 120 mA/cm² the voltage of the LiFeO₂ cathode under altered gas conditions is 300 mV higher than under standard gas conditions.

Full-cell Tests of LiCoO₂. Lithium-cobaltate cathodes were tested in full cells under conditions similar to those used with the Co-doped LiFeO₂ cathodes. The polarization curves for a cell operated at ambient pressure and tested with the standard cathode gas and with an altered cathode gas (64% O₂-36% CO₂) are shown in Fig. 11. The data indicated an increase in performance when the O₂ partial pressure was increased from 14 kPa to 64 kPa. With altered cathode-gas conditions, the performance was equivalent to that of NiO with the standard cathode gas.

CONCLUSIONS

Both LiFeO₂ and Li₂MnO₃ were stable in the cathode environment, had low solubility, and were non-precipitating in the anode environment. Dopants were employed to enhance the electronic conductivity of both materials. Cobalt-doped LiFeO₂ was a factor of 30 more conductive than the undoped LiFeO₂; Nb-doped Li₂MnO₃ was a factor of 60 more conductive than its undoped form. However, only the Co-doped LiFeO₂ exhibited the desired p-type conduction. Half- and full-cell tests with Co-doped LiFeO₂ as the cathode material showed that its performance strongly depended on the oxygen partial pressure. Under simulated high-pressure conditions, where the O₂ partial pressure was 70 kPa, the performance was good.

The LiCoO₂ material had low solubility and was a good electronic conductor in the undoped form. In addition, it exhibited p-type conduction, and, when used as a cathode material, gave good cell performance. It precipitated as cobalt metal under the reducing conditions present in the anode. However, neither the rate of deposition nor the conditions influencing the deposition and location of deposits are known at present.

Further study of the Co-doped LiFeO₂ cathode under pressurized conditions is needed to determine if the performance projections are realistic. Further study of the LiCoO₂ cathode is also needed to determine if its dissolution and deposition in the anode are life limiting.

ACKNOWLEDGMENTS

This research was sponsored by the U. S. DOE Morgantown Energy Technology Center. Argonne National Laboratory is operated by the University of Chicago for the U. S. DOE under Contract W-31-109-Eng-38. J. R. Stapay conducted the measurements of Seebeck coefficients.

REFERENCES

1. W. M. Vogle, L. J. Bregoli, H. R. Kunz, and S. W. Smith, "Stability of NiO Cathodes in Molten Carbonate Fuel Cells," *Proc. Electrochem. Soc.* **84-13**, pp. 443-451 (1984).
2. T. D. Kaun, T. M. Fannon, and B. A. Baumert, "Solubility of Proposed Cathode Materials for Molten Carbonate Fuel Cells," *Extended Abstracts, 166th Electrochem. Soc. Meeting*, **84-2**, pp. 76-77 (1984).
3. T. D. Kaun, "Solubility of the NiO Fuel Cell Cathode in Li₂CO₃-K₂CO₃ Melts as Determined by Cyclic Voltammetry," *Proc. Fourth International Symp. on Molten Salts*, M. Blander *et al.*, eds., 163rd *Electrochem. Soc. Meeting*, **84-2**, pp. 489-497 (1984).
4. L. Plomp, J. B. J. Veldhuis, E. F. Sitters, F. P. F. van Berkel, and S. B. van der Molen, "Status of MCFC Materials Development at ECN," *Proc. International Fuel Cell Conference, Makuhari, Japan*, Feb. 3-6, 1992.
5. S. B. van der Molen, private communications (1993).

6. J. L. Smith, G. H. Kucera, and A. P. Brown, "Development of Cathode Materials and Structures for the Molten Carbonate Fuel Cell," Proc. Second Symp. on Molten Carbonate Fuel Cell Technology, J. R. Selman *et al.*, eds., 90-16, (1990).
7. G. Wilemski *et al.*, "Molten Carbonate Fuel Cell Performance Model Update-Final Report," DOE/FE/15978-1742 (1985).
8. L. J. Van der Pauw, Philips Research Reports, 13, 1 (1958).

Table 1. Electrolyte Analysis for Cathode Cations
(2000 h Test)

	Cations (wppm)		
	Fe	Mn	Ni
Unused Electrolyte	23	4	<3
Electrolyte from Li_2MnO_3 Cathode Cell	64	19	30
Electrolyte from LiFeO_2 Cathode Cell	59	5	10
Electrolyte from NiO Cathode Cell	60	1	162

Anode Gas: 64 mol% H_2 -16 mol% CO_2 -20 mol% H_2O .
Cathode Gas: 27 mol% O_2 -53 mol % CO_2 -20 mol % H_2O .

Table 2. Conductivity of Doped Li_2MnO_3 at 650°C

Dopant	Mole Fraction Dopant/Mn	$\sigma(\text{ohm}^{-1}\text{cm}^{-1})$
Mg	0.01	0.0067
	0.025	0.014
	0.05	0.05
Zn	0.013	0.0068
	0.025	0.01
	0.05	0.012
	0.08	0.04
Nb	0.013	0.0047
	0.025	0.0075
	0.05	0.01
	0.075	0.08

Figure 1. Solubilities of Nickel Oxide and Alternative Cathode Materials as a Function of Temperature

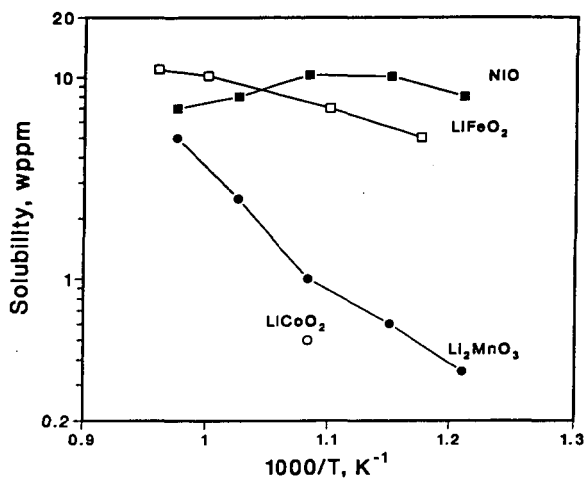


Figure 2. Conductivities of Alternative Cathode Materials (undoped) as a Function of Temperature

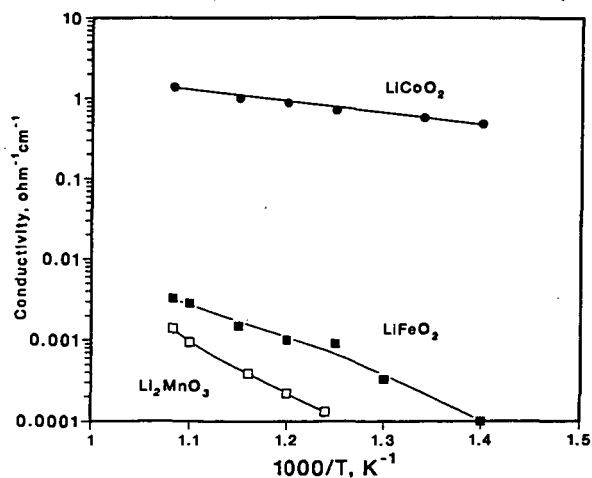


Figure 3. Conductivity of Mn-doped LiFeO_2 as a Function of Dopant Concentration

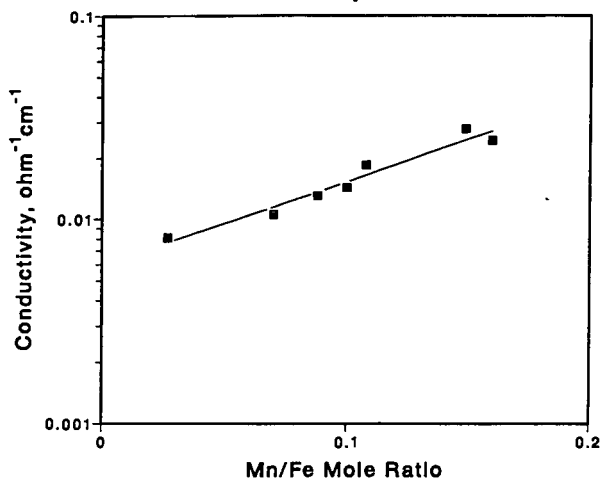


Figure 4. Lattice Parameter Change of Mn-doped LiFeO_2 as a Function of Dopant Concentration

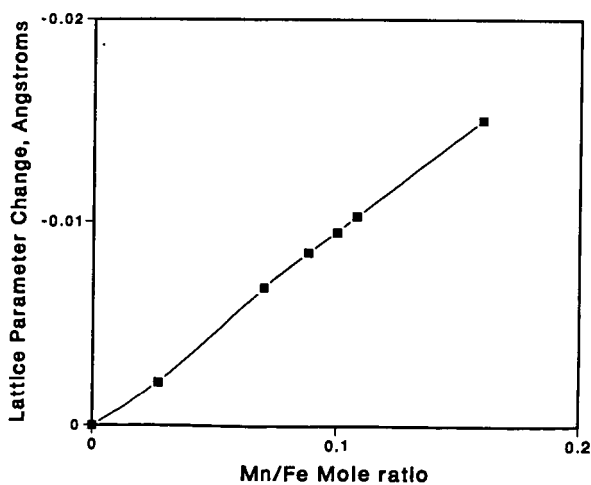


Figure 5. Conductivity of Co-doped LiFeO_2 as a Function of Dopant Concentration

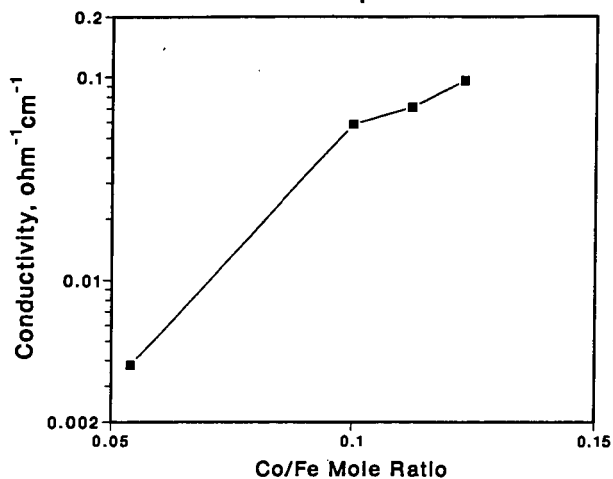


Figure 6. Seebeck Coefficients of Doped LiFeO_2 and Li_2MnO_3 and Undoped LiCoO_2

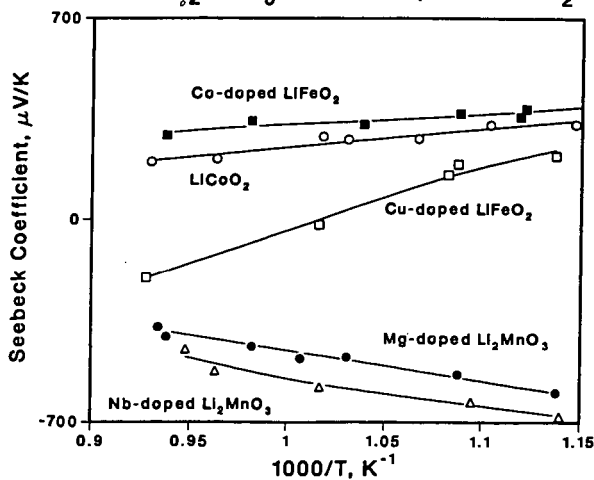


Figure 7. Polarization Curves for Co-doped LiFeO_2 at 650°C as a Function of O_2 Partial Pressure ($\text{CO}_2 = 30\%$ and $\text{O}_2 + \text{N}_2 = 70\%$)

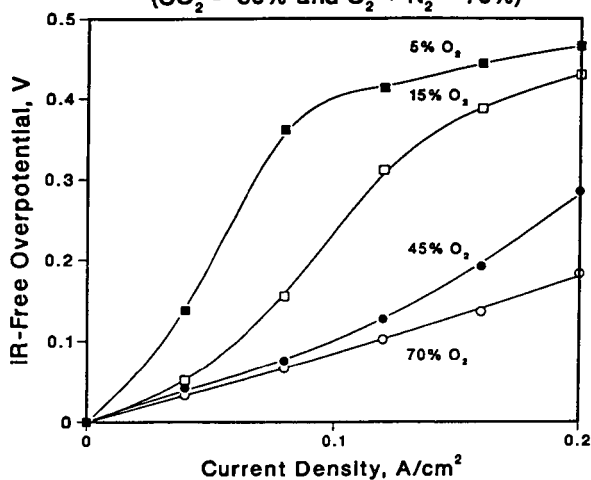


Figure 8. Polarization Curves for Co-doped LiFeO_2 at 650°C as a Function of CO_2 Partial Pressure ($\text{O}_2 = 15\%$ and $\text{CO}_2 + \text{N}_2 = 85\%$)

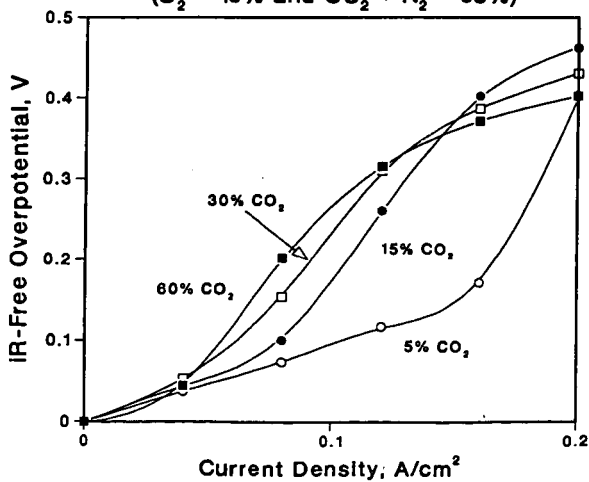


Figure 9. Performance of Co-Doped LiFeO_2 Cathode
In 20% O_2 -5% CO_2 -Bal. N_2 and NIO Cathode
In 14% O_2 -28% CO_2 -Bal. N_2

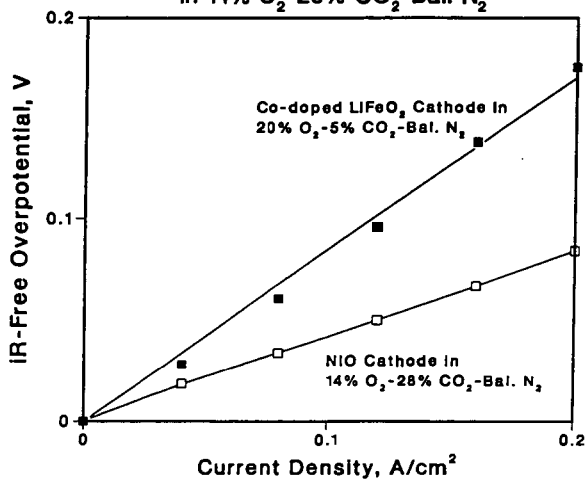


Figure 10. Polarization Curves from an MCFC with a Co-Doped LiFeO_2 Cathode In 80% O_2 -20% CO_2 and 14% O_2 -28% CO_2 -58% N_2

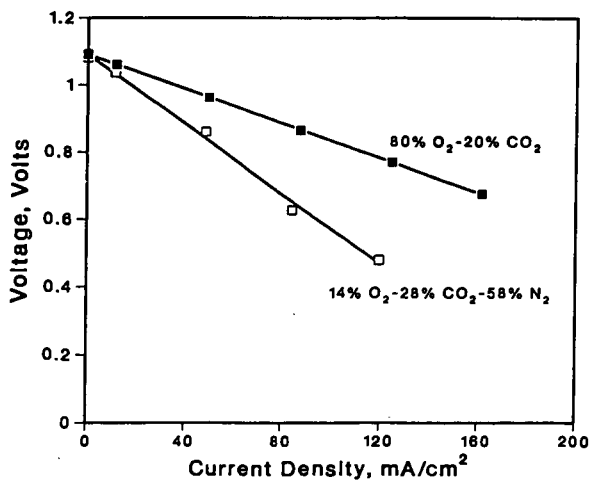
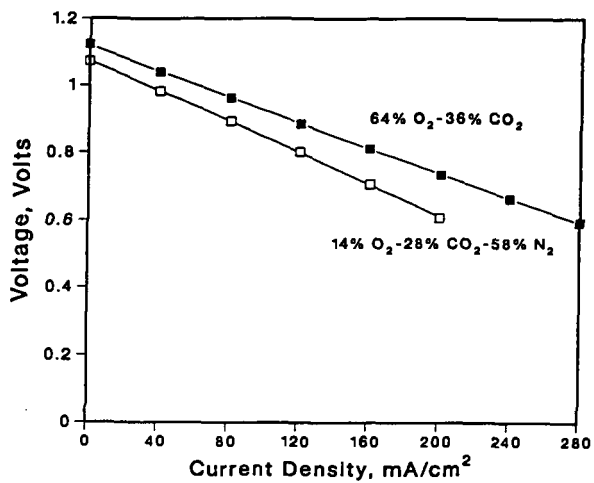


Figure 11. Polarization Curves from an MCFC with a LiCoO_2 Cathode in 64% O_2 -36% CO_2 and 14% O_2 -28% CO_2 -58% N_2



NiO CATHODE DISSOLUTION IN THE MCFC: A REVIEW

J.R. Selman, M.S. Yazici and Y. Izaki*

Department of Chemical Engineering

I.I.T., Chicago, IL

* Central Research Institute of Electric Power Industry
Yokosuka, Japan

ABSTRACT

The slow dissolution of the NiO cathode and precipitation of nickel particles in the electrolyte tile, leading eventually to short circuit, are key phenomena limiting the long-term performance of the MCFC. Although much work has been devoted to analysis of the nickel dissolution/shorting phenomenon, there are still many aspects which are not sufficiently understood to allow a confident prediction of lifetime. In particular, the driving force for displacement of the nickel precipitate particles and the mechanism by which they interact, leading to short circuit, are far from clear. The experimental data available thus far are critically reviewed and information necessary for a more complete quantitative understanding is identified.

1. INTRODUCTION.

The molten carbonate fuel cell (MCFC) is an energy producing electrochemical system which is expected to become commercial in the near future[1]. However, it remains a challenge to achieve the aimed-for lifetime of 40,000 h, especially in pressurized operation with fuel gas generated by coal gasification. Among the most important causes of limited lifetime is the dissolution of the cathode. In MCFC stacks operated thus far, the cathode material is lithiated nickel oxide. This material has good catalytic properties and a more than adequate electrical conductivity. However its solubility in the commonly used $\text{Li}_2\text{CO}_3\text{-K}_2\text{CO}_3$ electrolyte, at 650°C, though only tens of ppm, causes problems. Dissolved nickel is transported from the porous cathode into the electrolyte tile. There it is reduced to metallic nickel, presumably by chemical reaction with dissolved hydrogen, and precipitates as particles. Cathode dissolution has serious implications for long-term cell performance. This is not so much due to the loss of active cathode material, as to the accumulation of metallic nickel in the tile. Especially in large cells, this can eventually lead to a high-ohmic short which causes performance decline.

The implications of cathode dissolution for long-term performance of the MCFC have been recognized early, and much work has been done to circumvent or alleviate the problem. Alternative cathode materials have been pursued. However, such materials, which must be less soluble than nickel oxide or less easily reduced upon contact with dissolved fuel gas in the tile, are few in number and may require a remodeled cell design. On the other hand, certain additives which enhance the basicity of the electrolyte have been found to retard cathode dissolution, at least initially. Williams and George [2], reviewing the status of this issue as of 1991, do not consider it an impediment to commercial stack development, but emphasize the need for a better understanding of the phenomenon. The challenge is to quantify the factors which delay or accelerate it. The following is a brief summary of the

most important experimental findings and interpretations, with the purpose to assemble elements for a comprehensive predictive model.

2. EXPERIMENTAL OBSERVATIONS

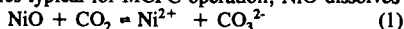
Small metallic nickel inclusions are found in the electrolyte of MCFC cells after thousands of hours. These particles are initially concentrated in a rather narrow zone, but are found later in a gradually widening band (see Section 6). The information available in the literature largely concerns the quantity of nickel deposited in the tile as a function of time. Kishida [10] reviewed MELCO data up to 1990 for hot-pressed and tape-cast matrices (of different thickness) in cells operated up to 10,000 h. He concluded that the nickel precipitation rate is approximately constant, approximately $4 \mu\text{g}/\text{cm}^2\cdot\text{h}$. Urushibata [11] arrived at a similar conclusion and value. Other authors [3,4,12], however, conclude that beyond 2000 h the dissolution rate decreases. They correlate their data with the square root of time, as illustrated in Figs. 1 and 2. It is difficult to resolve this discrepancy because of the large scatter in data points, as Fig. 1 illustrates. In addition, long-term data are relatively scarce. In such tests shorting effects may start to occur, caused by accumulation of nickel (see Section 7), which of course affect further precipitation.

3. INITIAL INTERPRETATION

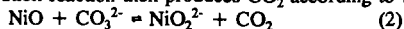
Since the earliest observations it has been assumed that nickel precipitation is caused by reduction of dissolved nickel (e.g., Ni^{2+} ions) reacting with hydrogen counterdiffusing from the anode toward the cathode. This is shown schematically in Fig. 3. If the electrolyte tile is without defect and the reduction of dissolved nickel occurs by means of a fast chemical reaction, the nickel particles should first accumulate in a sharply defined reaction zone. Based on this assumption one can apply known, or estimated, solubilities and diffusivities in molten carbonate to predict the location of the reaction zone. As discussed in the next section, there are important uncertainties in both nickel solubility and diffusivity. The calculations show that with hydrogen-rich fuel gas and standard oxidant, the reaction zone lies closer to the cathode than to the anode, in agreement with experimental observations. However, this "diffusion-reaction" model does not explain the time-dependent behavior of the precipitation.

4. SOLUBILITY OF NiO

Because it is considered a primary controlling parameter, the solubility of NiO in carbonate melts of various compositions and temperatures has been determined, for a range of gas compositions [2,13]. The generally accepted conclusion from this work is that under CO_2 partial pressures typical for MCFC operation, NiO dissolves according to the equilibrium:



The saturation solubility of NiO thus depends on the acid-base properties of the molten carbonate or carbonate mixture since the first step in this mechanism presumably produces Ni^{2+} and O^{2-} ions. This acid mechanism applies in low- O^{2-} activity ("acid") melts, while in "basic" (high- O^{2-} activity) melts the initial step may be association of NiO and O^{2-} . The overall "basic" dissolution reaction then produces CO_2 according to the equilibrium:



Therefore, the saturation solubility of nickel oxide shows a minimum, whose location depends on the composition and temperature of the carbonate mixture, as illustrated in Fig. 4. Recent data of Ota et al. [13] indicate a minimum solubility in Li-K carbonate eutectic at 650°C of

approximately 1 molar ppm, at a partial pressure of 0.01 atm CO_2 ; both the minimum solubility and the associated CO_2 partial pressure increase with temperature. Fig. 4 also shows that an increased Li^+/K^+ ratio lowers NiO solubility under CO_2 partial pressures typical for normal MCFC operation. As Fig. 2 illustrates, small additions of alkaline-earth carbonates have a significant effect on NiO solubility, presumably due to the enhanced basicity of the melt. Direct addition of alkaline-earth metal oxides to the cathode appears to decrease the NiO solubility even further, but the effect may be temporary.

5. SPECIATION AND TRANSPORT OF DISSOLVED NICKEL

To understand the accumulation of nickel in the tile, it has generally been assumed that the transported species is Ni^{2+} , based on the thermodynamic equilibrium discussed in the previous section. However, there is actually reason to doubt that the species is as simple as that. If the concentration of dissolved nickel at the boundary between cathode and electrolyte tile is assumed to equal the saturation solubility of nickel, the resulting flux into the electrolyte to the initial precipitation zone would be several times higher than that measured experimentally. The calculated flux, however, is based on scarce experimental data for the diffusivity of dissolved Ni^{2+} , which may be too high. The occurrence of Ni complexes cannot be excluded, or at the very least Ni^{2+} may be more strongly coordinated with the large CO_3^{2-} ions than with alkali ions. Molecular dynamic calculations have shown that this is likely to occur and that it can cause a significantly lower mobility of dissolved nickel [14]. Thus the actual flux may be smaller than calculated. In any case, in modeling of cathode dissolution, the diffusivity of dissolved nickel should not be treated simply as an a priori fixed parameter.

A different way to account for the lower-than-expected nickel flux is to assume a kinetic rate limitation of the NiO dissolution in the cathode, so that the nickel concentration in the cathode is not equal to the saturation concentration. This assumption was adopted in a systematic study by Shores, et al. [8]. They applied a simple transport model combining diffusion and convection (due to the net flux of carbonate ions) with slow dissolution kinetics, characterized by a forward rate constant. The convective velocity and the rate constant were treated as adjustable parameters. There is some justification for assuming a kinetic limitation of NiO dissolution, as suggested by dissolution transients in bulk carbonate melt (Fig. 5). This modeling approach yields a convective velocity of plausible magnitude and a fairly consistent set of kinetic parameters. It also predicts fairly well how NiO dissolution depends on applied current, as shown in Fig. 6. However, the reality of a kinetic limitation is not established without a doubt.

A different but more probable cause for depressed NiO solubility in the cathode is the high degree of basicity expected in the pores of the cathode under load, due to the slow recombination kinetics of O^- ions and CO_2 [15].

6. PRECIPITATION, PARTICLE MOVEMENT AND SHORTING

There are ample reasons to assume that the nickel particles precipitated by reduction of dissolved nickel are unstable, and that some of them grow at the expense of others (Ostwald ripening). The overall growth of nickel particles, of course, must correspond to the flux of nickel into the tile, but the latter must also drive the spreading of the precipitation zone. This phenomenon, qualitatively similar to that of periodic precipitation (Liesegang rings), presents

one of the most difficult to analyze aspects of NiO dissolution and precipitation/shorting. A key question concerns the role played by the net flux of CO_3^{2-} ions in the convection of particles.

The number density and distribution of particles is important intermediate information in trying to establish a correlation between the nickel content of the electrolyte and the occurrence of shorting. Kunz and Pandolfo [16] have indicated a way to establish such a correlation, however, without considering specific features of the particle distribution. important to predict. For improved prediction, a more accurate representation of convection would be desirable, and particle distribution must be accounted for. Systematic data (Fig.7) are now becoming available which should help to verify such a correlation.

ACKNOWLEDGMENT

This work was supported by the U.S. Department of Energy, Morgantown Energy Technology Center, under contract DE-AC21-86MC 23263.

REFERENCES

- [1] J.R. Selman, "Research, Development and Demonstration of Molten Carbonate Fuel Cell Systems", in "Fuel Cell Systems"(L.J. Blomen and K. Mugerwa, Ed.), Plenum, London(1993)
- [2] M.C. Williams and T.J. George, "Cathode Corrosion in Molten Carbonate Fuel Cells", Proc.26th Intersoc.Energ. Conv. Eng. Conf.(1991)
- [3] H. Kasai and A. Suzuki, Proc. 3rd Int. Symp. Carbonate Fuel Cell Technology, PV 93-3, The Electrochemical Soc. Inc., Pennington, NJ, p.240 (1993)
- [4] K. Yamashita and K. Murata (Toshiba Corp., Kawasaki, Japan), Priv. Comm.(1990)
- [5] K.N. Lee and D.A. Shores, J.Electrochem.Soc. 137, 859 (1990)
- [6] Y. Qu, G. Zhao and D.A. Shores, "The Dissolution of NiO in Molten Carbonate Mixtures", in Proc. 2nd Symp. Molten Carbonate Fuel Cell Technology, PV90-16, The Electrochemical Society Inc., Pennington, NJ, p.338 (1990)
- [7] E.T. Ong, "MCFC Endurance Issues", in Proc.Intern.Fuel Cell Conf. Makuhari (Japan), p.219 (1992)
- [8] D.A. Shores, J.R. Selman, S. Israni and E.T. Ong, in Proc. 2nd Symp. Molten Carbonate Fuel Cell Technology, PV90-16, The Electrochemical Society Inc., Pennington, NJ, p.290 (1990)
- [9] Y. Mugikura, Y. Izaki, T. Watanabe, E. Kouda, H. Kinoshita, T. Abe, "Development Status of MCFC at CRJEP", in Fuel Cell Seminar Abstracts (1992)p.109
- [10] K. Kishida, Ber. Bunsen Ges. Phys. Chem. 94, 941 (1990)
- [11] H. Urushibata, "Life Issues of MCFC" in Proc.Intern. Fuel Cell Conf., Makuhari (Japan), p.1223 (1992)
- [12] J.B.J. Veldhuis, S.B. van der Molen, and R.C. Makkus, Ber. Bunsen Ges. Phys.Chem. 94, 947 (1990)
- [13] K. Ota, S. Mitsuhashi, K. Kato, and N. Kamiya, in Proc. 2nd Symp. Molten Carbonate Fuel Cell Technology, PV 90-16, The Electrochemical Society Inc., Pennington NJ, p.318 (1990)
- [14] J. Tissen and G. Janssen (ECN, The Netherlands), Private Communication (June 1992)
- [15] S.H. Lu and J.R. Selman, J.Electrochem.Soc. 137 (1990) 1125.
- [16] H.R. Kunz and J.W. Pandolfo, J.Electrochem.Soc. 139, 1549 (1992)

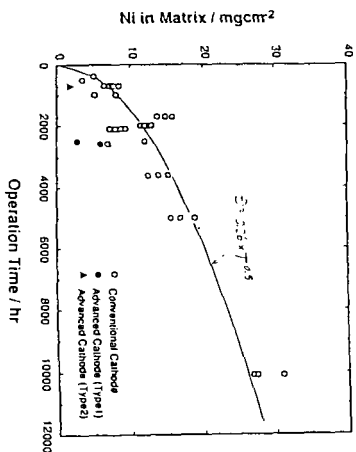


Fig. 1. Nickel in the tiles of 100-cm²(single) to 1400-cm²(stack)cells, as a function of operating time under average current density 150 mA/cm². Adapted from H. Kasai and A. Suzuki [3]

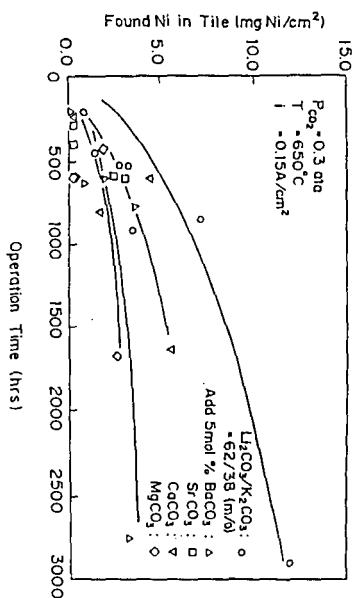


Fig. 2. Nickel found in the electrolyte tiles of terminated cells of Toshiba Corp. [4]

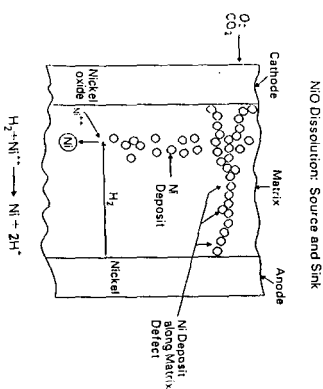


Fig. 3. Schematic representation of a cross-section through a MCFC cell, illustrating nickel oxide dissolution. From Williams and George [2]

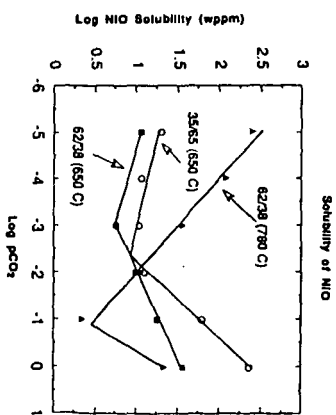


Fig. 4. Solubility of NiO in Li₂CO₃-K₂CO₃ mixtures, as function of pCO₂. From Lee and Shores [5]

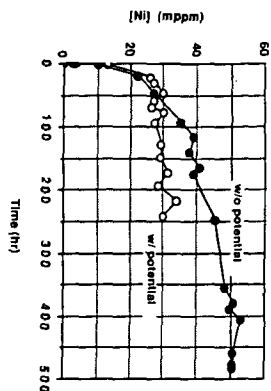


Fig. 5. Dissolution of NiO in bulk $\text{Li}_2\text{CO}_3\text{-K}_2\text{CO}_3$ eutectic as function of time. From Qu, et al. [6]

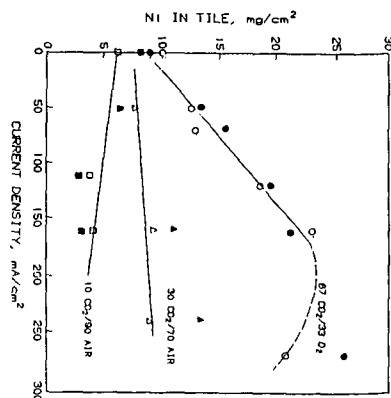


Fig. 6. Model predictions and experimental values of Ni deposited in the tile as function of CO_2 partial pressure and current density. Adapted from Ong [7], and Shores et al. [8]

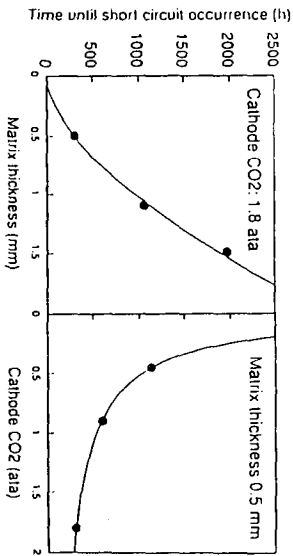


Fig. 7. Effect of matrix thickness and CO_2 partial pressure on time to start of internal shorting. From Mugikura, et al. [9]

MATHEMATICAL MODELING OF MCFC CELLS/STACKS AND NETWORKS

Dr. M. C. Williams¹, J. Wimer¹, F. Sudhoff¹
and Professor D. Archer²

¹US DOE, METC, Box 880, Morgantown, WV 26507

²Carnegie-Mellon University, Pittsburgh, PA

ABSTRACT

Molten carbonate fuel cell (MCFC) modeling has various uses and involves different degrees of sophistication. In this paper, the various, MCFC cell/stack and network and system models available in the public domain are discussed. Parametric and phenomenological fuel cell mathematical models are being used to simulate individual MCFC cell/stack performance. With the initial demonstration of full-area, full-height 250-kW to 2-MW MCFC power plants, the spatial configuration of the MCFC stacks into networks in the fuel cell power plant takes on new importance. MCFC network and power plant system flowsheet performance is being modeled using the ASPEN system model. ASPEN is a tear and iterate flowsheet simulator in the public domain. ASPEN is suitable for MCFC network simulation since it has strong systems and property database capabilities. With the emergence of larger MCFC power plant system demonstrations, system modeling of MCFC power plants is now essential. The DOE routinely uses MCFC models in making performance comparisons and in decision-making.

INTRODUCTION

The United States Department of Energy (DOE), Morgantown Energy Technology Center (METC) was one of the first organizations to recognize that MCFC systems are promising high-efficiency, power generation systems. Natural gas and gasification MCFC power plant systems with overall system efficiencies from fifty to sixty percent are forecast. Advanced, fully integrated gasification MCFC systems could have cycle efficiencies as high as 60 percent. The high MCFC efficiency makes it attractive for electric utility applications. On-site industrial and commercial applications where the waste heat can be utilized are also attractive. MCFC's are environmentally benign and can be sited in environmentally sensitive areas.

DOE is accelerating the private sector commercialization of multi-fuel, MCFC power plants. To accomplish this, METC is continuing support of power plant development, product development testing or demonstration and product improvement. With the emergence of larger MCFC power plant system demonstrations, system modeling of MCFC power plants is now essential. In addition, with the initial demonstration of full-area, full-height 250-kW to 2-MW MCFC power plants, the spatial configuration of the MCFC stacks in the fuel cell power plant takes on new importance.

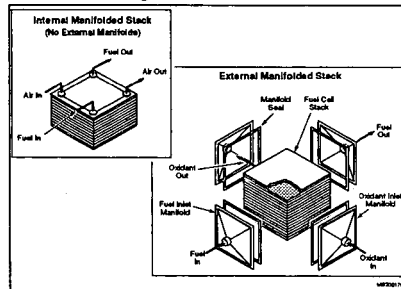
The developers of the MCFC have with the aid of the DOE been provided several models of MCFC performance available in the public domain. These models vary in their purpose, degree of complexity, and input requirements. Many have been modified to meet various developers ends. The DOE routinely uses them in making performance comparisons and in decision-making.

MCFC DESCRIPTION

MCFC stack designs incorporate either internal or external manifolding. Internal and external reforming are being considered for both manifolding concepts. All MCFC concepts employ flat cell components in the cell package (i.e., anode, matrix to hold carbonate, cathode, current collector, and separator plate). Operating conditions for MCFC's are projected to be in the ranges of 150 to 250 amperes per ft^2 at 0.60 to 0.80 volts with 50 to 85 percent fuel utilization (Williams and George, 1990).

Figure 1 illustrates the structure of an MCFC stack. Conductive, bipolar separator plates connect individual cells in a stack both structurally and electrically. Made of stainless steel, each bipolar separator plate physically separates the fuel gas stream of one cell from the oxidant gas stream of the adjacent cell. One side of each separator plate channels a fuel stream so that it flows over a porous anode, while the flip side channels an oxidant stream over a porous cathode. Each bipolar separator plate also collects current, connecting adjacent cells of a stack electrically in series. From the anode, electrons are conducted through the bipolar separator plate and into the cathode of the adjacent cell. There, they react with the oxidant gas stream and carbonate ions are formed. The carbonate ions diffuse through the electrolyte and into the anode, where they react with the fuel gas stream, releasing electrons into the anode. Electrons are conducted in this manner through all the cells, establishing direct current (DC) through the stack. An external circuit connects a load between the two endplates of the stack, completing the circuit.

In conventional fuel cell systems, multiple stacks have been arranged in parallel with regard to the flow of reactant streams. As illustrated in Figure 2, the initial oxidant and fuel feeds are divided into equal streams which flow in parallel through the fuel cell stacks.



Networking is ducting reactant streams such that they are fed and recycled through fuel cell stacks in series. Figure 2 also illustrates how the reactant streams in a fuel cell network flow in series from stack to stack.

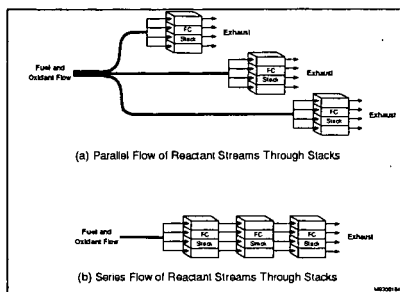
MCFC CELL/STACK MODELING

Lumped Parameter Modeling

Parametric-type models require the least user input information, and are used by some MCFC developers in the US and abroad. One such model is USRMC0 which can be used by itself or as an ASPEN (Advanced System for Process Engineering) user model. It was developed by Gilbert Commonwealth for modeling externally reforming MCFCs. USRMC0 is a lumped parameter and also a statistical, least squares or perturbation model, i.e., it adjusts a "reference" voltage based on deviations in the operating conditions from a set of arbitrary "reference" operating conditions. A separate voltage adjustment is made for deviations in each of the following variables: current density, temperature, pressure, fuel utilization, fuel composition, oxidant utilization, oxidant composition, cell lifetime, production year, and the presence of internal reforming. The user also may specify an additional arbitrary voltage adjustment. The estimated cell voltage is equal to the reference voltage plus the calculated voltage adjustments. After USRMC0 determines the cell voltage, it computes the cell power and heat loss.

Given the feed streams, several fuel cell production parameters (production year, number of stacks, number of cells per stack), and the operating conditions (temperature, pressure, fuel utilization, current density or area, and cell lifetime), the model computes the outlet compositions, cell voltage, power output, heat loss, and either the cell area or current density (whichever is not input).

Stauffer and coworkers (1991) give a discussion of the voltage adjustment correlations and their sources. Briefly, the correlations are simple, piecewise continuous splines that were fit to MCFC operating data culled from the literature. All of the correlations have the following properties: (1) the voltage correction is zero when the operating variable equals the reference state, (2) the greater the deviation of the operating condition from the reference state, the greater is the magnitude of the voltage correction, (3) the greater the deviation from the reference condition, the less accurate is the calculated voltage correction, and (4) the correlations are piecewise continuous but



their derivatives may not be (specifically, the correlations for current density, temperature, pressure, and production year have discontinuous derivatives).

Unfortunately, Stauffer and coworkers (1991) do not give either a comparison of the correlations with the literature data or an estimate of the accuracy of the predictions.

The model assumptions for USRMC0 are as follows: (1) flow through the fuel cell is cocurrent, (2) the anode and cathode are isothermal (although not necessarily at the same temperature), (3) the water gas shift reaction is in equilibrium at the anode outlet, (4) no reforming reactions occur within the fuel cell, (5) transport processes are fast in comparison to the rate of the fuel cell electrochemical reactions, (6) the "fuel" for which the fuel utilization is based consists of H_2 and CO, and (7) no solids are present in the inlet and outlet streams.

The USRMC1 model, which has been recently developed by DOE/METC, is an extension of USRMC0 (White, 1993). USRMC1 is an internally reforming model. This model is being used to compare the performance of various MCFC developers (Ashbaugh 1993).

Phenomenological Modeling

One common and popular phenomenological MCFC model in the public domain is the ICM4X model, referred to as the "PSI model" MCFC model. Unlike the Gilbert-Commonwealth model which is based on macroscopic performance equations, it is a distributed parameter model which attempts to model in detail the microscopic transport processes within the fuel cell (Wilemski and coworkers, 1979, Pigeaud, 1992). The PSI model requires more input and characterization of the MCFC than the Gilbert-Commonwealth model.

Key physical and chemical phenomena modeled include mass transport, ohmic losses, electrode kinetics, fuel and oxidant utilization, gas phase convective heat transfer and inplane conduction through cell hardware. Numerical solution schemes have been developed to calculate overpotential versus current density curves for electrodes, current-voltage performance curves, and current and temperature distributions. The solution involves solving a set of heat and mass balance equations.

DOE/METC (Gardener 1993) has recently compared the performance data of the major MCFC manufacturer's including Ansaldo Ricerche, Energy Research Corp., Hitachi Corp., International Fuel Cells Corp., Ishikawajima-Harima Heavy Industries Co., Kansai Electric Corp., MC-Power Corp. and Mitsubishi Electric Corp.

When comparing the performance data, it was necessary to normalize the data. Ideally, when the engineering performance comparison is made, all fuel cells should be operating at the same

constant fuel and oxidant utilizations on the same anode fuel and cathode oxidant. The fuel cells should also be operating at the same pressure. During a performance comparison test when the fuel cells are operating in the manner just prescribed, the current (load) is varied and the change in voltage is measured. As the current is increased, the voltage decreases and the fuel cell oxidant flows must increase to keep utilizations constant. As the current is increased from zero, the power output (the product of current and voltage) goes through a maximum, whereas the fuel cell efficiency decreases with increasing voltage. There are three engineering performance test curves which resulted from the DOE's performance test: 1) the plot of current density versus voltage, 2) the plot of current density versus power density, and 3) the plot of current density or voltage versus fuel cell efficiency.

MCFC NETWORK AND POWER SYSTEMS MODELING

With the initial demonstration of full-area, full-height 250-kW to 2-MW molten carbonate fuel cell (MCFC) power plants, the spatial configuration of the MCFC stacks into networks in the fuel cell power plant takes on new importance. METC has recently completed computer simulations were done to evaluate the performance of various internal reforming (IRMCFC) networks and to compare conventional IRMCFC power systems to networked ones (Wimer et. al 1993). The simulated performance of MCFC networks was found to be superior to the performance of unnetworked cells/stacks.

These important simulations were accomplished with the public version of ASPEN. ASPEN is an extremely powerful and complex tool. ASPEN is an iterative, flowsheet solver which tears recycles streams and iterates until convergence. ASPEN is a state-of-the-art process simulator and economic evaluation package which was designed for use in engineering fossil energy conversion processes. ASPEN can represent multiphase streams, including solids, and handle complex substances such as coal. The system can perform steady-state material and energy balances, determine equipment size and cost, and carry out preliminary economic evaluations. It is supported by a comprehensive physical property system for computation of major properties such as enthalpy, entropy, free energy, molar volume, equilibrium ratio, fugacity coefficient, viscosity, thermal conductivity, diffusion coefficient, and thermal conductivity for specified phase conditions -- vapor, liquid, or solid. The properties may be computed for pure components, mixtures, or components in a mixture, as appropriate. The ASPEN input language is oriented towards process engineers.

The DOE ASPEN IRMCFC stack model gives the user great freedom in defining the process he wishes to simulate. However, some details of the internal operation of the stack are not as flexible as others. For instance, the internal flow geometry of the stack is always assumed to be co-current. In addition, the internal voltage losses, ohmic, activation and concentration polarizations,

are not individually calculated by ASPEN. Instead, the user is required to specify the total voltage polarization at the stack outlet.

While a modest MCFC data input is required for the use of ASPEN, the system information input required can be extensive. Training in the use of ASPEN is required. ASPEN must have the composition and flowrate of the IRMCFC stack's inlet fuel and oxidant streams as well as a sufficient definition of their thermodynamic state (e.g. temperature and pressure). This information can be directly defined by the user, or ASPEN can calculate it from upstream process data.

Once the inlet reactant streams are known, the IRMCFC stack must be described. The number of cells in the stack must be given. Either the stack current or single-pass fuel utilization must be defined. The total outlet voltage polarization must be provided. The ASPEN model assumes that there is sufficient heat transfer between the fuel and oxidant streams such that they exit the stack at a common outlet temperature. Specification of this outlet temperature is optional. If left unspecified, ASPEN assumes that the stack is adiabatic. If the outlet temperature is provided, ASPEN equilibrates the exhaust gases at this temperature and calculates the corresponding heat duty.

The stack power output is computed by ASPEN as the product of stack current and stack voltage. Finally, by subtracting the stack power output from the total enthalpy change in the reactant streams, ASPEN calculates the heat duty of the stack (Shah 1988).

For a given total outlet voltage polarization, the performance predicted by the ASPEN IRMCFC model is generally conservative. The outlet Nernst potential which is calculated is the minimum possible for a given fuel utilization. Since the model assumes a co-current internal flow geometry, the conditions at the outlet of the stack generate the smallest local Nernst potential of anywhere within the stack. For a given fuel utilization, the Nernst potential which ASPEN calculates is the smallest possible for any internal flow geometry.

REFERENCES

1. Ashbaugh, M., "A Comprehensive MCFC Performance Comparison," DOE Memorandum, June, 1993.
2. Gardner, T., "A Comprehensive MCFC Performance Comparison," DOE Memorandum, April 2, 1993.
3. Pigaud, A., "Effects of Coal-Derived Trace Species on Performance of Molten Carbonate Fuel Cells", Final Report, Contract No. DE-AC21-88MC25009, May 1992.
4. Stauffer, D.B., White, J.S. and J.H. Hirschenhofer, "An ASPEN/SP MCFC Performance USER Block", Final Report, Contract No. DE-AC21-89-MC25177, July 1991.
5. Shah, V., "ASPEN Models for Solid Oxide Fuel Cell, Molten Carbonate Fuel Cell & Phosphoric Acid Fuel Cell", Final Report, Contract No. DE-AC21-85MC21353, June 1988.
6. White, C., "An ASPEN User Model for an Internal Reforming Molten Carbonate Fuel Cell: Code Documentation," ECG Report to DOE, April 1993.
7. Willemaki, G., Wolf, W., Bloomfield, D., Pinaon, M.L., Pugh, E.R., and K.L. Wray, "Performance Model for Molten Carbonate Fuel Cells", Final Report, Contract No. DE-AC-03-79ET11322, August 1979.
8. Williams, M. C. and George, T. J., "The Developmental Status of Coal-Fueled Molten Carbonate Fuel Cell Power Plants," Proceeding 25th IECEC, 3, pp. 185-92 (1990).
9. Wimer, J., Williams, M. C., Azcoff, D. and Oster, J., "MCFC Networks: Principles, Analysis, and Performance," Proceeding 26th IECEC, Atlanta, 1993.

ADVANCED BATTERIES FOR ELECTRIC VEHICLE APPLICATIONS

by

D. R. Vissers, W. H. DeLuca, and G. L. Henriksen
Argonne National Laboratory
Electrochemical Technology Program
Chemical Technology Division
9700 South Cass Avenue
Argonne, IL 60439

Keywords: Electric Vehicles, Zero Emission Vehicles, Advanced Batteries

1.0 INTRODUCTION

In the late 1970s, the U.S. government launched major battery R&D projects to assist industry in the development and commercialization of electric vehicles (EVs). These efforts were initiated to relieve U.S. dependence on foreign oil, following the 1973 oil crisis. The Electric & Hybrid Vehicle Program was established under Public Law 94-413, entitled "Electric and Hybrid Vehicle Research, Development, and Demonstration Act of 1976." This program, residing within the Energy Research and Development Administration--the precursor to the U.S. Department of Energy (DOE)--was responsible for establishing and monitoring federally funded EV projects, including the EV battery R&D projects. Also, the Electric Power Research Institute (EPRI), through its Electric Transportation Program, helped support advanced battery R&D projects for EVs. However, funding for these projects was not sustained at a sufficient level through the 1980s to significantly advance any of the battery technologies being supported by DOE and/or EPRI.

In the early 1990s, concern over deteriorating air quality in many urban areas of the U.S. caused state legislatures to begin mandating the introduction of zero emission vehicles (ZEVs), ultra-low emission vehicles, and low emission vehicles. In 1990, California was the first state to enact such legislation for the Los Angeles Basin area of southern California. According to the current definition, battery-powered or flywheel-powered vehicles are the only types of vehicles that qualify as ZEVs. California requires automobile manufacturers to market ZEVs at the rate of 2% in 1998 and 10% in 2003. Several states along the East coast are enacting similar legislation. Maine, Maryland, New Jersey, and New York are in various stages of enacting legislation, while surrounding states are considering it.

In January 1991, Chrysler, Ford, and General Motors formed a partnership, named the U.S. Advanced Battery Consortium (USABC), to accelerate the development and commercialization of selected advanced-battery technologies. Both EPRI and DOE joined with the U.S. auto industry to make it a joint government/industry consortium later that same year. According to existing agreements, which run through 1995, DOE provides 50% of the funds and industry provides the other 50%. Total funding for these projects could reach \$260 million during this time frame.

Also, a number of international battery companies formed a consortium in 1992, the Advanced Lead-Acid Battery Consortium (ALABC), to promote the development of advanced lead-acid batteries for EV and hybrid vehicle (HV) applications. This was done in response to a decision by the USABC to fund R&D only on more-advanced battery technologies. The ALABC research efforts are directed at increasing cycle life, achieving rapid recharge capabilities, and increasing specific energy of lead-acid batteries. It is a 38-member 11-nation consortium.

Finally, in October 1992 former President Bush signed into law the Energy Policy Act of 1992, which includes many new initiatives relating to EVs. Included in these initiatives are:

- o Major multi-year (1993-8) R&D programs on batteries and EVs
- o A 10-year \$50 million EV demonstration program
- o A 5-year \$40 million infrastructure development program
- o A \$50 million program to assist states in developing and implementing incentives
- o A federal tax incentive program

2.0 REQUIREMENTS

The requirements for an EV battery can vary significantly, depending on the type of vehicle and its intended mission. When the USABC established criteria for advanced battery technologies, they necessarily avoided this issue and created two sets of generic goals: one for mid-term batteries and the other (more demanding) for long-term batteries. The USABC primary battery criteria for mid-term and long-term batteries are provided in Table 1.

Table 1. USABC Primary Battery Criteria for Mid-Term and Long-Term Batteries.

Parameter	Mid-Term Criteria	Long-Term Criteria
Specific Energy (Wh/kg)	100	200
Specific Power (W/kg)*	200	400
Energy Density (Wh/L)	150	300
Power Density (W/L)*	300	600
Cycle Life (cycles)	600	1000
Calendar Life (years)	5	10
Recharge Time (hours)	6	3-6
Selling Price (\$/kWh)	150	100

*30-second peak power @ 80% depth of discharge (DOD)

Additional criteria related to electrochemical efficiency, thermal efficiency, abuse tolerance, and freedom from maintenance were established by the USABC. Again these are generic criteria not tied to specific vehicles or vehicle missions.

It is possible to use published information on electric vehicles under development today to establish some vehicle-related requirements for EV batteries. These requirements are based on battery technologies available today or in the near term and would likely be altered by the availability of a more-advanced battery system. A few of these requirements are provided in Table 2.

As shown in Table 2, the power-to-energy ratio of the batteries for these two vehicle applications differ significantly. This is because the electric van acceleration is intended to be comparable to that of a diesel-powered van, while the acceleration of the passenger vehicle is intended to be comparable to that of a sports car. Another difference between the van and passenger vehicle applications is the importance placed on the space occupied by the battery. On a relative basis, more space is available in a van and, therefore, battery weight becomes the controlling parameter. However, in passenger vehicle applications, it is more difficult to allocate space for the battery, and battery volume becomes a more significant parameter.

Table 2. Vehicle Related Battery Requirements.

Parameter	Electric Van	High-Performance Passenger Car
Energy (kWh)	40	14
Power (kW)	60	85
Weight (kg)	650	410
Size (LxWxH, in cm)	191x79x25	205x20x33
Voltage (V)		
Maximum	260	415
Minimum	140	320
Max Current (A)	340	340
Power/Energy Ratio	1.5	6.1

3.0 TECHNOLOGIES

With the advent of requirements for zero emission vehicles in California, the U.S. government and the U.S. automobile manufacturers have launched a concerted effort to develop advanced batteries for electric vehicles. In this overview of the battery technologies, we will review the major existing or near-term systems, as well as the advanced systems being developed for EV applications. It is important to note that this overview does not cover all of the advanced batteries being developed in the world today.

3.1 Near-Term Batteries

By definition, near-term batteries are currently being manufactured commercially and are available for use in electric vehicles in large volumes. These batteries include the nickel/cadmium and lead-acid batteries. Both battery types have their advantages and disadvantages.

For example, the lead-acid battery dominates the SLI market in the United States for automobiles and trucks. It is quite inexpensive and has excellent power characteristics. However, as a propulsion device for an electric vehicle, specific energy is quite low, limiting the vehicle range to about 60 to 100 miles. Nevertheless, the first generation of commercial electric vehicles will probably utilize these batteries because of their widespread availability and low cost.

The nickel/cadmium battery also possesses excellent power but has significantly better specific energy and longer cycle life than the lead-acid system. However, it is very expensive and, because of its use of cadmium, raises environmental concerns related to disposal of spent batteries. This system, however, may well be used in a limited number of first generation EVs because of its performance and life characteristics.

3.2 Advanced Batteries

The advanced batteries are divided into mid-term (available in 5 years) and long-term (available in 5 to 10 years) systems. The mid-term batteries include sodium/sulfur, sodium/nickel chloride, nickel/metal hydride, zinc/air,

zinc/bromine, and nickel/iron systems. The long-term batteries principally include the lithium-polymer and the lithium/iron disulfide systems; the latter could also be available in the mid term.

3.2.1 Mid-Term Batteries

Of the mid-term batteries, the sodium/sulfur and sodium/nickel chloride systems offer the highest specific energies. Sodium/sulfur offers higher power, while the sodium/nickel chloride offers longer life. On the other hand, the nickel/metal hydride system offers the best power and may approach the sodium-based batteries in specific energy. The zinc/air and zinc/bromine batteries have energies similar to those of the sodium-based batteries but are limited in power. Finally, the nickel/iron system has specific energies comparable to those of nickel/cadmium, but lacks the power of the nickel/cadmium system and tends to exhibit poor columbic efficiency because of the excessive amount of hydrogen that is generated on charge.

3.2.2 Long-Term Batteries

The long-term batteries are expected to have very high specific energy (200 Wh/kg) and specific power (400 W/kg) with calendar lives of 10 years. The lithium/iron disulfide system appears to be further advanced than the lithium-polymer system at present, but because of the proprietary nature of the development efforts, on the latter, it is difficult to assess its status and exact degree of development. Both of these systems appear very promising, and significant efforts on their development are being carried out in the United States.

It is important to note that the lithium-polymer system operates at about 60-120°C, while the lithium/iron disulfide system operates at slightly over 400°C. Attaining the 400 W/kg specific power will be a technical challenge for any battery system, more so for the low temperature systems.

4.0 PERFORMANCE AND LIFE TESTING AT ANL

Advanced-battery technology evaluations are performed under simulated electric-vehicle operating conditions at ANL's Analysis & Diagnostic Laboratory (ADL). In this segment of the paper we briefly review the performance and cycle-life test results obtained at ANL on several near-term and mid-term battery technologies. The tests were conducted over a period of several years--mainly during the period of 1990 thru 1992--for DOE's Electric and Hybrid Propulsion Division and EPRI's Electric Transportation Program. The tests were conducted on a wide range of hardware, covering single cells to multi-cell modules, encompassing six types of battery technologies--Na/S, Zn/Br₂, Ni/MH, Ni/Cd, Ni/Fe, and Pb-Acid.

Table 3 lists the general specifications and best performance demonstrated by each EV battery technology. Plots of specific energy and specific peak power for each technology are given in Figs. 1 and 2, respectively. The specific energies were measured using constant power discharges to 100% depth of discharge (DOD). The specific peak powers were derived from driving profile discharge data and are plotted as a function of DOD, based on available energy for the average power discharge rate.

4.1 Sodium/Sulfur System

An 8-V Na/S module from Chloride Silent Power Ltd. (CSPL) was under test from June 1990 to March 1992. The module contained 120 cells (10-Ah each) configured into 30 parallel-connected strings of four series-connected cells. This 300-Ah module was of the same design and assembly as those (24 series-connected modules) in the battery system developed for the Ford ETX-II vehicle (a light-duty van based on the Ford Aerostar). Life testing with Simplified Federal Urban Driving Schedule (SFUDS) discharges to a DOD of 100% was started in October 1990, after completion of the performance characterization tests (~120 cycles accrued). Test results indicated that the specific energy of this module is similar to that of the ASEA Brown Boveri (ABB) battery previously tested at ANL (see Table 3). However, the CSPL module had a higher internal resistance and, therefore, could not

achieve as high a peak power. End-of-life (<80% of initial SFUDS discharge energy) occurred at cycle 795, but testing was continued to acquire additional statistics for cell failure analyses. Testing was halted in March 1992 (21 months and 973 cycles at operating temperature) when the SFUDS discharge energy decreased to <75% of its initial level. There was a significant drop in module capacity between 450 and 550 cycles of operation, which reflected the loss of four 4-cell strings (~40-Ah loss). Module resistance increased by ~20%, which also indicated the loss of four strings in the 30-string battery. Owing to the increase in module resistance with life, the peak power declined from an initial 94 W/kg to only 68 W/kg at the end of testing (50% DOD). After 973 cycles, the module retained ~79% of its initial 292-Ah capacity (3-h rate) and ~73% of its initial 2084-Wh SFUDS discharge energy (100% DOD). The Na/S technology approaches the USABC mid-term goals.

Table 3. Performance Summary of EV Battery Systems Evaluated in the ADL Between January 1991 and December 1992

Battery Description			Initial Module		Specific Energy, ^a Wh/kg	Energy Density, ^a Wh/L	Peak Power, ^b W/kg	Efficiency ^c		Life, ^d cycles	Van Range, ^e mi (km)
Technology	Manufacturer	Model	Weight, kg	Capacity, ^f Ah				Coulombic, %	Energy, %		
Sodium/Sulfur	ABB CSPL	B-11 ^g BP-MK3	253 29.2	238 292	81 79 ^h	83 123 ⁱ	152 90 ^j	100 100	91 88	592 795	154 (246) 150 (240)
Zinc/Bromine	SEA	ZBB-5/48	81	126	79	56	40	93	75	334	93 (149)
Nickel/Metal Hydride	Oxonica	H-Cell	0.628	28.0	55	152	175	90	80	505 ^k	97 (155)
Nickel/Cadmium	SAFT	STM5-200	24.5	214	55	104	175	90	78	1018 ^k	102 (163)
Nickel/Iron	Eagle-Picher	NIF200	25	203	51	118	99	74	58	918 ^k	87 (139)
Lead-Acid	Sonnenschein CEVS	6V160	31.5	184	36	92	91	94	84	370 ^h	51 (82)
		3ET205	32.8	185	33	78	68	87	68	149	47 (75)

^aDetermined for 3-h rate discharges at constant current.
^bDetermined from driving profile discharge data at 80% depth of discharge (DOD).
^cDetermined with discharges to 100% DOD under the Simplified Federal Urban Driving Schedule (SFUDS), unless otherwise indicated.
^dDetermined for the IDSEP (improved dual-shaft electric propulsion) Van with a 695 kg battery on an SFUDS driving schedule.
^eTested in 1991; included for comparison.
^fBased on manufacturer projections of future battery weight and case volume.
^gTested with 80% DOD discharges.
^hTested with discharges under simulated driving profile, J227aC.

4.2 Zinc/Bromine System

A 5-kWh, 48-V Zn/Br module (ZBB-5/48) from the Studiengesellschaft für Energiespeicher und Antriebssysteme (SEA) (Research Group for Energy Storage and Propulsion Systems, Austria) underwent EV performance and life testing from November 1989 to June 1991. Performance characterization tests showed that the SEA battery has good specific energy (~79 Wh/kg at 3-h rate) but low power capability (~53 W/kg at 50% DOD). The low power is due to a high internal battery resistance. The battery also exhibited a high self-discharge loss (~20% loss in 24 h) when its electrolyte pumping motors remain energized. This loss is significantly reduced when pump operation is halted during extended open-circuit times. Life testing with SFUDS discharges to 100% DOD was started in March 1990 after performance testing (~130 cycles accrued). Because of the high module resistance, a peak discharge current limit (150 A) had to be imposed with SFUDS discharges to avoid reaching the discharge cut-off voltage (DCOV) on the first 79 W/kg power peak. With a 150 A current limit, a maximum power of ~67 W/kg was obtained at the start of the discharge, and 50 W/kg was attained at the 27-V DCOV. The module reached end-of-life (>20% loss of initial capacity) after 334 cycles. The power characteristics of this technology need to be significantly enhanced if it is to be used for EV applications.

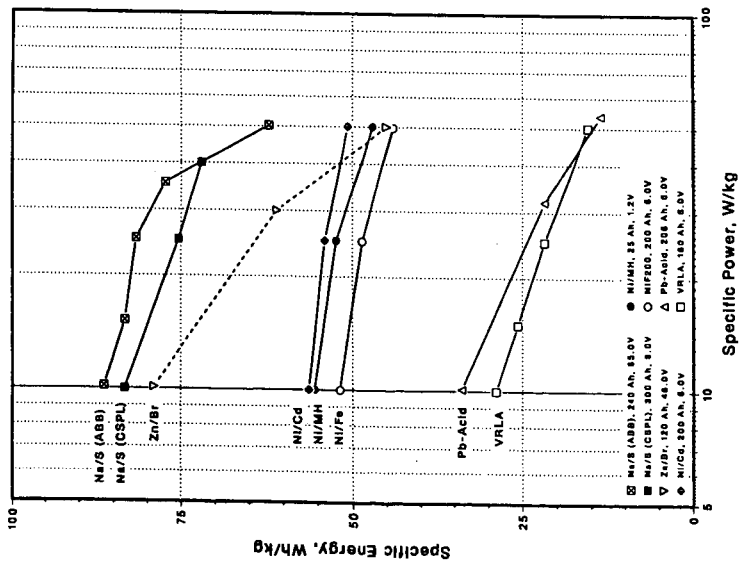


Fig. 1. Effect of discharge specific power on available energy of eight advanced battery systems.

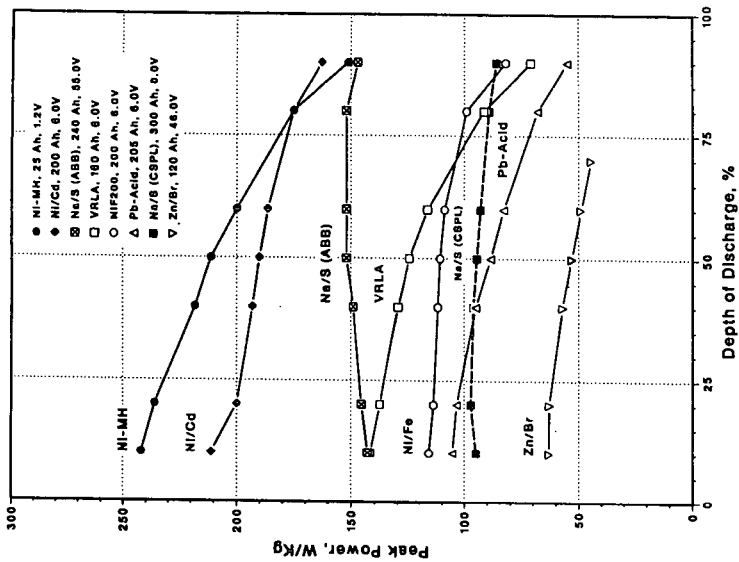


Fig. 2. Derived peak power vs. DOD of eight advanced battery systems from driving profile discharge (J227d/IETV1) data.

4.3 Nickel/Metal Hydride (Ni/MH) System

Performance and life tests were conducted on two Ni/MH cells (25-Ah rating) manufactured by Ovonic Battery Co. (Troy, MI) to determine the suitability of this technology for EV applications. The two cells were delivered to ANL in June 1991. Performance characterization tests were completed, and life evaluation (SFUDS discharges to 80% DOD) started in November 1991. The peak power of the H-cells is the highest measured at the ADL to date (175 W/kg at 80% DOD and ~200 W/kg at 50% DOD). A high peak power provides full capacity and maximal vehicle range for all driving profile discharges. One H-cell was removed from life test after 380 cycles due to a sudden decline in capacity (to <70% of its initial 25-Ah capacity) caused by electrolyte loss. Water (13.6 g) was added to this valve-regulated cell, and full capacity (26.5 Ah) was achieved on a subsequent discharge. Thereafter, the capacity declined at a rate of ~0.5 Ah/cycle. Testing was halted when the capacity declined to 13.8 Ah on cycle 399. Cell weight was reduced again (6.3 g). The problem was later found to be caused by a faulty pressure release vent.

The second H-cell was removed from life test after 533 cycles due to capacity and power loss. End-of-life (EOL) with SFUDS discharges to 80% DOD occurred on cycle 505. The weight of this cell did not change significantly with life. The charge return was increased from 120% to 150% after EOL, but no improvement in cell capacity resulted. The cell retained ~78% of its initial 28-Ah capacity (3-h rate) when testing was halted. Both H-cells were returned to Ovonic for further analyses. This battery technology has excellent potential to meet the USABC mid-term performance goals.

4.4 Nickel/Cadmium System

Life tests were conducted on a 6-V Ni/Cd module (190-Ah rating) manufactured by SAFT (Industrial Storage Battery Division), France, from April 1990 to August 1992. The module was received from Idaho National Engineering Laboratory, where it had completed 35 performance characterization cycles. Life testing was started at the ADL in June 1990 after 78 cycles of performance testing. Life evaluation was conducted with discharges to 100% DOD using the J227aC driving profile for a Chrysler TEVan. The module had completed 1018 cycles and still retained ~99% of its initial capacity (3-h rate) when it was voluntarily removed from test. At that time, the TEVan discharge energy had only declined to ~96% of its initial value. Variations in module resistance, IR-free voltage, and peak power vs. DOD during the life evaluation were examined. Analyses showed that module resistance had increased by ~23%, and IR-free voltage had remained constant to within 1.0%. As a result of the increased module resistance, the peak power was decreased from 190 to 154 W/kg at 50% DOD (~19% decrease) between cycles 46 and 1016. This module was sent to EPRI for other EV evaluations. The Ni/Cd battery technology has performance very comparable to the Ni/MH battery technology.

4.5 Advanced Nickel/Iron System

Life tests were conducted on four advanced Ni/Fe modules (NIF200) from Eagle-Picher Industries, Inc. The NIF200 design provides a capacity of 200 Ah in the same module package as the 170-Ah module developed for the dual-shaft electric propulsion (DSEP) vehicle developed by Eaton Corp. The longest operating module completed 918 cycles with discharges to 80% DOD (J227aC driving profile for G-Van) before reaching EOL in April 1992. Another module was cycled using an ANL-recommended charge regime from November 1991 to October 1992. The module completed 394 cycles (to 100% DOD using J227aC for a Chrysler TEVan) before reaching EOL. Module life was less than expected based on that exhibited by early NIF200 modules. The two remaining NIF200 modules were voluntarily removed from testing to prepare for future deliverables. This technology with its excellent cycle life and moderate power could be used as a near-term battery for EVs.

4.6 Recombinant Lead-Acid Systems

Tests were started in December 1989 for EPRI on two 6-V, valve-regulated lead-acid (VRLA) modules with a gelled electrolyte manufactured by Sonnenschein Battery Co. (Germany). The maintenance-free cells were equipped with pressure-relief valves for gas venting and used an antimony-free alloy. Both modules completed performance characterization, and one underwent life testing with J227aC/G-Van discharges to 100% DOD. After 370 cycles, the energy obtained on simulated driving profile discharges had declined to 80% of its initial level. New modules were delivered from Sonnenschein, and one was placed on life test using G-Van discharges. The module was operated to 100% DOD for 122 cycles and then changed to 80% DOD cycling. This module completed 448 cycles before reaching end-of-life (100% DOD condition reached before the 80% DOD energy obtained). At that time, the 3-h rate capacity had only declined by $\approx 9\%$. This lead-acid battery technology appears very promising and will probably be used in near-term EVs.

4.7 Tubular Lead-Acid System

Two advanced, three-cell, lead-acid modules with tubular positive electrodes (3ET205) made by Chloride EV Systems Ltd. (CEVS), England, were acquired and tested in January 1991. This test measured the 3ET205 cycle life with SFUDS discharges (100% DOD) for comparison with that achieved in an EPRI-sponsored test using J227aC/G-Van discharges to 100% DOD. Both of the new modules underwent an abbreviated performance characterization, and one was selected for life testing with SFUDS discharges. After 149 cycles, this module reached end-of-life ($<80\%$ of initial energy). In the EPRI test (1990), the 3ET205 module completed 715 cycles before reaching end-of-life. Post-test analyses revealed that both modules failed due to deterioration of the negative electrodes, caused by high levels of antimony and by poor adhesion between the active materials and the grids. The antimony was generated by corrosion of the positive grids and plated onto the negative electrodes during operation. Charging efficiency and effective capacity of the electrodes were consequently reduced. The cells in the module using SFUDS discharges had a greater divergence in post-test findings than those observed in the EPRI module. Hence, cell mismatch may have impaired the evaluation of the SFUDS test. This particular lead-acid battery exhibited limited cycle life.

5.0 CONCLUSIONS

It will be very difficult for any one battery system to meet the propulsion requirements of the different vehicle configurations. For example, while van applications allow significant space for battery systems and require only a power-to-energy ratio of 1 or 2, batteries used in high-performance passenger cars or hybrid vehicles will require power-to-energy ratios of 6 or 7 and will allow only a minimal space for the battery system. Thus, a battery such as a lead-acid system may be very suitable for a van application but might be entirely inappropriate for a commuter or hybrid vehicle, where much higher power and energy densities are required. Certainly, some of the advanced batteries, such as the lithium/iron disulfide system, when they are developed, could be configured for different vehicle configurations. That is, an advanced battery with a power-to-energy ratio of 6 or 7 might be designed for a hybrid vehicle, while this same battery might be redesigned for a van with a power-to-energy ratio of 2.

The development of advanced batteries for electric vehicles is going to require many years and many millions of dollars before they are ready for commercial EV applications. While the DOE/USABC initiative will certainly move battery technologies forward from their present levels, it is highly unlikely that this initiative will be successful in developing all the technologies to the point where they meet most of the battery requirements. Certainly, some of the technologies, such as lead-acid and nickel/cadmium, are near commercialization, but others, such as lithium-polymer and lithium/iron disulfide, require significantly more development before they will be commercial. Others, such as nickel/metal hydride, sodium/nickel chloride, and sodium/sulfur are at an intermediate stage of development.

Table 4 provides a comparison of relative characteristics for near-term, mid-term, and long-term battery technologies. The performance and life data for Pb-Acid, Ni/Cd, Ni/Fe, Ni/MH, Zn/Br₂, and Na/S batteries are based on ANL's test data. Those for Na/NiCl₂, Zn/Air, Li/FeS₂, and Li-polymer are based on developers' data and/or ANL projections scaled from cell data. Relative costs are ANL judgements based on our knowledge of materials' and processing costs for these technologies. The information presented in Table 4 clearly illustrates a trend toward higher performance in moving from near-term to long-term batteries. However, there is a corresponding increase in R&D time and cost, along with a higher degree of uncertainty regarding the ultimate commercialization of these technologies for EV applications. Also, it appears that no battery technology is the ideal battery for every EV application. Some technologies combine high specific energy with low-to-moderate cost, but have peak power limitations. Others offer high specific energy and peak power, but appear to be more expensive. Therefore, a number of these technologies are likely to be used commercially as EV batteries to satisfy different EV vehicle market segments. Certainly, if the lithium/iron disulfide or the lithium-polymer batteries can achieve 200 Wh/kg and 400 W/kg, as specified by the USABC, an electric vehicle with an extended operating range >200 miles between recharges could be achievable.

Finally, it is important to understand that the development of viable electric vehicles will require many years of development and involve many iterations, both of the battery and of the vehicle itself. When one considers that this nation spends about \$50 billion each year on imported oil, the bulk of which is utilized for transportation and the use of which significantly affects our urban environments, it is quite apparent that EVs, when developed, could have a tremendous beneficial effect on our environment and economy.

Table 4. Comparative Characteristics of Candidate Electric Vehicle Battery Systems

Battery System	Specific Energy (Wh/kg)	Peak Power ^a (W/kg)	Cycle Life (cycles)	Relative Cost	State of Development
Lead-Acid	25-40	70-90	400-700	Low/Moderate	Commercial
Nickel/Cadmium	50-60	175	>1000	High	Commercial
Nickel/Iron	50-60	100	>1000	Moderate/High	Prototype ^b
Nickel/Metal Hydride	50-65	170-300	~500	Moderate/High	Module
Zinc/Bromine	80	40	~300	Low/Moderate	Prototype ^b
Sodium/Sulfur	75-80	100-150	800-900	Moderate	Prototype ^b
Sodium/Nickel Chloride	80-100	50-75	>1000	Moderate/High	Prototype ^b
Zinc/Air	75-100	~50	100-200	Low/Moderate	Prototype ^b
Lithium/Iron Sulfide	130-170	200-500	TBD	Moderate	Stack
Lithium-Polymer	100-200	100-300	TBD	Moderate/High	Cell

^aPeak power at 80% DOD for 30 seconds.

^bFull-scale prototype EV batteries have been tested in vehicles.

ACKNOWLEDGMENT

This work was supported by the Department of Energy, Office of Transportation Systems, Electric and Hybrid Propulsion Division under Contract W-31-109-Eng-38, and the Electric Power Research Institute.

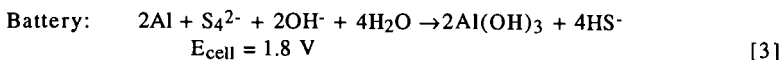
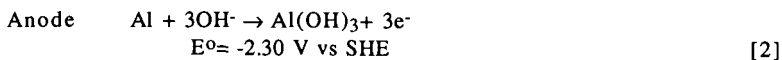
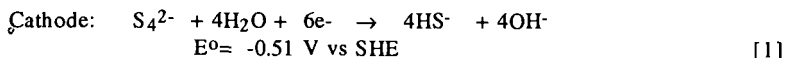
THE HIGH STORAGE CAPACITY OF SULFUR AT LOW TEMPERATURE NOVEL SOLID SULFUR CATHODES FOR AQUEOUS BATTERIES

Dharmasena Peramunage and Stuart Licht
Department of Chemistry
Clark University
Worcester, MA 01610

Keywords: Batteries, Fuel Cells, Aluminum/Sulfur

The light weight of sulfur makes metal/molten sulfur batteries attractive for electrochemical energy storage. However, material constraints associated with the requisite high temperatures, have slowed the development of a variety of metal/molten sulfur batteries (1). In a previous study we introduced an alternative high faradaic capacity aqueous sulfur redox cell (2). That study described conductive solutions which by mass could accommodate more sulfur than water, and demonstrated faradaic storage capacities comparable to those in molten sulfur batteries. In a recently letter we presented the utilization of this ambient temperature polysulfide redox reaction with an aluminum anode to introduce a class of aluminum/polysulfide batteries (3).

The battery was expressed by aluminum oxidation and polysulfide reduction for an overall battery discharge consisting of:



In accordance with Eq. [3], this aluminum/polysulfide battery has a theoretical charge capacity of 505, 595, or 724 Ahr/kg calculated respectively using either potassium, sodium or lithium electrolytes.

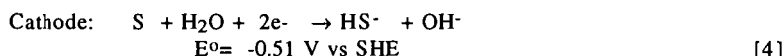
Eq. [1] represents a simplified description of sulfur reduction. Sulfur dissolved in aqueous sulfide solutions gives rise to a variety of polysulfide species, dominated at moderate alkaline pH by the tetrasulfide species, S_4^{2-} (4). CoS is an effective material to electrocatalyze oxidation

and reduction of polysulfide (5). Cathodic polarization losses at thin film CoS electrodes decrease from $-4 \text{ mV cm}^2 \text{ mA}^{-1}$ to $2 \text{ mV cm}^2 \text{ mA}^{-1}$ as temperature increases from 20° to 65°C . Zero valent sulfur added to sulfide solutions may be reduced to the divalent state at faradaic efficiencies approaching 100 percent (2). The electrochemistry of polysulfide solutions reflects the complex speciation in these solutions, and is affected by solution pH, activity and the ratio of dissolved sulfur per sulfide. In concentrated solutions, with the ratio of dissolved sulfur per sulfide increasing from 1 to 3, the polysulfide potentials shifts 150 mV cathodically, a favorable situation for coupling with an Al anode.

Effective aluminum anode utilization requires that the rate of electrochemical oxidation must be high compared to the competing chemical loss reaction. Polarization losses for aluminum oxidation have generally not been investigated in highly concentrated (greater than 10 molal) alkaline solutions useful to maximize energy density of the aluminum/sulfur battery. Polarization losses for aluminum oxidation in a 18 m KOH solution decrease from 6 to $0.4 \text{ mV cm}^2 \text{ mA}^{-1}$ as temperature is increased from 20° to 85°C . Measured polarization is similar in either concentrated sodium or potassium hydroxide electrolytes, and also for aluminum anodes comprised of either 99.999% Al or an alloy containing over 99% Al and added Mg, Sn and Ga.

Initial tests on the aluminum/polysulfide cells consist of non-flow batteries. Anolyte limited cells were discharged to determine the anodic efficiency in highly concentrated alkaline electrolytes. Additives such as metal oxide salts effect cell performance. 10mm Ga_2O_3 added to 18 m KOH anolyte enhances cell voltage, whereas added $\text{In}(\text{OH})_3$ substantially increases anodic capacity. Anodic utilization efficiency is further increased to over 80% by optimization of anolyte volume (3). Al/polysulfide batteries were demonstrated with an energy density of 170 Whr/kg based on materials excluding water (modeling a "water activated" cell) and 110 Whr/kg based on total materials (3). "D" volume (0.05 liter) cells provided a 10.1 Whr energy capacity with an 86% conversion efficiency based on KOH, a 78% conversion efficiency based on K_2S_4 , and an 68% conversion efficiency based on consumed Al. In Table I, the aluminum/polysulfide battery is compared to conventional Zn/carbon and alkaline batteries under standard moderately high current densities. Under these test conditions, the time of discharge advantage of the new cell is evident. Studies of solution and aluminum modification continue to further increase the energy density of the aluminum/polysulfide battery.

In accordance with Eq. 1, at 25°C, the solubility of K₂S₄ is consistent with a maximum charge capacity of 500 Ah/kg solution. Here we investigate an alternative, higher capacity cathode. This new cathode could be capable of direct reduction of elemental sulfur at room temperature. The new maximum storage capacity is substantially increased, and is given by the limit as all solid sulfur is reduced:



$$\text{storage} = \frac{1 \text{ mole (S+H}_2\text{O)}}{(0.032+0.018)\text{kg}} \cdot \frac{2 \text{ faraday}}{\text{mole}} \cdot \frac{96500\text{C}}{\text{faraday}} \cdot \frac{\text{Amp hour}}{3600\text{C}} = 1070 \text{ Ah/kg}$$

This theoretical storage capacity of the solid sulfur cathode is several fold higher than the theoretical storage capacity of conventional aqueous cathodes including PbO₂, NiOOH, MnO₂, HgO, and AgO (1).

The new cathode features solid sulfur in contact with aqueous polysulfide solution. This solid sulfur will not dissolve in a polysulfide solution saturated in sulfur. Initiation of reductive discharge of the cell will generate shorter length polysulfide species:

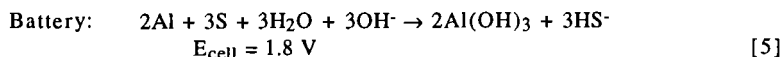


which as represented in Figure 1B then permits dissolution and continued reduction of available solution and solid phase sulfur:



Discharge proceeds until all available zerovalent sulfur (both solid and dissolved) is reduced in accordance with Eq. 1. The solid sulfur maintains longer chain polysulfide species in solution. Longer chain polysulfide species positively shifts and maximizes cell voltage (2). This elemental (solid/solution phase) sulfur cathode has the theoretical advantage of higher storage capacity and higher cell voltage.

The solid sulfur cathode was incorporated into an aluminum cell analogous to the aluminum/polysulfide battery recently described (3). In accordance with Eq. 2 and Eq. 4, discharge of the aluminum/solid sulfur battery is expressed by:



Faradaic capacity of the Al/solid sulfur battery (based on potassium salts and all reactants) is 505 Ah/kg, and the theoretical specific energy is:

$$1.8 \text{ Volt} \times 505 \text{ Ah/kg} = 910 \text{ Wh/kg} \quad [6]$$

This 910 Wh/kg aluminum/sulfur battery theoretical specific energy is approximately 40% higher than the aluminum/polysulfide battery (8), and is 2 to 5 times that of conventional aqueous batteries. Utilization of lighter weight cations than K^+ may further improve the Al/S energy capacity.

REFERENCES

1. D. Linden, "Handbook of Batteries", McGraw-Hill, NY (1984).
2. S. Licht, *J. Electrochem. Soc.*, **134**, 2137 (1987).
3. S. Licht, D. Peramunage, *TJ. Electrochem. Soc.*, **140**, L4 (1993).
4. S. Licht, *Nature*, **330**, 148 (1987).
5. G. Hodes, J. Manassen, D. Cahen, *J. Electrochem. Soc.*, **127**, 544 (1980).

Table I. Comparison of Al/S and conventional aqueous electrochemical storage at 20°C. The aluminum/sulfur cells contain 0.018 L of 7.7 m K_2S_4 catholyte and 0.032 L of 18 m KOH, 10 mm $\text{In}(\text{OH})_3$ in a rectangular cell geometry described in the text.

load	<u>D size cells continuous discharge time to 0.65 volts</u>		
	<u>Zinc Carbon (1)</u>	<u>Alkaline (1)</u>	<u>New Aluminum/Sulfur</u>
0.5W	0.5 hours	3.0 hours	7.4 hours
1.0W	1.0 hour	6.5 hours	13 hours
2.3 W	3.5 hours	19 hours	28 hours

A NOVEL HIGH POWER AND ENERGY DENSITY
ENVIRONMENTALLY COMPATIBLE ALUMINUM/PERMANGANATE BATTERY

Stuart Licht and Dharmasena Peramunage
Department of Chemistry
Clark University
Worcester, MA 01610

Keywords: Batteries, Fuel Cells, Aluminum/Permanganate

The search for contemporary batteries with the requisite high power and energy densities for electric propulsion of vehicles has blurred the conventional distinctions of electrochemical storage systems, and no available system is considered satisfactory. Candidates include mechanically rechargeable primary batteries, secondary batteries and fuel cells (1-9). Nonaqueous systems are being actively developed²⁻⁷, but challenges of environmental compatibility, conductivity, cost, safety or power density remain and aqueous systems dominate both the consumer and electric propulsion market (1). There have been few new high capacity aqueous batteries introduced. Aqueous batteries utilizing metal hydride or air cathodes are being actively developed, and challenges including cost, CO₂ poisoning and power densities are being addressed (7-9).

An environmentally compatible novel aqueous aluminum/permanganate battery is discussed with the potential for unusually high pulsed power densities and with high theoretical sustained specific energy.

Conventional nickel/cadmium and lead acid batteries have moderate to low energy densities and adverse environmental impact. As seen in Table I, zinc/silver oxide batteries have a higher theoretical energy capacity, however the silver oxide cathode is not cost effective for large scale systems (7).

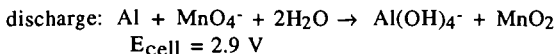
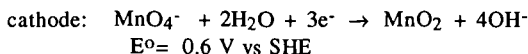
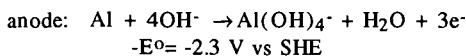
Compared to zinc cells, aluminum cells can yield substantially higher energy capacities. The theoretical potential of an aluminum anode is greater than one volt more favorable than the zinc anode potential. Furthermore, the theoretical storage capacity of Al (2980 A hr/kg) is substantially higher than that of zinc (820 A hr/kg). As seen in Table I, these combined characteristics lead to a three fold higher energy capacity for aluminum compared to zinc/silver oxide batteries. Aluminum/silver oxide batteries have among the highest measured steady

state power densities, and are useful for the requisite high discharge rates necessary for electrochemical propulsion (7, 12). However the high cost of silver is an impediment to the use of aluminum/silver oxide cells for land-based electric vehicle propulsion.

Aluminum is among the most common elements, and its light weight, electronegative potential and three electron oxidation state make it a compelling anode material (9). Electronegative anodes such as aluminum might be considered incompatible (reactive) when immersed in a strong oxidizing agent. However, this problem is circumvented by utilizing the extraordinarily high oxidative currents accessible for aluminum in aqueous alkaline media (10,11). We recently used a model system with a ferricyanide cathode to demonstrate that such aluminum batteries are possible when the redox phase cathode can also support high current densities (10). The Al/ferricyanide demonstrated high power densities (in excess of $2\text{W}/\text{cm}^2$ over simple planar surfaces). Al/ferricyanide has a modest specific energy (96 Wh/kg) which can be theoretically exceeded by an alternative aluminum/permanganate cell (Table I). A permanganate cell operating in a manner similar to the Al/ferricyanide cell may also provide high power densities.

(Mn(IV)) has found wide spread, cost effective use in Leclanché and alkaline batteries and does not pose the environmental threat of cadmium or lead in batteries (7). Permanganate (Mn(V)), MnO_4^- , has a more attractive cathodic potential and storage capacity than MnO_2 .

The new battery is expressed by aluminum oxidation and permanganate reduction:



Based on lithium, sodium or potassium salts this represents high theoretical specific energies respectively of 1230, 1140 and 1070 Wh/kg. A comparison of the capacities of aluminum/permanganate and existing cells including our recent aluminum/sulfur battery (13) is provided in Table I accentuating the theoretical advantage of the permanganate cell.

REFERENCES

1. "Energy Workshop on Advanced Battery Technology Research and Development ", A. Weber, Chair", Division of Chemical Sciences, Office of Basic Energy Science, U.S. Dept. of Energy, June 16-17, 1992, Report Published September, 1992.
2. C. A. Angell, C. Liu, E. Sanchez, *Nature*, **362**, 137 (1993).
3. E. J. Plichta, W.K. Behl, *J. Electrochem. Soc.*, **140**, 46 (1993).
4. C. Scordilis-Kelley, J. Fuller, R. R. Carlin, J. S. Wilkes, *J. Electrochem. Soc.*, **139**, 694 (1992).
5. K. E. Heusler, A. Grzegorzewski, *J. Electrochem. Soc.*, **140**, 426 (1993).
6. H. Sasaki, M. Suzuki, S. Ootoshi, A. Kalimura, M. Ipopommatsu, *J. Electrochem. Soc.*, **139**, L12 (1992).
7. D. Linden, "Handbook of Batteries", McGraw-Hill, NY (1984).
8. N. Kuriyama, T. Sakai, H. Miyamua, I. Uehara, H. Ishikaras, *J. Electrochem. Soc.*, **139**, L72 (1992).
9. K. Y. Chu, and R. F. Savinell, *J. Electrochem. Soc.*, **138**, 1976 (1991).
10. S. Licht, C. Marsh, *J. Electrochem. Soc.*, **139**, L109 (1992).
11. D. Chu, R. F. Savinell, *Electrochimica Acta*, **36**, 1631 (1991).
12. G. E. Anderson U. S. Patent 3,953,239 (1976).
13. S. Licht, D. Peramunage, *J. Electrochem. Soc.*, **140**, L4 (1993).

Table I. Conventional and new high energy density aqueous batteries.

System	Cell Potential, OCV		Charge Capacity*	Maximum* Energy Density
	Theoretical	Observed		
Lead Acid	2.04 V	2.0 V	83 Ahr/kg	174 Whr/kg
Nickel/Cadmium	1.35 V	1.2 V	181 Ahr/kg	244 Whr/kg
Zinc/Silver Oxide	1.57 V	1.4 V	199 Ahr/kg	312 Whr/kg
Aluminum/Silver Oxide	2.69 V	2.0 V	378 Ahr/kg	1020 Whr/kg
Aluminum/Ferricyanide	2.8 V	2.2 V	81 Ahr/kg	227 Whr/kg
Aluminum/Sulfur	1.8 V	1.4 V	595 Ahr/kg	1070 Whr/kg
Aluminum/Permanganate	2.9 V	2.3 V	476 Ahr/kg	1380 Whr/kg

*Theoretical, per kg stored reactant, assumes water activated cell in a H₂SO₄ or sodium (hydroxide) electrolyte

APPLICATIONS OF X-RAY ABSORPTION FINE STRUCTURE TO THE *IN SITU*
STUDY OF THE EFFECT OF COBALT IN NICKEL HYDROUS OXIDE ELECTRODES
FOR FUEL CELLS AND RECHARGEABLE BATTERIES

Sunghyun Kim,^o Donald A. Tryk,^o Mark R. Antonio⁺ and Daniel Scherson^o

^oDepartment of Chemistry
Case Western Reserve University
Cleveland, OH 44106-7078

⁺ Argonne National Laboratory
Chemistry Division
Argonne, IL 60439

Keywords: Nickel hydrous oxide electrodes, X-ray absorption fine structure,
in situ spectroelectrochemistry

INTRODUCTION

Nickel oxide electrodes have found widespread application in a variety of energy storage and energy generation devices, including rechargeable batteries and fuel cells.¹ The addition of certain metal cations to the nickel hydrous oxide lattice can profoundly affect its electrochemical characteristics.¹ In particular, cobalt has been found to shift the potential associated with the oxidation of $\text{Ni}(\text{OH})_2$ to NiOOH ² and to improve the charge acceptance of nickel oxide electrodes used in alkaline batteries.¹ In contrast, composite nickel oxide films involving iron as the guest metal exhibit high electrocatalytic activity for oxygen evolution and, as such, may be of practical value in alkaline water electrolysis.^{3,4}

The studies presented herein have been aimed at elucidating the structural and electronic properties of composite nickel-cobalt hydrous oxides using *in situ* X-ray absorption fine structure (XAFS) as a probe of the host (Ni) and guest (Co) metal sites in the lattice.

Basic aspects of XAFS as applied to the study of electrochemical interfaces have been amply reviewed in the literature⁵ and will not be discussed here. This technique can provide structural information without relying on long range order. This factor is of crucial importance, as high charge storage capacities can only be achieved by using materials in high area form, which are in many cases amorphous or consist of particles that are too small to achieve sufficient coherence for standard X-ray diffraction techniques to be very useful. Furthermore, high intensity X-rays in the energy range of interest can penetrate through thin electrolyte layers and low-Z window materials, such as organic polymers and thin aluminum sheets. This provides a means of performing measurements *in situ*, that is, with the electrode under potential control in an appropriately designed electrochemical cell.

EXPERIMENTAL

Pure metal (either nickel or cobalt) and nickel-cobalt composite hydrous oxides were prepared by cathodic (galvanostatic) electrodeposition^{2,6} from solutions of the corresponding metal nitrates on a solid graphite electrode. After deposition, the films were rinsed with

water and characterized in the spectroelectrochemical cell first by cyclic voltammetry and subsequently by XAFS in deaerated 1.0 M KOH. The cell for *in situ* fluorescence XAFS experiments employed in this study has been described elsewhere.⁷

In situ XAFS measurements for the pure Ni and Ni/Co hydrous oxide films were conducted in the discharged (i.e., reduced) and partially and nominally fully charged (i.e., oxidized) states. For the latter experiments, the potential was first scanned to a value more positive than the onset of oxygen evolution and then reversed to a value sufficiently negative for the current to drop essentially to zero but still positive with respect to the onset of NiOOH reduction. This strategy made it possible to eliminate problems associated with oxygen bubble formation during spectral acquisition. For measurements involving partially oxidized films, the potential was scanned up to a value on the rising part of the Ni(OH)₂ oxidation peak and then reversed to a no-current voltage condition.

All experiments were performed at beam-line IV-2 at the Stanford Synchrotron Research Laboratory. Details regarding these measurements as well as the method employed in the analysis of the EXAFS data have been given in previous work.⁸

RESULTS AND DISCUSSION

I. ELECTROCHEMISTRY

The cyclic voltammogram of a composite 9:1 Ni/Co hydrous oxide in 1.0 M KOH, shown in curve a, Figure 1, displayed characteristic oxidation and reduction peaks associated with the Ni(OH)₂/NiOOH redox process. In agreement with the observations of Corrigan,² but at variance with those of Cordoba et al.,⁴ the overpotential for oxygen evolution was larger for this composite oxide than for a pure nickel hydrous oxide prepared using the same procedure (see curve b, Figure 1). Also in harmony with earlier data⁴ are the shifts in the Ni(OH)₂/NiOOH redox features in the negative direction (ca. 50 mV) induced by the presence of Co in the Ni hydrous oxide lattice. As pointed out by Corrigan and Bendert,² no voltammetry features associated with the Co(OH)₂/CoOOH redox couple can be identified for this composite Ni/Co film. This is particularly interesting, as the redox peaks of pure Co hydrous oxide in this same electrolyte occur at a potential of 0.09 V and thus more negative than those observed for a pure Ni film and therefore should be clearly discernable in the voltammogram.

II. XANES

A. Nickel K-edge

The Ni K-edge XANES for the composite Ni/Co hydrous oxide film in the reduced (fully discharged) and oxidized (nominally charged) state recorded at -0.3 and +0.3 V vs. SCE, in 1.0 M KOH are shown in Curves a and b, Fig. 2, respectively. These curves are nearly identical to those reported by Pandya et al.⁹ for pure Ni hydrous oxide in 1.0 M KOH. Particularly noticeable is the shift in the overall absorption edge region toward higher X-ray energies for the oxidized (Ni³⁺) film compared to the reduced (Ni²⁺) film, including the peak at about 8363 eV. As discussed by Pandya et al.,⁹ the pre-edge feature at about 8332 eV is ascribed to the 1s → 3d electronic

transition, for which the intensity is found to be larger for the oxidized than for the reduced state. It must be stressed that in both cases this spectral feature is relatively small and therefore consistent with a slightly distorted octahedral environment.

B. Cobalt K-edge

The Co K-edge XANES for the Ni/Co composite film in the oxidized and reduced states are very similar (see Curves a and b, Fig. 3) displaying a very small pre-edge peak. This observation provides strong evidence that the nature of the cobalt sites is not modified by the structural and electronic changes in the lattice associated with redox processes involving the nickel sites. A comparison between these curves and those obtained for pure cobalt hydrous oxide films (prepared using the same electrodeposition method: see curve c in this figure)⁸ clearly shows that the cobalt sites in the latter composite hydrous oxide can be assigned to Co^{3+} . This is somewhat surprising since Co^{2+} in a pure cobalt hydrous oxide film undergoes oxidation at a potential only slightly more negative than that observed for the $\text{Ni}(\text{OH})_2/\text{NiOOH}$ couple.⁴ As is well known, however, the nature of the ligands can profoundly alter the redox potential of the $\text{Co}^{3+}/\text{Co}^{2+}$ couple, e.g., $E^\circ[\text{Co}(\text{NH}_3)_6]^{2+/3+} = 0.108 \text{ V}$, while $E^\circ[\text{Co}(\text{H}_2\text{O})_6]^{2+/3+} = 1.83 \text{ V}$.¹⁰ It can therefore be concluded that the environment of the cobaltic ions in the hydrated nickel oxide lattice is such that the potential required for their reduction is shifted to much more negative values. Such a claim has been made earlier in the literature, although without much substantiation.¹¹ Additional evidence for the presence of Co^{3+} sites in these composite hydrous oxides was obtained from the *in situ* Co K-edge EXAFS data (*vide infra*).

III. EXAFS

A. Nickel K-edge

The Fourier transforms (FTs) (without phase shift correction) of the $k^3\chi(k)$ Ni K-edge EXAFS for the Ni/Co hydrous oxide films in the reduced (-0.30 V vs. SCE) and oxidized (+0.30 V) states (see Curves a and b, Fig. 4, respectively) are very similar to those reported by Pandya et al.^{9,12,13} for the oxidized and reduced forms of battery-type nickel hydrous oxide electrodes. In accordance with their observations, the Ni-O and Ni-Ni distances within the sheet-like NiO_2 layers (1st and 2nd major shells, respectively) were found to be somewhat smaller for the nominally oxidized film, $d(\text{Ni-O}) = 1.92 \pm 0.02 \text{ \AA}$, $d(\text{Ni-Ni})_1 = 2.82 \pm 0.02 \text{ \AA}$, shown in Curve b, Fig. 4, compared to its reduced counterpart, $d(\text{Ni-O}) = 2.09 \pm 0.02 \text{ \AA}$, $d(\text{Ni-Ni})_1 = 3.11 \pm 0.02 \text{ \AA}$. The close similarity between the results obtained for the pure and composite Ni/Co hydrous oxide films indicates that within the sensitivity of this technique, the presence of cobalt at a nominally 10 metal-atom percent does not appear to significantly affect the structure of the nickel hydrous oxide.

Unlike the behavior observed for composite Ni/Fe hydrous oxide films in the nominally fully oxidized state, for which contributions due to Ni^{2+} were invariably observed, the Ni-Ni shell for a fully oxidized 9:1 composite Ni/Co film displayed a single well-defined shell attributed to Ni^{3+} sites.

This affords unambiguous evidence that under these conditions the nickel in Ni/Co films can be completely oxidized, leaving no residual Ni^{2+} ions in the lattice.

C. Cobalt K-Edge

A number of interesting conclusions can be drawn from the analysis of the FT of the $k^3\chi(k)$ Co K-edge EXAFS spectra of these composite Ni/Co films (see Figure 5). In particular, the best fit to the Co K-edge EXAFS data yielded a value of $d(\text{Co-O}) = 1.90 \pm 0.02 \text{ \AA}$ and thus, within experimental error, is identical to $d(\text{Co-O})$ in crystalline CoOOH , i.e., 1.90 \AA .¹⁴ This observation is consistent with the presence of cobaltic sites in the lattice, as proposed on the basis of the XANES data. More noteworthy, however, is the fact that composite Ni/Co films purposely charged only partially (obtained at +0.32 V; see curve c, Figure 5) displayed clearly resolvable Co-Ni shells associated with $\text{Co}^{3+}\text{-Ni}^{2+}$ and $\text{Co}^{3+}\text{-Ni}^{3+}$ interactions. These results clearly indicate that the co-electrodeposition procedure generates a single phase, mixed metal hydrous oxide, in which cobaltic ions occupy nickel sites in the NiO_2 sheet-like layers and not two intermixed phases each consisting of a single metal hydrous oxide.

LITERATURE

1. McBreen, J. In *Modern Aspects of Electrochemistry*, Conway, B.; White, R.; Bockris, J. O'M., Eds.; Plenum Press: New York, 1991, Vol. 23.
2. Corrigan, D. A.; Bendert, R. M. *J. Electrochem. Soc.* 1989, 136, 723.
3. Corrigan, D. A. *J. Electrochem. Soc.* 1987, 134, 377.
4. Cordoba, S. I.; Carbonio, R. E.; Lopez Tejel, M.; Macagno, V. A. *Electrochim. Acta* 1986, 31, 1321.
5. Abruna, H. D. In *Electrochemical Interfaces*, Abruna, H. D. Ed.; VCH: New York, 1991, Chapter 1.
6. Burke, L. D.; Twomey, T. A. *M. J. Power Sources* 1984, 12, 203.
7. Kim, S.; Bae, I. T.; Sandifer, M.; Ross, P. N.; Carr, R.; Woicik, J.; Antonio, M. R.; Scherson, D. A. *J. Am. Chem. Soc.* 1991, 113, 9063.
8. Kim S.; Tryk, D. A.; Antonio, M. R.; Scherson, D. A. *J. Phys. Chem.* submitted, March 1993.
9. Pandya, K. I.; Hoffman, R. W.; McBreen, J.; O'Grady, W. E. *J. Electrochem. Soc.* 1990, 137, 383.
10. Milazzo, G.; Caroli, S. *Tables of Standard Electrode Potentials*, Wiley: New York, 1978, pp. 337.
11. Weininger, J. L. In *The Nickel Electrode*, Gunther, R. G.; Gross, S.; Eds., Proceedings of the Symposium, The Electrochemical Society, 1982.
12. McBreen, J.; O'Grady, W. E.; Pandya, K. I.; Hoffman, R. W.; Sayers, D. E. *Langmuir* 1987, 3, 428.
13. Pandya, K. I.; O'Grady, W. E.; Corrigan, D. A.; McBreen, J.; Hoffman, R. W. *J. Phys. Chem.* 1990, 94, 21.
14. Delaplane, R. G.; Ibers, J. A.; Ferraro, J. R.; Rush, J. J. *J. Chem. Phys.* 1969, 50, 1920.

ACKNOWLEDGEMENTS

This work was supported in part by the Department of Energy through a subcontract from Lawrence Berkeley Laboratory. Additional funding was provided by Eveready Battery Co., Westlake, Ohio.

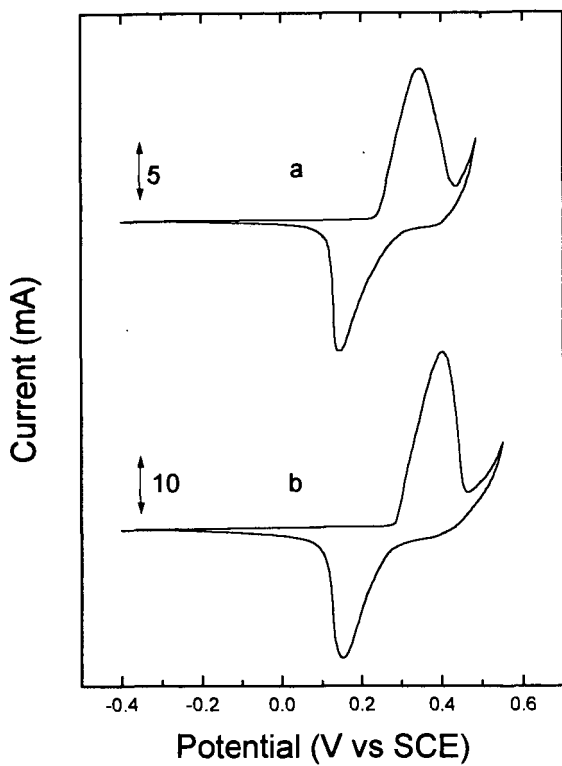


Fig. 1 Cyclic voltammetry curves for composite 9:1 Ni/Co (curve a) and a pure Ni (curve b) hydroxide electrode in deaerated 1.0 M KOH. Scan rate: 5 mV s^{-1} . Cross sectional electrode area: 0.74 cm^2 .

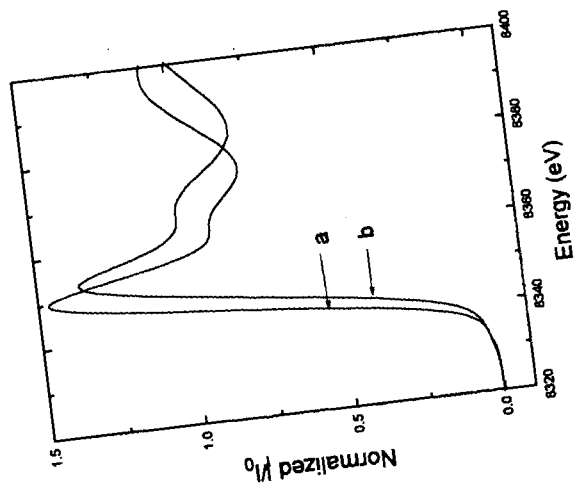


Fig. 2 Ni K-edge XANES for a composite 9:1 Ni/Co hydrous oxide film in the fully discharged (Curve a) and nominally fully oxidized (Curve b) recorded at -0.3 V and $+0.3$ V vs SCE, respectively in 1.0 M KOH.

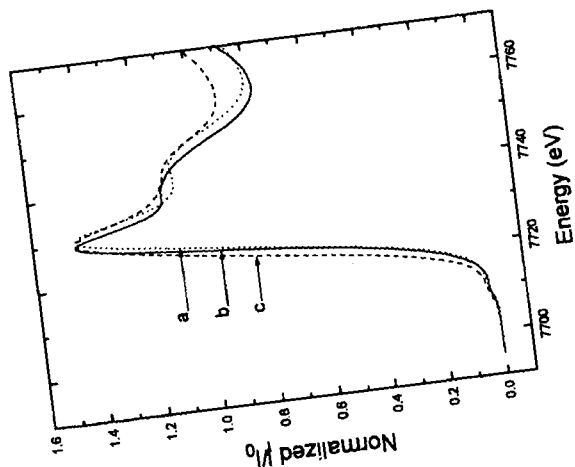


Fig. 3 Co K-edge XANES for a composite 9:1 Ni/Co hydrous oxide film in the oxidized (0.3 V) and reduced (-0.3 V) states (Curves a and b, respectively). Also shown in this figure are the corresponding spectra for a pure Co hydrous film prepared by the same electrodeposition procedure described in the Experimental Section in the reduced state (Curve c).

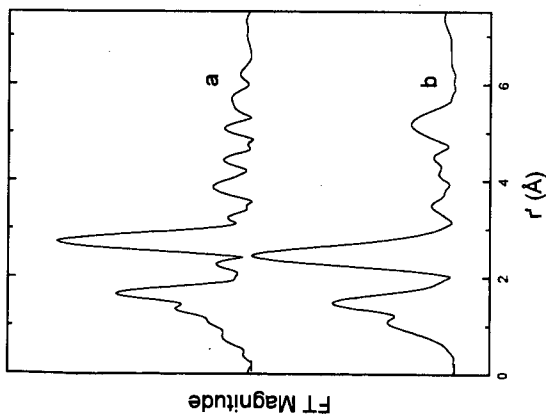


Fig. 4 Phase-uncorrected FT for the $k^3\chi(k)$ Ni K-edge EXAFS for 9:1 Ni/Co hydrous oxide films in the reduced (-0.3 V vs SCE, Curve a), and oxidized (+0.30 V, Curve b) states.

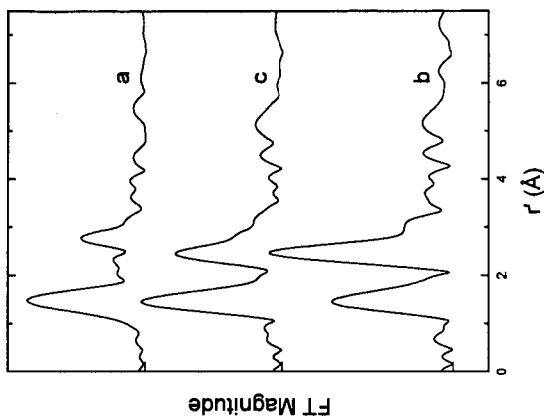


Fig. 5 Phase-uncorrected FT for the $k^3\chi(k)$ Co K-edge EXAFS for 9:1 Ni/Co hydrous oxide films in the reduced (Curve a), fully oxidized (Curve b) and partially oxidized (obtained at +0.32 V, Curve c) states. Other conditions are given in the Caption Figure 2.

THEORETICAL DISCHARGE CURVES FOR NICKEL HYDROXIDE

John W. Weidner
Department of Chemical Engineering
University of South Carolina
Columbia, SC 29208

Paul Timmerman
Jet Propulsion Laboratory
California Institute of Technology
Pasadena, CA 91109

ABSTRACT

Discharge curves for the nickel hydroxide electrode are simulated assuming resistances due to diffusion of protons and conduction of electrons through the active nickel hydroxide film as well as charge-transfer resistance at the film/electrolyte interface contribute to the polarization losses of the electrode. Previous models which have combined these three resistances into a pseudocharge-transfer resistance predict discharge curves which are higher and flatter than experimental data, and material utilization which is unrealistically high. The present model predicts realistic trends as a function of discharge rates. In addition, the governing equations have been solved analytically which allows the model of the active film to be integrated into our battery models.

INTRODUCTION

Battery models that can predict the effect of operating conditions on battery life and performance are extremely valuable to battery users and manufacturers. Model predictions can provide quality assurance that the batteries being manufactured are of consistently high quality, and provide indicators well in advance of failure so that steps can be taken to adjust operating condition and prolong battery life. In addition, a variety of design parameters can be investigated to aid an electrode development program.

Theoretical discharge curves have been generated by a number of investigators [1]—[5] using a one-dimensional, macrohomogeneous model. The spatial dimension of interest is in the direction perpendicular to the current collectors, and therefore the polarization loss across the $\text{NiOOH}/\text{Ni}(\text{OH})_2$ active film is assumed to be due solely to charge-transfer resistance. Although these models reveal the importance of transport limitations in the electrolyte phase, they predict nickel electrode potentials as a function of time which are larger and more constant than experimental data. They also predict material utilization on discharge which is unrealistically high. Sinha [10] developed a model of a porous electrode in which the solid active material was described using semiconductor theory. This model, however, contains many parameters that can not be obtained experimentally.

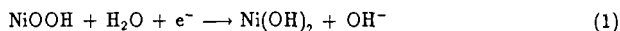
Experimentally it has been suggested that proton diffusion and ohmic drop in the active material may contribute appreciably to overall polarization losses [6]—[8]. Two dimensional,

macrohomogeneous models have been developed to account for the diffusion of protons in the active nickel hydroxide film [9] and diffusion coupled with electronic resistance of the film [11]. One of the rationals for including variable electronic resistance in the later model [11] is that the nickel hydroxide is an electrical insulator in the reduced state and a conductor in the oxidized state. The drawback of these models is that the solution procedure requires a large amount of computer memory and computational time.

In this paper, an analytical solution is given which accounts for proton diffusion and variable electronic conductivity in the film. This solution can be used in conjunction with a one-dimensional, macrohomogeneous model to achieve the results obtained by Mao *et al.* [11], but with considerably less computer power. In addition, the analytical solution can be used to simulate electroanalytical techniques in order to extract kinetic, transport, and electronic resistance parameters from experimental data.

MATHEMATICAL MODEL

The discharge reaction at the nickel electrode is generally expressed as



Proton diffusion into the bulk of the solid phase makes it possible for this reaction to continue at the film/electrolyte interface. The kinetic expression given by previous investigators [5, 11] is used to relate the current to the potential driving force and proton concentration at this interface. For a constant current discharge, this expression can be written in dimensionless form as

$$1 = I_0 \left[(1 - \theta_s) e^{\alpha_s \Phi_s} - \theta_s e^{-\alpha_s \Phi_s} \right] \quad (2)$$

where θ_s is the state-of-charge at the film/electrolyte interface and is related to the proton concentration at this surface by

$$\theta_s = 1 - C_s (1 - \theta^0) \quad (3)$$

and Φ_s is the dimensionless potential driving force at the surface defined as

$$\Phi_s = \frac{F}{RT} (\phi_s - U_{\text{ref}}) \quad (4)$$

The dimensionless potential driving force, therefore, is the potential drop across the film/electrolyte interface relative to a reference potential ($U_{\text{ref}} = 0.440$ V versus SHE which is the open circuit potential for Ni(OH)_2 at a degree of discharge of 0.5 in 31% KOH). (See the notation section and Table 1 for a complete list of variable and parameter definitions, respectively.)

In order to obtain C_s , the concentration profile of protons in the nickel hydroxide film must be obtained as a function of time. It is assumed that the proton concentration in the film is governed by the time-dependent, one-dimensional diffusion equation. In dimensionless form this equation can be written as

$$\frac{\partial C}{\partial \tau} = \frac{\partial^2 C}{\partial Y^2} \quad (5)$$

The initial proton concentration is uniform, the proton concentration gradient is zero at the film/substrate interface ($Y = 0$), and the concentration gradient is proportional to the current at the film/electrolyte interface ($Y = 1$). The initial and boundary conditions can be written as:

$$(5a) \quad \tau = 0; \quad C = 1$$

$$(5b) \quad Y = 0; \quad \frac{\partial C}{\partial Y} = 0$$

$$(5c) \quad Y = 1; \quad \frac{\partial C}{\partial Y} = \frac{1}{D(1-\theta^0)}$$

The Laplace transform of equation 5 is taken with respect to τ , the resulting ordinary differential equation for the transformed concentration is solved, and the solution is inverted back to the time domain resulting in

$$C(Y, \tau) = 1 + \frac{1}{D(1-\theta^0)} \left[\tau + 2 \sum_{k=1}^{\infty} \frac{(-1)^k \cos(k\pi Y)}{k^2 \pi^2} (1 - e^{-k^2 \pi^2 \tau}) \right] \quad (6)$$

In order to obtain the applied potential, ohm's law must be integrated from the conducting substrate ($Y = 0$) to the electrolyte ($Y = 1$) giving the following expression at room temperature.

$$\text{applied potential (mV vs SHE)} = 440 + 25.7 \left[\Phi_s + \frac{1}{\Theta} \int_0^1 \frac{dY}{\sigma(Y, \tau)} \right] \quad (7)$$

where

$$\sigma(Y, \tau) = \exp \left[-24.45 (1 - \theta^0)^4 C^4 \right] \quad (8)$$

Note that for a constant current discharge

$$\text{degree of discharge} = (1 - \theta^0) + \tau/D \quad (9)$$

RESULTS AND DISCUSSION

Figure 1 shows the effect of discharge rate on discharge curves for nickel hydroxide. The term c/n is the current which causes the electrode to completely discharge in n hours. Each curve was obtained by solving equation 6 at $Y = 1$, solving equation 2 for Φ_s , obtaining the applied potential from equation 7, and then repeating these steps at successive points in time. The values used to calculate the dimensionless parameters given in Figure 1 are listed in Table 2.

The convergence of the series in equation 6 was accelerated using Richardson extrapolation [13] and a binomial averaging algorithm [14] for $Y = 1$ and $Y \neq 1$, respectively. Equation 7 was integrated numerically using Simpson's rule, and Newton's method was used to obtain Φ_s from equation 2.

Three features which are observed experimentally are also seen in the theoretical discharge curves shown in Figure 1. The first feature is the curvature observed during the early stages of discharge (degree of discharge < 0.05). The other two features seen in Figure 1 are the potential dependence of the middle plateau and the abrupt drop in the potential as a function of discharge rate. This abrupt drop in potential is a critical characteristic of the discharge curve since the electrode loses its energy producing capability at this point and the remaining capacity can not be utilized.

It is unclear from Figure 1 what the relative contributions of mass-transfer, ohmic, and kinetic resistances are to the observed polarization losses. Figures 2-4 were generated at a discharge rate of $c/2$ in order to isolate the individual resistances, and determine their effect on the discharge

curves. The polarization losses seen in Figure 2 are due solely to kinetic resistance since \mathcal{D} and Θ were increased by many orders of magnitude. Kinetic resistance alone can not account for two of the three trends observed experimentally. Namely, utilization is not affected by kinetic limitations since approximately 100% utilization is observed even when kinetic resistance (or discharge rate) is increased two orders-of-magnitude from the base case. The curvature of the discharge curves is also lost as kinetic resistance is increased relative to discharge time. This observation suggests that kinetic resistance may be a small contributor to the overall polarization losses observed in a nickel hydroxide electrode.

The polarization losses seen in Figure 3 are due solely to the mass-transfer resistance of protons through the active nickel hydroxide film. The same trends seen in Figure 1 are observed in Figure 3. Consequently, diffusion alone could account for curvature during the early stages of discharge, and a middle plateau and material utilization which are functions of discharge rate.

Figure 4 shows the polarization losses due to ohmic resistance. Curvature is seen at the early stages of discharge, and material utilization decreases as ohmic resistance relative to discharge time increases. However, a four order-of-magnitude increase in ohmic resistance did not affect utilization as much as a one order-of-magnitude increase in mass-transfer resistance did. In addition, polarization losses at the midpoint of discharge are not a function of discharge rate. As with kinetic resistance, ohmic resistance alone can not account for all the trends observed from experimental discharge curves.

CONCLUSIONS

Discharge curves for the nickel hydroxide electrode were simulated assuming resistances due to diffusion of protons and conduction of electrons through the active nickel hydroxide film as well as charge-transfer resistance at the film/electrode interface contribute to the polarization losses of the electrode. The model was able to predict realistic trends as a function of discharge curves. The results suggest that polarization losses due to diffusional limitations of protons is a critical factor in determining the shape of the discharge curve. Variable electronic resistance has a noticeable effect on the discharge curve but it alone can not account for all the observed trends. Charge-transfer resistance is insignificant relative to ohmic and mass-transfer resistance.

NOTATION

c_{H^+}	proton concentration, mol/cm ³
$c_{H^+}^0$	proton concentration, mol/cm ³
c_{Ni}	concentration of nickel sites, mol/cm ³
C	dimensionless proton concentration, $c_{H^+}/c_{H^+}^0$
C_s	dimensionless proton concentration at $Y = 1$
D_{H^+}	diffusion coefficient for protons, cm ² /s
f	F/RT , V ⁻¹
F	Faraday's constant, C/equiv
i	current density, A/cm ²
i_0	exchange current density, A/cm ²
l	thickness of the nickel hydroxide layer, cm
n	hours required for complete discharge, hr
R	gas constant, J/(mol·K)
t	time, s
T	temperature, K

U_{ref}	open-circuit potential, V
y	distance from the film/substrate interface, cm
Y	dimensionless distance, y/l
Greek	
α_a	anodic transfer coefficient
α_c	cathodic transfer coefficient
θ_s	state-of-charge at $Y = 1$
θ^0	initial state-of-charge
σ	dimensionless conductivity
σ^0	initial conductivity, $(\text{ohm}\cdot\text{cm})^{-1}$
ϕ_s	potential drop across film/electrolyte interface, V
Φ_s	dimensionless potential driving force at $Y = 1$
τ	dimensionless time, tD_{H^+}/l^2

References

- [1] Choi, K. W. and N. P. Yao, **Proceedings of the Symposium on Battery Design and Optimization**, S. Gross (ed.), The Electrochemical Society Inc., Princeton, NJ (1979).
- [2] Micka, K. and I. Roušar, *Electrochim. Acta*, **25**, 1085 (1980).
- [3] Micka, K. and I. Roušar, *Electrochim. Acta*, **27**, 765 (1982).
- [4] Fan, D. and R. E. White, *J. Electrochem. Soc.*, **138**, 17 (1991).
- [5] Fan, D. and R. E. White, *J. Electrochem. Soc.*, **138**, 2952 (1991).
- [6] G. W. D. Briggs, and P. R. Snodin, *Electrochim. Acta*, **27**, 565 (1982).
- [7] Zimmerman, A. H. and P. K. Effa, *J. Electrochem. Soc.*, **131**, 709 (1984).
- [8] Zhang, C. and S. Park, *J. Electrochem. Soc.*, **134**, 2966 (1987).
- [9] Bouet, J., F. Richard, and P. Blanchard, *Proceedings of the Symposium on Nickel Hydroxide Electrodes*, D. A. Corrigan and A. H. Zimmerman, Eds., p. 260, The Electrochemical Society Inc., NJ (1990).
- [10] Sinha, M., *A Mathematical Model for the Porous Nickel Hydroxide Electrode*, Dissertation, University of California, Los Angeles, 1982.
- [11] Mao, Z. R. E. White, and J. Newman, Submitted to, *J. Electrochem. Soc.* (1992).
- [12] Delahay, P., *J. Am. Chem. Soc.*, **75**, 1190 (1953).
- [13] Bender, C. M. and S. A. Orszad, **Advanced Mathematical Methods for Scientists and Engineers**, McGraw Hill, New York, NY (1978).
- [14] Dahlquist, G. and Å. Björk, **Numerical Methods**, Translated by N. Anderson, Prentice Hall, New York, NY (1974).

<u>Parameter</u>	<u>Interpretation</u>	<u>Definition</u>
\mathcal{D}	$\frac{\text{discharge time}}{\text{mass-transfer resistance}}$	$\frac{3600n D_{H^+}}{l^2}$
I_o	$\frac{\text{discharge time}}{\text{charge-transfer resistance}}$	$\frac{3600n i_o}{F C_{Ni} l}$
Θ	$\frac{\text{discharge time}}{\text{ohmic resistance}}$	$\frac{3600n \sigma_o}{f F C_{Ni} l^2}$

Table 1: The definitions of the dimensionless parameters that govern discharge curves in nickel hydroxide.

$c_{Ni} = 0.040 \text{ mol/cm}^3$	$D_H^+ = 4.6 \times 10^{-11}$
$i_o = 6.0 \times 10^{-3} \text{ A/cm}^2$	$l = 5.0 \times 10^{-4} \text{ cm}$
$\sigma^o = 0.1185 \text{ (ohm}\cdot\text{cm)}^{-1}$	$T = 293 \text{ K}$
$\alpha_a = \alpha_c = 0.5$	$\theta^o = 0.99$

Table 2: Parameters used to obtain Figure 1 [11]. The three dimensionless parameters that result from these values are listed in Figure 1.

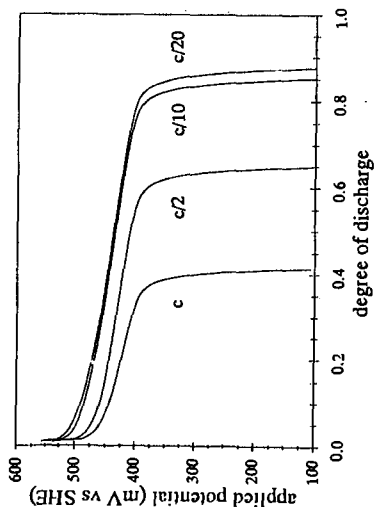


Figure 1: The effect of discharge rate on discharge curves for nickel hydride. The term c/n is the current which causes the electrode to completely discharge in n hours. As n increases the discharge rate decreases. ($\Theta = 11,380$ h, $I_a = 11.19$ A, $D = 0.662$ cm²)

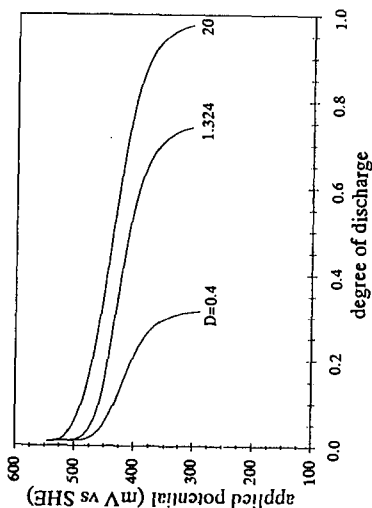


Figure 3: The effect of proton mass-transfer resistance on a $c/2$ discharge curve. As D increases, mass-transfer resistance decreases relative to discharge time. ($\Theta = 2 \times 10^3$, $I_a = 22.38$)

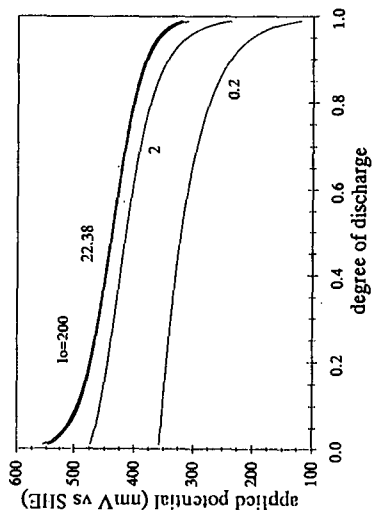


Figure 2: The effect of kinetic resistance on a $c/2$ discharge curve. As I_a increases, kinetic resistance decreases relative to discharge time. ($\Theta = 2 \times 10^3$, $D = 20,000$)

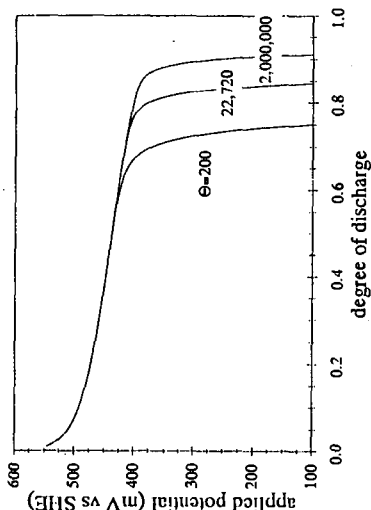


Figure 4: The effect of ohmic resistance on a $c/2$ discharge curve. As Θ increases, the ohmic resistance decreases relative to discharge time. ($I_a = 22.38$, $D = 20,000$)

FUEL PROCESSING REQUIREMENTS AND TECHNIQUES FOR FUEL CELL PROPULSION POWER

by

R. Kumar, S. Ahmed, and M. Yu
Argonne National Laboratory
Chemical Technology Division
9700 South Cass Avenue
Argonne, IL 60439

Keywords: Fuel Cells, Reformers, Methanol

ABSTRACT

Fuels for fuel cells in transportation systems are likely to be methanol, natural gas, hydrogen, propane, or ethanol. Fuels other than hydrogen will need to be reformed to hydrogen on-board the vehicle. The fuel reformer must meet stringent requirements for weight and volume, product quality, and transient operation. It must be compact and lightweight, must produce low levels of CO and other byproducts, and must have rapid start-up and good dynamic response. Catalytic steam reforming, catalytic or non-catalytic partial oxidation reforming, or some combination of these processes may be used. This paper discusses salient features of the different kinds of reformers and describes the catalysts and processes being examined for the oxidation reforming of methanol and the steam reforming of ethanol. Effective catalysts and reaction conditions for the former have been identified; promising catalysts and reaction conditions for the latter are being investigated.

INTRODUCTION

Electric vehicles powered by fuel cells require hydrogen as the fuel. This can be obtained directly from onboard pressurized cylinders. For example, Ballard Power Systems, Inc., will be unveiling a 9.75 m (32-ft.), 20 passenger bus later this year in Vancouver, British Columbia. This bus will be powered by a 100 kW polymer electrolyte fuel cell (PEFC), with hydrogen stored as compressed gas at 20.7 MPa (3000 psi). The driving range will be limited to 161 km (100 miles).

On a commercial level, the logistics of hydrogen supply to refueling stations, the mechanism of cylinder exchange or refueling at the stations, the driving range (i.e., the time/distance required between refueling), the weight penalty imposed due to a bulky and heavy cylinder, and the safety concerns of carrying a cylinder of hydrogen have led to a search for alternative hydrogen storage systems or alternative fuels from which hydrogen can be produced onboard.

Hydrogen can also be stored as a metal hydride or as an adsorbed gas on activated carbon. These methods require a large weight and volume per unit of hydrogen stored. Consequently, the amount of hydrogen that can be stored onboard is limited. In turn, the driving range of the vehicle is limited. Reforming of liquid fuels provides a viable alternative to on-board hydrogen storage. These fuels would preferably be liquids or capable of being liquefied at moderate to low pressures, can easily be made available at the refueling stations, and possess a high hydrogen/carbon ratio.

Of the different fuels being considered for use in fuel-cell powered vehicles, methanol has clear advantages in terms of fuel storage and distribution as it can be used with minimal disruption to the present fuel distribution network.^[1,2] Methanol is a commodity chemical; it can be manufactured from coal, natural gas, or other feedstocks; and can easily be reformed to hydrogen at low temperatures. Ethanol, another alternative, is a renewable energy source produced from corn or other biomass and has 30% more energy than an equal amount of methanol.

The fuel cell powered bus program, sponsored jointly by the Departments of Energy and Transportation (DOE/DOT) is planning to field test prototype buses. These 8.8-m (29-ft) long, 20-27 passenger buses will be powered by a battery combined with a phosphoric acid fuel cell. Liquid methanol will be reformed onboard to provide the hydrogen for the fuel cell.

An on-board fuel processor has to meet a number of restrictions unique to transportation applications. The fuel processor needs to be compact and lightweight, since the vehicles have limited space and the total vehicle weight determines the power requirements and thus the "engine" size. Depending on the type of fuel cell that receives the hydrogen-rich reformat, the quality of the reformat can be very important. For example, polymer electrolyte fuel cells (PEFC) are very sensitive to the levels of carbon monoxide in the reformat and contaminants such as formic acid, acetic acid, acetaldehyde.

On-board fuel processors need a rapid start-up capability, i.e., they should be able to warm up to reaction conditions and deliver the required hydrogen to the fuel cell very quickly. Non-steady state operation (acceleration, braking) being an integral part of transportation power requirements, the fuel processor must be responsive to changes in hydrogen demand and have a high turndown ratio (idling).

If the fuel processor is designed around a catalytic reformer, the above-mentioned constraints translate, in terms of the catalyst, to the following. The catalyst should be very active to achieve a compact, lightweight reactor; give good product selectivity to obtain high hydrogen fractions as well as minimize reformat cleanup; and operate at relatively low temperatures to enable rapid heatup to reaction conditions. In addition, the catalyst should be rugged – capable of withstanding the vibrations; should have a long life – not requiring frequent regeneration or recharging; and should possess good thermal properties – high thermal conductivity to avoid hot/cold spots and resistance to sintering. As always, the material cost and availability are important issues as well.

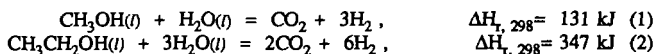
REFORMING AND REFORMERS

Fuel reformers are commonly used in chemical process industries for the manufacture of hydrogen from common feedstocks such as natural gas, propane, butane, and naphtha. The two most commonly used processes are (1) steam reforming and (2) partial oxidation in the presence of steam. Catalysts for the steam reforming process have already been demonstrated for methanol^[3] and methane.^[4]

Fuel reformers for the production of hydrogen for use in fuel cells have been developed more recently. Much of this development work, however, has concentrated on stationary applications, with essentially constant system load and process throughput. Reformers have been built and tested for converting methanol and natural gas to a hydrogen-rich fuel gas. Reforming of a variety of other fuels, including gasoline, diesel, and naphtha, has also been demonstrated. For constant-load stationary applications, steam reforming is preferred over partial oxidation reforming, since the former provides a higher overall

system efficiency as well as a reformat with a higher hydrogen concentration. Steam reforming is endothermic and requires the input of thermal energy.

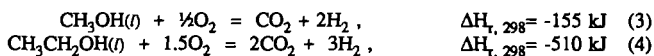
Methanol steam reforming is a well-studied reaction. The reaction stoichiometries for the steam reforming of methanol and ethanol are shown in Equations (1) and (2). Both reactions are endothermic.



Commercial catalysts can catalyze reaction (1) at relatively low temperatures (150°-250°C) with good selectivity. The catalysts are sufficiently active that the reformer designs are not limited by the reaction rate, but by the rate at which the heat for the endothermic reaction can be provided. Not surprisingly then, the reformer designs are more akin to heat exchangers than to conventional catalytic reactors. Several manufacturers have come up with various designs that look like shell-and-tube (Engelhard Corp.^[5]) and plate-and-frame (Ishikawajima-Harima Heavy Industries^[6]) heat exchangers. The packed-bed reformer built under the joint General Motors-Allison/Los Alamos National Laboratory^[7] program uses an electric heater and gas recycling to maintain the desired bed temperatures. The presence of the recycle stream also serves as a surge tank to meet limited transient needs.

At present, effective catalysts or reformers have not been demonstrated for the steam reforming of ethanol.

The reactions for partial oxidation reforming are exothermic, and the reaction stoichiometries for methanol and ethanol are shown in Equations (3) and (4).



Although a good partial oxidation reforming catalyst has been found at Argonne, the same cannot be said for the partial oxidation reforming of ethanol. Testing of the methanol partial oxidation catalyst and the search for an ethanol partial oxidation catalyst are continuing.

For transportation applications, the partial oxidation reformer can be much superior to the steam reformer with respect to its start-up and load-following performance.^[1] For example, during start-up the reaction, once ignited, generates its own heat and thus can heat up the catalyst bed within a very short time. In contrast, the steam reforming catalyst bed receives the heat from across a surface. Similarly, at times of acceleration, the partial oxidation reformer merely requires additional feed, whereas the steam reformer requires both additional feed and heat, the latter being supplied across a boundary.

The partial oxidation reformer, using air for the oxidation process, produces a reformat that contains nitrogen, which reduces the hydrogen concentration in the reformat stream. In comparison, the steam reformer can, theoretically, provide up to 75% hydrogen in the reformat stream.

CATALYSTS FOR PARTIAL OXIDATION OF METHANOL

A number of catalysts for the partial oxidation of methanol have been studied in the laboratory. The tests consisted of methanol and water vapors fed in with a helium stream, mixed with oxygen, and passed

over a catalyst bed (~0.5 g) at temperatures of 150-400°C. The product stream was analyzed with a gas chromatograph.

Table 1 shows the product distributions obtained with some of these materials. Column 1 (methanol) shows that the Co/SiO₂ gives the highest (100%) conversion, but the hydrogen fraction is quite low at 24%; most of the hydrogen produced is oxidized to water (52%), which is undesirable. The CuZnO gives the highest hydrogen fraction; its overall conversion is very good, with only 1.6% methanol in the product stream; and this catalyst produces no methane. Although some CO is produced, if necessary, it can be converted via the water-gas shift reaction at low temperatures. Of the materials tested, the CuZnO catalyst appears to be the best choice in terms of activity and selectivity.

Table 1. Methanol Partial Oxidation Products Obtained with Different Materials

Catalyst	CH ₃ OH vol. %	H ₂ O vol. %	CO ₂ vol. %	H ₂ vol. %	CO vol. %	CH ₄ vol. %	Others vol. %
Pd/SiO ₂	10.2	55	14	15	1.9	0.04	3.2
CuZnO	1.6	37	21	40	1.1	0	0
CuBiO/SiO ₂	9.8	76	11	2	0.2	0	1.1
FeZnO	10	52	15	22	0.7	0.4	0
Co/SiO ₂	0	52	18	24	0.5	5.1	0

Figure 1 shows the methanol conversion and hydrogen selectivity obtained with CuZnO as a function of temperature. Starting at a conversion of 70% at 275°C, the conversion increases and reaches nearly 98% at 325°C. At 400°C, all of the methanol gets converted. The level of hydrogen in the product stream remains almost unchanged at 63% throughout the temperature range. The maximum hydrogen mole percent achievable, as indicated from the reaction stoichiometry, is 67%. The figure also shows the levels of carbon monoxide, which is an undesirable product for low temperature fuel cells, such as the PEFC. The carbon monoxide does increase with temperature, but even at 400°C, it is a moderate 2%. Further testing of this catalyst in a bench-scale reformer is in progress.

CATALYSTS FOR STEAM REFORMING OF ETHANOL

A number of nickel-based catalysts have been studied in a reactor loaded with ~2 g of catalyst at temperatures of 250-450°C and fed a mixture containing 20 mol % ethanol (80 mol % water). The product gases were analyzed for hydrogen, carbon monoxide, carbon dioxide, and methane. A gas chromatograph was used for this analysis. The conversions were estimated from the product gas flow rates, ranging from 20 to 55%. Figure 2 shows the distributions in the gaseous product obtained with one of these catalysts as a function of temperature. At 250°C, the gaseous product was predominantly hydrogen (56%), carbon monoxide (23%), and methane (25%). With increasing temperature the CO fraction dropped sharply and was accompanied by increased fractions of carbon dioxide and methane. At ~400°C, the H₂ and CH₄ fractions passed through a minimum and maximum, respectively. Above 400°C, the CO₂ was found to level off, the CO and H₂ started to increase, while the methane fell off sharply to under 25%. The products also contained some acetaldehyde and acetic acid. The catalyst was found to deactivate due to coke deposition.

This product distribution suggests a reaction mechanism involving dehydrogenation of ethanol, followed by dissociation of acetaldehyde to form methane and carbon monoxide. The decreasing levels of carbon monoxide indicate some conversion via the water-gas shift reaction. This is consistent with other studies^[8] with nickel, where ethanol was found to undergo dissociation, leading all the way to coke deposition. Some other formulations showed lower conversions and higher levels of carbon monoxide.

The presence of methane in the product stream represents a loss in hydrogen-producing capacity, because the reforming of methane requires temperatures higher than 700°C. Other materials and formulations which will catalyze mechanisms offering better product selectivity are being investigated.

CONCLUSIONS

Fuel cells for transportation applications offer some choices and impose some unique restrictions upon the fuel processor. The choice of fuel, the weight/volume limitations, the rapid startup and transient response requirements, the need for durability in a mobile environment, and the overall efficiency of the fuel cell system are important considerations in the design of the fuel processor.

Methanol and ethanol have the potential to be the fuel of choice, provided the reforming processes can be demonstrated within the boundaries of the application requirements. Catalytic partial oxidation of methanol can provide the rapid startup and dynamic performance demanded in transportation applications, and a copper-zinc oxide catalyst is capable of supporting such a reformer.

Alternative reformer designs are being evaluated, and the catalyst screening continues for the steam reforming and partial oxidation reforming of ethanol.

ACKNOWLEDGEMENTS

This research was sponsored by the U.S. DOE Office of Transportation Technologies. Argonne National laboratory is operated by the University of Chicago for the U.S. DOE under Contract W-31-109-Eng-38.

REFERENCES

1. Kumar, R., Ahmed, S., Krumpelt, M., and Myles, K. M., "Reformers for the Production of Hydrogen from Methanol and Alternative Fuels for Fuel Cell Powered Vehicles," Argonne National Laboratory Report ANL-92/31, Argonne, IL, 1992.
2. Srinivasan, S., "Potential Fuel Cell System for Transportation Applications," Proceedings of Renewable Fuels and Advanced Power Sources for Transportation Workshop, National Renewable Energy Laboratory Report SERI-CP-234-1707, p. 139 (1982).
3. Amphlett, J. C., Evans, M. J., Mann, R. F., and Weir, R. D., "Hydrogen Production by Catalytic Steam Reforming of Methanol. Part 2: Kinetics of Methanol Decomposition using Girdler G66B Catalyst," *Canadian Journal of Chemical Engineering*, **63**, pp.605-611 (1985).
4. Rostrup-Nielsen, J. R., "Steam Reforming Catalysts," Danish Technical Press Inc., Copenhagen, Denmark, 1974.
5. Kaufman, A. and Werth, J., "Develop and Test Fuel Cell Powered On-site Integrated Total Energy Systems," DOE/NASA/0241-12, NASA CR-174951, October 1984.
6. Watanabe, T., Koga, M., and Morishima, S., "Plate Reformer for Molten Carbonate Fuel Cell," 1988 Fuel Cell Seminar Abstracts, pp.56-59 (1988).

7. Lemons, R. A., "Fuel Cells for Transportation," *Journal of Power Sources*, **29**, pp.251-264 (1990).
8. Gates, S. M. Russell Jr., J. N., and Yates Jr., J. T., "Bond Activation Sequence Observed in the Chemisorption and Surface Reaction of Ethanol on Ni(111)," *Surface Science* **171**, pp.111-134 (1986).

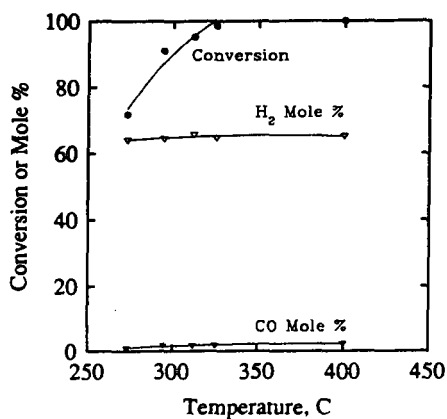


Fig. 1. Methanol conversion and mole percent of hydrogen and carbon monoxide obtained from partial oxidation of methanol over CuZnO.

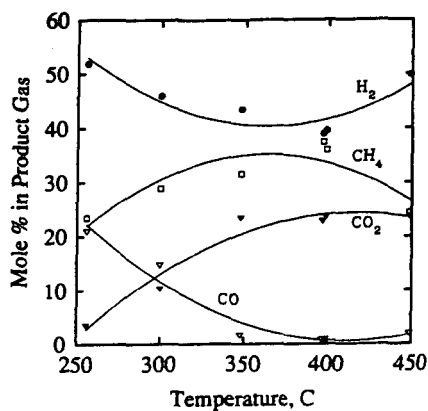


Fig. 2. Product gas distributions obtained with ethanol and over a nickel-based

THE EFFECT OF CARBON MONOXIDE CONTAMINATION ON ANODE EFFICIENCY IN PEM FUEL CELLS

J.C. Amphlett, R.M. Baumert, R.F. Mann, B.A. Peppley, P.R. Roberge, and A. Rodrigues
Royal Military College of Canada
Kingston, Ontario K7K 5L0 Canada

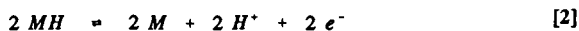
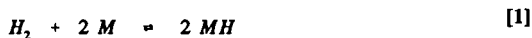
keywords: carbon monoxide poisoning fuel cell

ABSTRACT

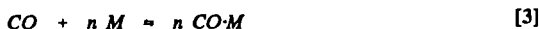
Carbon monoxide (CO) contamination in the anode feed acts as a poison to platinum electrodes in proton exchange membrane (PEM) fuel cells. The CO is preferentially adsorbed onto the platinum, blocking active catalyst sites which are required for hydrogen oxidation. An empirical model of the performance of a Ballard PEM fuel cell based on a mechanistic analysis of the gas-electrode-interface has been developed by our group. This model was modified with a CO surface coverage term to account for the effect of CO contamination on the fuel cell output voltage. The effect of CO enters the model as a reduction in the exchange current which results in an increase in activation voltage losses.

A proton exchange membrane (PEM) fuel cell system combines hydrogen and oxygen electrochemically via catalyzed reactions. The products of these reactions are electrochemical energy and water. Hydrogen can be obtained by steam reforming methanol or other light hydrocarbon fuels. The reformat feed gas may contain up to 5 % carbon monoxide (CO) by volume, which can be reduced to 100 ppm using a selective oxidizer^{1,2}. Even small traces of CO, however, can cause significant reductions in fuel cell performance. It has been shown³ that even 30 ppm of CO can cause a 48 % drop in the output cell voltage of a PEM fuel cell lowering it from 0.60 V to 0.31 V at 150 Amps. Other researchers² have reported output voltage drops up to 90 % for 100 ppm of CO at a current density of 650 ASF.

Adsorption of carbon monoxide greatly reduces the activity of the platinum electrocatalyst by blocking active catalyst sites¹. CO poisoning thus reduces the voltage output of a PEM fuel cell by limiting the number of catalyst sites available for the hydrogen oxidation reaction. The mechanism for the electrochemical oxidation of molecular hydrogen on platinum is believed to proceed according to the Tafel-Volmer Sequence^{4,5,6}:



The rate controlling reaction step is the dissociation of the adsorbed hydrogen molecule to two hydrogen atoms (shown in reaction [1]). CO impurities in the hydrogen feed, may result in another competitive adsorption process:



where n is the average number of platinum sites occupied by each carbon monoxide molecule. It has been reported⁷ that $1 \leq n \leq 2$. These inhibiting effects of CO can be explained through the kinetics of the anode reaction in the fuel cell.

The output voltage of a PEM fuel cell consists of three terms: the thermodynamic potential, the activation overvoltage, and the ohmic overvoltage, with mass transport losses incorporated into each of the terms⁸:

$$V = E + \eta_{act} + \eta_{ohmic} \quad [4]$$

where η_{act} and η_{ohmic} are both negative terms which decrease the total output voltage. The polarisation due to kinetic losses at the anode has been defined by Berger⁸:

$$\eta_{act} = \frac{RT}{2F} \ln \frac{I^0}{I} \quad [5]$$

where the exchange current density, I^0 , is always less than the actual current density, I . The exchange current density for a fuel cell is defined as the current density in either direction at reversible conditions⁸. This occurs at zero overvoltage when the anodic and cathodic currents are equal.

DERIVATION OF A PERFORMANCE MODEL INCORPORATING THE EFFECTS OF CO

The rate limiting process for the kinetics of the anode reaction is the chemisorption of hydrogen onto active catalyst sites⁵. The exchange current density is thus dependent upon the rate of chemisorption. As CO is preferentially adsorbed onto the platinum, the rate of hydrogen chemisorption will decrease, lowering values of current density and increasing the activation overvoltage. The fraction of the total platinum sites that are available, θ_M , will be reduced by the fractional CO surface coverage, θ_{CO} , so that the fraction of the catalyst that is available for hydrogen chemisorption becomes:

$$\theta_M = 1 - \theta_H - \theta_{CO} \quad [6]$$

A special case of this conservation equation applies at zero current when all values are at an steady-state, zero overvoltage condition:

$$\theta_{M,0} = 1 - \theta_{H,0} - \theta_{CO,0} \quad [7]$$

The electrode potential in the presence of CO can be expressed as^{5,6,9}

$$E = E^* + \frac{RT}{F} \ln \left(\frac{1 - \theta_{H,0} - \theta_{CO,0}}{\theta_{H,0}} \right) \quad [8]$$

Vogel and co-workers⁵ proposed that the exchange current density for pure hydrogen (no CO contamination) be defined as:

$$I^o = 2FkC_{H_2}(1-\theta_{H_2})^2 \quad [9]$$

and the exchange current density with CO contamination be defined as⁵

$$I_{CO}^o = 2FkC_{H_2}(1-\theta_{H_2})^2(1-\theta_{CO,\rho})^2 \quad [10]$$

Therefore, the effects of CO can be expressed by combining Equations [9] and [10]^{4,6,9}:

$$I_{CO}^o = I^o(1-\theta_{CO,\rho})^2 \quad [11]$$

where I_{CO}^o is the exchange current density for a CO site coverage of $\theta_{CO,\rho}$ and I^o is the exchange current density with no CO contamination. Combining Equations [5] and [11] yields the following expression for the activation overvoltage with CO effects:

$$\eta_{act,CO} = \frac{RT}{2F} \ln \frac{I^o(1-\theta_{CO,\rho})^2}{I} \quad [12]$$

Rearranging Equations [4] and [12] produces a relationship between the steady-state (ie. zero current) fractional surface coverage of CO and overvoltage:

$$\theta_{CO,\rho} = 1 - \exp \left[\frac{-F}{RT} (\eta_{act} - \eta_{act,CO}) \right] \quad [13]$$

Now that the CO concentration can be expressed as a surface coverage, the next step is to incorporate the CO surface coverage term into a fuel cell performance model. Combining Equations [4], [12], and [13] will yield the simple expression for the fuel cell output voltage:

$$V_{CO} = V + \frac{RT}{F} \ln(1-\theta_{CO,\rho}) \quad [14]$$

as the general case for any PEM fuel cell where V is the cell voltage for a zero CO content.

A model predicting the output voltage of a PEM fuel cell (a Ballard Power System Mark IV single cell with NafionTM membrane, Pt catalyst and an active surface area of 50.56 cm²) has been developed by our group^{10,11}. Mechanistic expressions were developed for each term in Equation [4], leading to an expression with seven unknown coefficients. These model parameters were determined by least squares linear regression using the experimental data based on the Ballard single cell. The following empirical expression was obtained:

$$\begin{aligned} V = & 1.23 - 0.85 \cdot 10^{-3} (T-298.15) + 4.31 \cdot 10^{-5} T [\ln(p_{H_2}) + \frac{1}{2} \ln(p_{O_2})] \\ & - 0.951 + 3.12 \cdot 10^{-3} T - 1.87 \cdot 10^{-4} T [\ln(i)] + 7.40 \cdot 10^{-3} T [\ln(c_{O_2})] \\ & + 0.016 - 3.5 \cdot 10^{-3} T + 8.0 \cdot 10^{-5} i \end{aligned} \quad [15]$$

The operating range for each experimental variable were as follows: 50 ASF $\leq I \leq$ 300 ASF, 328 K $\leq T \leq$ 300 K, 0.64 atm $\leq p_{O_2} \leq$ 3.06 atm, and 1.99 atm $\leq p_{H_2} \leq$ 3.06 atm. By combining Equations [14] and [15], the effect of CO contamination can be incorporated into the performance model of the PEM fuel cell.

APPLICATION OF THE MODIFIED PERFORMANCE MODEL TO PUBLISHED DATA

Figure 1 shows the experimentally measured effect of CO contamination on the output voltage of a PEM fuel cell as reported by Lemons². The derivation of Equation [13] implies that $\theta_{\text{CO},o}$ does not vary with current density (based on the definition of exchange current). Equation [13] therefore predicts that the decrease in the output cell voltage, $(V - V_{\text{CO}})$, should be uniform over the polarization curve as shown in Figure 2. The values of $\theta_{\text{CO},o}$ used to generate Figure 2 are based on the values of $(V - V_{\text{CO}})$ at 700 ASF for each level of CO contamination shown in Figure 1. These values of $\theta_{\text{CO},o}$ are given in Table 1. A current density of 700 ASF was chosen, since the high current density end of a polarization curve is more likely to be at steady-state during an experiment than the low current density end.

DISCUSSION

Comparing Figures 1 and 2, it is clear that the modified performance model, incorporating the effect of CO based on the analysis of Dhar and Vogel, does not predict the observed variation in fuel cell performance reported by Lemons. Assuming $\theta_{\text{CO},o}$ does not vary with current density, Equation [14] is not able to account for the points of inflexion seen in Figure 1. Several explanations for this disagreement are possible.

It is commonly known that the complex multi-phase system at the electrolyte-electrocatalyst-gas interface is very slow in reaching steady-state. The processes involved, such as membrane hydration, catalyst surface equilibration and water removal, can undergo very slow transients as operating conditions are changed. It is possible, therefore, that there is a systematic error in the measured output cell voltage which varies with current density in the data reported in Figure 1 because steady-state was not fully attained. If Figure 1 is compared with Figure 2, it is clear that the experimental values of $\theta_{\text{act,CO}}$ are lower than that of the predicted values. This could imply that the CO poisoning process is still underway, perhaps too slowly to be evident, and that the experimental values of $\theta_{\text{act,CO}}$ are still increasing.

A second possible explanation is that the assumption of θ_{CO} remaining constant at $\theta_{\text{CO},o}$ for a particular CO concentration (as concluded by Dhar³) is not valid. A conservation analysis of the concentration of chemisorbed H, θ_{H} , will indicate that the value of θ_{H} is determined by the relative rates of H atoms occupying vacant sites and vacating occupied sites. If the removal rate increases, θ_{H} decreases. When the basic two processes, adsorption and desorption, are joined by a third, the movement of protons from platinum sites into the membrane toward the cathode, θ_{H} should decrease. The greater the cell current density, such that the greater the required proton flux from the anode to the cathode, the lower θ_{H} should be. Since hydrogen and CO are involved in a competitive chemisorption process, a decrease in θ_{H} should permit a decrease in θ_{CO} . Thus higher currents should cause a higher fraction of the Pt sites to be poisoned by CO and the performance of the cell to degrade. This hypothesis can be indirectly tested as follows. As explained earlier, the 700 ASF data from Lemon's paper were used to estimate $\theta_{\text{CO},o}$ at each CO level via Equation [13]. If instead, overvoltages at other current densities are used to make the same estimation, the results in Figure 3 are obtained. Since the choice of 700 ASF data was somewhat arbitrary, it would be expected, for a particular ppm level of CO in the anode gas, that the same value of $\theta_{\text{CO},o}$ would be calculated from Equation [13] for all current densities. Figure 3 makes it clear that this is far from true.

CONCLUSIONS

The model previously proposed^{5,6,9} to account for the effect of CO contamination on the activation overvoltage in PEM fuel cells does not appear to explain the one available set of published data². It is possible that either the model or the data are at fault. More work, both theoretical and experimental, is required.

Table 1. The surface coverage of carbon monoxide as a function of CO concentration based on Lemons' data at 700 ASF.

CO concentration (ppm)	θ_{CO}
5	0.99988109
10	0.99998049
20	0.99999477
50	0.99999927
100	0.99999980

Figure 1. Experimental data on the effects of CO impurities on a PEM fuel cell (reconstructed from Lemons, R.A., *J of Power Sources* 29, 251 (1990))²

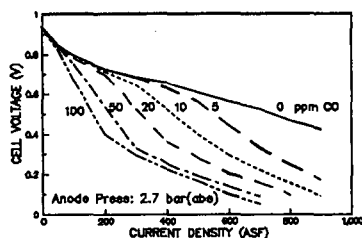


Figure 2. The predicted effects of CO on the Ballard Mark IV fuel cell performance using θ_{CO} data from Table 1.

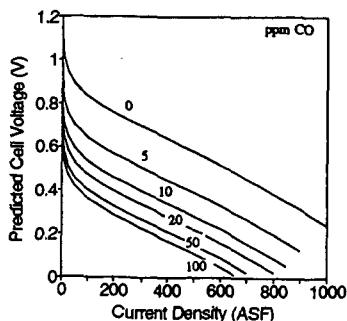
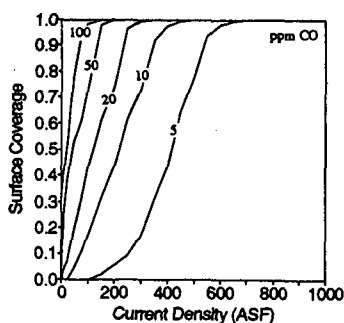


Figure 3. CO surface coverage on a platinum catalyst as a function of current density based on Lemons' data.



NOTATION

A	active surface area, cm ²		
c _i	concentration of species i at the interface, mol·cm ⁻³		
CO	carbon monoxide		
E	thermodynamic potential, V		
F	Faraday's Constant		
I	current density, ASF		
i°	exchange current density, ASF		
i	current, A		
K	adsorption equilibrium constant, bar ⁻¹		
k	reaction rate constant, mol·s ⁻¹ ·bar ⁻¹		
M	available catalyst site		
MCO	catalyst site with CO adsorbed		
MH	catalyst site with H adsorbed		
N	net number of electrons transferred in a reaction		
n	average number of platinum sites occupied by the CO molecule		
p _i	partial pressure of species i in the fuel cell, bar		
R	ideal gas constant, 8.314 J/mol·K		
r	reaction rate, mol·s ⁻¹	Subscripts	
T	temperature of the fuel cell stack, K	CO	occupied by a CO molecule
V	total cell output voltage, V	H	occupied by a hydrogen atom
^{act}	activation overvoltage, V	M	unoccupied platinum "metal" site
^{ohmic}	ohmic overvoltage, V	o	steady-state condition
θ	fraction of platinum surface sites	T	total number of platinum "metal" sites

REFERENCES

1. S. Gottesfeld, S. Pafford. *J. Electrochem. Soc.* **135**, 2651 (1988).
2. R.A. Lemons. *J. Power Sources* **29**, 251 (1990).
3. C.M. Seymour. *J. Power Sources* **37**, 155 (1992).
4. K.J. Vetter. *Electrochemical Kinetics*, p.522. Academic Press, New York (1967).
5. W. Vogel, J. Lundquist, P. Ross, and P. Stonehart. *Electrochim. Acta* **20**, 79 (1975).
6. J. Wang and R.F. Savinell. *Electrochim. Acta* **37**, 2737 (1992).
7. R.P. Eischens and W.A. Pliskin. *Z. Phys. Chem.* **24**, 11 (1960).
8. C. Berger. *Handbook of Fuel Cell Technology*, Prentice-Hall, Englewood Cliffs, NJ (1968).
9. H.P. Dhar, L.G. Christner, A.K. Kush, and H.C. Maru. *J. Electrochem. Soc.* **133**, 1574 (1986).
10. R.M. Baumert. *Performance Modelling of the Ballard Mark IV Solid Polymer Electrolyte Fuel Cell*, Masters Thesis, Queen's University, Kingston, Ont. (1993).
11. J.C. Amphlett, R.M. Baumert, R.F. Mann, B.A. Peppley, P.R. Roberge. "Performance Modelling of the Ballard Mark IV Solid Polymer Electrolyte Fuel Cell", submitted to *J. Electrochem. Soc.* June 1993.
12. T.E. Springer, T.A. Zawodzinski, and S. Gottesfeld. *J. Electrochem. Soc.* **138**, 2334 (1991).

Proton Exchange Membrane Fuel Cell R&D at Texas A&M University

Supramaniam Srinivasan, Arvind Parthasarathy, Sanjeev Mukerjee, A. Cesar Ferreira,
Masanobu Wakizoe, Yong Woo Rho, Junbom Kim and A. John Appleby,
Center for Electrochemical Systems and Hydrogen Research,
Texas Engineering Experiment Station, Texas A&M University System,
College Station, Texas 77843-3402

SPECTRUM OF R&D ACTIVITIES

Research efforts in the area of proton exchange membrane fuel cells (PEMFC) at the Center for Electrochemical Systems and Hydrogen Research (CESHR), Texas Engineering Experiment Station (TEES), Texas A&M University System (TAMUS) involves multifaceted fundamental and applied approaches. Among the main goals in this effort are the attainments of high power densities and energy efficiencies and long lifetimes in PEMFCs with low Pt loading electrodes. Our efforts comprise of (1) microelectrode and single cell investigations for the determination of the electrode kinetic, mass transport and ohmic parameters as well as membrane characteristics such as ionic conductivity and oxygen solubility and diffusion coefficient and (2) the use of x-ray techniques such as XANES and EXAFS to understand the role of geometric and electronic factors in the electrocatalysis of oxygen reduction by the Pt-C and by binary alloys of Pt with base transition elements. In addition, are the efforts to optimize the membrane electrode assemblies to attain high catalyst utilization and lower mass transport losses. Besides these, are the engineering-related efforts towards improved water and thermal management in 50 cm² cells and the modeling studies of the membrane electrode assemblies and of multicell stacks. The knowledge gained from these investigations are being incorporated in the current projects for the development of multicell stacks, with performance capabilities acceptable for space and terrestrial (electric vehicles) applications. The progress made in the above-mentioned areas of research and development are briefly summarized in the following sections.

MICROELECTRODE TECHNIQUE TO DETERMINE ELECTRODE KINETIC, MASS TRANSPORT AND OHMIC PARAMETERS

A novel microelectrode technique was developed to carry out these determinations at the platinum microelectrode/proton exchange membrane interface. An illustration of the experimental set-up for these measurements, as a function of temperature and pressure, is represented in Fig. 1. Cyclic voltammetric, chronoamperometric and AC impedance spectroscopic techniques were used. The purity of the system was assessed from the cyclic voltammograms at a sweep rate of 100 mV/s. The electrode kinetic parameters for oxygen reduction were obtained from the mass transfer corrected Tafel plots, as obtained from the current versus potential plots recorded on the microelectrode at low sweep rates (< 10 mV/s). The analysis of chronoamperometric plots yielded the diffusion coefficients and solubilities of oxygen in the membrane. The results of the AC impedance studies lent insight on (i) specific resistance of the membrane; (ii) the grain boundary resistance and capacitance of the membrane; and (iii) the charge transfer resistance of the oxygen reduction reaction and the double layer capacitance as a function of potential. These parameters were determined as a function of operating temperature and pressure. A detailed study was carried out using DuPont's Nafion® membranes. Studies are in progress with the Asahi Chemicals Aciplex®-S membranes. The results to date provide clear evidence for the better electrode kinetic and mass transport rates for oxygen reduction at the interfaces of platinum with proton exchange membrane rather than with aqueous acid electrolytes, such as sulfuric or perchloric acid.

OPTIMIZATIONS OF STRUCTURES AND COMPOSITIONS OF ELECTRODES AND OF MEMBRANE AND ELECTRODE ASSEMBLIES TO ATTAIN HIGH ENERGY EFFICIENCIES, HIGH POWER DENSITIES AND TO ENHANCE PLATINUM UTILIZATION

Considerable progress was made in these areas during the last five years at TAMU. Firstly, high energy efficiencies and high power densities were achieved with low platinum loading or (about 0.4 mg/cm²) electrodes using H₂/O₂ or H₂/Air as reactants. Secondly, the platinum utilization was significantly enhanced in PEMFCs (Fig. 2) with electrodes containing only about 0.1 mg/cm² prepared in-house by the rolling method. It was also demonstrated that the platinum

utilization can be increased by using alloy electrocatalysts (Pt-Cr, Pt-Co, Pt-Ni). Thirdly, performance improvements were made possible by optimization of the Teflon contents in the active and diffusion layers.

The alternate approach to attain high energy efficiencies and power densities is to use perfluorinated sulfonic acid membranes with higher water contents and specific conductivities. Previous studies by Srinivasan and his co-workers at Los Alamos National Laboratory and at Texas A&M University have demonstrated the considerably better performances with the Dow membranes than with Nafion®. Our studies, since 1992, have revealed high levels of performances with Asahi Chemicals Aciplex®-S membranes. These studies also demonstrated the advantages of increased temperature for hot-pressing of the membrane and electrode assemblies to considerably higher values (say by about 20°C) than the glass-transition temperature.

X-RAY ABSORPTION TECHNIQUES TO ELUCIDATE ROLE OF ELECTRONIC AND GEOMETRIC FACTORS ON THE ELECTROCATALYSIS OF OXYGEN REDUCTION BY BINARY PLATINUM ELECTROCATALYSTS

The x-ray absorption studies (XAS) were conducted at Brookhaven National Laboratory (BNL) by McBreen and Mukerjee. The combination of both XANES (x-ray absorption near edge structure) and EXAFS (extended x-ray absorption fine structure) provide a powerful tool, especially because of the *in situ* capabilities, to elucidate the mechanism of electrocatalysis of oxygen reduction on the alloy electrocatalysts (Pt-Cr, Pt-Co, Pt-Ni, Pt-Fe and Pt-Mn). The XAS studies were made both in the transmission and fluorescent modes using the National Synchrotron Light Source at BNL. XAS measurements were made at the Pt L₂ and L₃ edges as well as the K edge of the respective alloying component. The *in situ* measurements were made at various potentials in the range from 0 to 1.0 V/RHE. The EXAFS investigation on the Pt-Ni alloy rules out any evidence for a redox mechanism and was confirmed by the lack of potential dependence in the XANES studies. However, an increase of the Pt L₃ XANES reveals an emptying of the d states. The results on Pt-Co indicate a similar behavior. The XANES for Pt-Cr does not show any effect on the Pt-d states indicating a different electrocatalytic pathway from that of Pt-Ni. The lack of dependence of the Ni XANES and EXAFS with respect to potential suggest the possibility of the outer alloy surface being Pt. A correlation of the electronic and geometric factors for Pt and the alloys, as ascertained from the XANES and EXAFS studies, during oxygen reduction at two potentials is presented in Table 1. Optimum values for the d-orbital vacancy and bond distance are necessary to obtain the highest electrochemical performance. The best values correspond to those for Pt-Cr.

NOVEL METHOD FOR DETERMINATION OF TRANSPORT PARAMETERS OF H₂ AND O₂ IN PEMFCs

The permeation method used for the determinations of diffusion coefficients and solubilities of hydrogen in thin metallic membranes was extended for the determinations of these mass transport parameters for the fuel cell reactants in Nafion® and in Aciplex®-S membranes. In these experiments the transient and steady state currents were recorded as functions of the time for the oxidation of hydrogen or reduction of oxygen transported through the membranes, when the pressures of these gases were either increased or decreased instantaneously. An analysis of these measurements yields the diffusion coefficients and solubilities (Table 2). The values of the D are higher for the Nafion® than for the Aciplex®-S membranes. The reverse is the case for the C. However, the value of the product DC, the essential parameter governing mass transport rate, is higher for the Aciplex®-S than for Nafion®.

EXPERIMENTAL AND MODELING ANALYSIS OF MASS TRANSPORT PHENOMENA IN PEMFCs

One of the major challenging problems in PEMFCs is to minimize overpotential losses due to mass transport phenomena at the oxygen electrode when using air as the cathodic reactant. Experimental studies were conducted in PEMFCs to determine the effect of the type of inert gas (He, Ar, N₂) and the oxygen content in the gas mixture on the PEMFC performance. A theoretical analysis led to the following conclusions: (i) mass transport overpotentials are less when using O₂/He rather than O₂/N₂ or O₂/Ar gas mixtures; (ii) above 40% O₂ in the gas mixtures, departure from linearity of the cell potential (E) vs current density (i) plot occurs at higher current densities; (iii) the higher slope of the linear region in the E-i plot is due to mass transport in the

electrocatalytic layer; and (iv) the departure from linearity of the E-i plot is due to mass transport in the substrate-diffusion layer.

A second type of mass transport analysis is underway in our laboratories from experimental measurements of performance of PEMFCs at different flow rates of the cathodic reactant (O_2 or air). The preliminary results show that (i) even at high current densities, there is hardly any dependence of performance on flow rate; and (ii) with air, there is a significant flow rate dependence at current densities of 300 m A/cm^2 and higher. The problem with air at 1 atm is that when one takes into consideration the vapor pressure of water at about 70°C , the partial pressure of oxygen at 1 atm total pressure is only about 0.12 atm. Thus in order to satisfy the oxygen requirement at the higher current densities, extremely high flow rates of air are necessary.

ACKNOWLEDGEMENTS

The areas of work, reviewed in this paper, were carried out under the auspices of the NASA Johnson Space Center, NASA Lewis Research Center, Texas Higher Education Coordinating Board, Asahi Chemical Industry Co. Ltd. and Mazda R&D of North America.

Table 1. Comparison of Electronic and Geometric Parameters in the Electrocatalysis on some Binary Alloys of Pt: In-situ XANES and EXAFS results at 0.3 V and 0.6 V vs SCE

Electrocatalyst	Double Layer Region (0.3 V vs SCE)			Oxygen Reduction Region (0.6 V vs SCE)		
	(Du)s	Pt-Pt (R) (Å°)	Pt-Pt (N)	(Du)s	Pt-Pt (R) (Å°)	Pt-Pt (N)
Pt/C	0.329	2.77	8.7	0.370	2.77	6.8
Pt/Mn	0.331	2.76	7.5	0.344	2.76	8.3
Pt/Cr	0.360	2.71	6.1	0.358	2.71	6.1
Pt/Fe	0.368	2.70	5.7	0.370	2.71	5.5
Pt/Co	0.401	2.68	6.9	0.390	2.68	7.6
Pt/Ni	0.409	2.68	9.1	0.404	2.68	9.5

(Du)s : Pt *d* orbital vacancy per atom

R : Interatomic distance

N : Co-ordination number around the first co-ordination shell

Table2. Dependence of Temperature on Transport Parameters in PEMFCs with Aciplex®-S and Nafion®-117 Membranes. Values of Activation Energy for the Diffusion Coefficient are also presented.

(1) H₂

Parameter T or ΔE*	Aciplex-S			Nafion-117		
	D×10 ⁶ cm ² /s	C _o mM	DC _o ×10 ⁶ mM·cm ² /s	D×10 ⁶ cm ² /s	C _o mM	DC _o ×10 ⁶ mM·cm ² /s
50°C	0.78	89.4	69.73	2.44	10.86	26.50
70°C	1.33	78.3	104.14	3.91	12.13	47.43
95°C	1.87	100.4	187.75	5.88	12.28	72.21
85°C*						
ΔE*						
kcal/mol	4.68			5.75		

* Nafion-117

(2) O₂

Parameter T or ΔE†	Aciplex-S			Nafion-117		
	D×10 ⁶ cm ² /s	C _o mM	DC _o ×10 ⁶ mM·cm ² /s	D×10 ⁶ cm ² /s	C _o mM	DC _o ×10 ⁶ mM·cm ² /s
50°C	2.88	4.13	11.89	6.94	1.19	8.26
70°C	3.11	6.68	20.77	8.54	1.81	15.46
95°C	5.04	8.61	43.39	11.50	1.99	22.89
85°C*						
ΔE*						
kcal/mol	3.41			3.39		

* Nafion-117

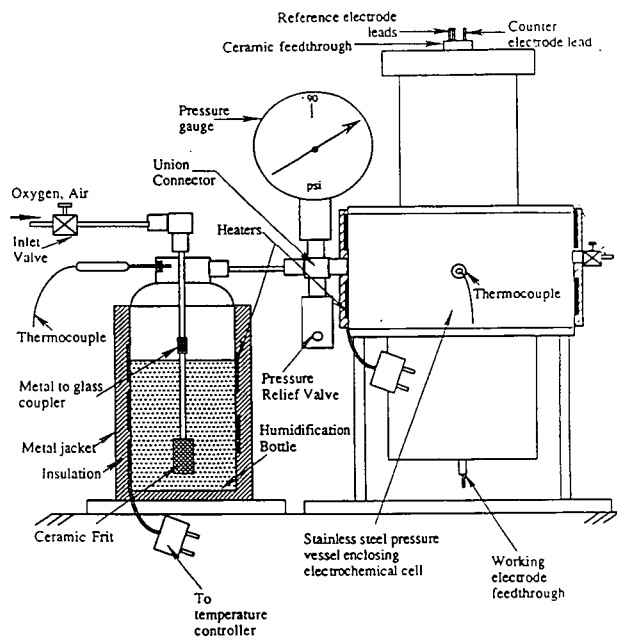


Fig 1 Schematic of the pressure vessel housing the electrochemical cell and the humidification set-up.

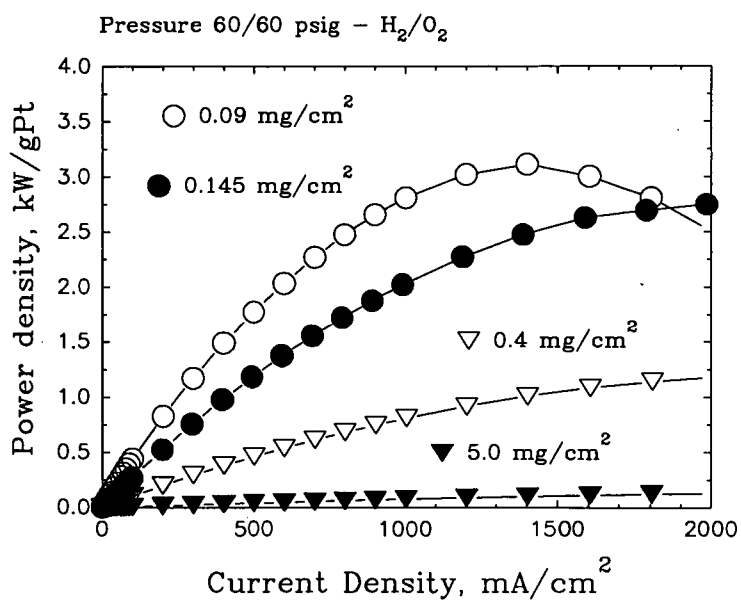


Fig 2. Effect of Pt loading in the electrode on power vs current density in PEMFC (●) 0.090 and (○) 0.145 $mg Pt/cm^2$ -CESHR; (▽) 0.4 $mg Pt/cm^2$ ETEK, Inc.; 5 $mg Pt/cm^2$ -Johnson & Matthey at 95°C and 5 atm.